Recovery of the full *in vivo* firing range in post-lesion surviving DA SN neurons associated with Kv4.3-mediated pacemaker plasticity

Lora Kovacheva[1*], Josef Shin[1,2], Josefa Zaldivar-Diez[1,3], Johanna Mankel[1], Navid Farassat[1,4], Kauê Machado Costa[1,5], Poonam Thakur[1,6], José Obeso[3] & Jochen Roeper[1*]

1 Institute of Neurophysiology, Neuroscience Center, Goethe University, Frankfurt, Germany

2 Department of Neurology, University Medical Centre of the Johannes Gutenberg University Mainz, Mainz, Germany

3 HM CINAC (Centro Integral de Neurociencias Abarca Campal), Hospital Universitario HM Puerta del Sur, HM Hospitales. Madrid, Spain.
CIBERNED, Instituto de Salud Carlos III, Madrid, Spain.
Medical School, CEU-San Pablo University, Madrid, Spain

4 Eye Center, Medical Center-University of Freiburg, Freiburg im Breisgau, Germany

5 Department of Psychology, University of Alabama at Birmingham, AL, USA

6 School of Biology, Indian Institute of Science Education and Research (IISER)-Thiruvananthapuram, Kerala, India

[*]Corresponding authors:
Dr. Lora Kovacheva & Prof. Dr. Jochen Roeper
Institute for Neurophysiology
Neuroscience Center, Goethe University
Theodor-Stern-Kai 7, 60590 Frankfurt, Germany
e-mail: roeper@em.uni-frankfurt.de & lorask@gmail.com
webpage: https://www.neurophys-frankfurt.de
Tel: +49-69-6301-84091/92

Abstract

Dopamine (DA) neurons in the substantia nigra (SN) control several essential functions, including the voluntary movement, learning and motivated behavior. Healthy DA SN neurons show diverse firing patterns *in vivo*, ranging from slow pacemaker-like activity (1-10 Hz) to transient high frequency bursts (<100 Hz), interspersed with pauses that can last hundreds of milliseconds. Recent *in vivo* patch experiments have started to reveal the subthreshold mechanisms underlying this physiological diversity, but the impact of challenges like cell loss on the *in vivo* activity of adult DA SN neurons, and how these may relate to behavioral disturbances, are still largely unknown. We investigated the *in vivo* electrophysiological properties of surviving SN DA neurons after partial unilateral 6-OHDA lesions, a single-hit, non-progressive model of neuronal cell loss. We show that mice subjected to this model have an initial motor impairment, measured by asymmetrical rotations in the open field test, which recovered over time. At 3 weeks post-lesion, when open field locomotion was strongly impaired, surviving DA SN neurons showed a compressed *in vivo* dynamic firing range, characterized by a 10-fold reduction of *in vivo* burst firing compared to controls. This *in vivo* phenotype was accompanied by pronounced *in vitro* pacemaker instability. In contrast, in the chronic post-lesion phase (>2 months), where turning symmetry in open field locomotion had recovered, surviving SN DA neurons displayed the full dynamic range of *in vivo* firing, including *in vivo* bursting, similar to controls. The normalized *in vivo* firing pattern was associated with a 2-fold acceleration of stable *in vitro* pacemaking, mediated by Kv4.3 potassium channel downregulation. Our findings demonstrate the existence of a homeostatic pacemaker plasticity mechanism in surviving DA SN neurons after pronounced cell loss.

Keywords

dopamine, 6-OHDA, Kv4.3 potassium channel, substantia nigra, pacemaker, homeostasis, intrinsic plasticity

Introduction

Midbrain dopamine (DA) neurons in the substantia nigra (SN) project mainly to the dorsal striatum (DS), where they release dopamine in an activity-dependent manner, further shaped by additional mechanisms at the distal axon (Liu et al., 2022, Kramer et al., 2023). The resulting temporal and spatial dynamics of DA release in DS are relevant for multiple functions, including the control of voluntary movements, as evidenced by the cardinal features of Parkinson disease (PD), which is characterized by the death of SN DA neurons. The *in vivo* activity pattern of healthy SN DA neurons is complex, ranging from slow pacemaker-like activity (1-10 Hz) to transient high frequency bursts (<100 Hz), and interspersed with pauses that can last hundreds of milliseconds. However, our understanding if and how SN DA neuron electrical activity adapts to cell loss, relevant during aging or PD, is limited.

We have previously shown that overexpression of mutant A53T-α-synuclein induced an age-dependent acceleration of *in vivo* and *in vitro* firing frequencies. This was associated with redox-mediated dysfunction of Kv4.3 channels and an upregulation of Kv4.3 expression, potentially representing a homeostatic attempt to regulate pacemaker frequency (Subramaniam, Althof, et al. 2014). This study, however, left a more fundamental question unanswered: do adult DA SN neurons have the ability for homeostatic regulation of firing pattern in response to challenge? For this purpose, we employed the well-established 6-Hydroxy-Dopamine (6-OHDA) chemical lesion model in order to induce an unilateral loss of about half of the DA SN neurons. 6-OHDA has been widely used for generating non-progressive loss of DA SN neurons (Rubi and Fritschy 2020; P. R. L. Parker, Lalive, and Kreitzer 2016; Ungerstedt 1968). We opted for an unilateral, partial, intrastriatal 6-OHDA model, previously well characterized by Bez et al. (Bez, Francardo, and Cenci 2016). Bez and colleagues, as well as others, demonstrated that these partial 6-OHDA DA lesions are non-progressive and follow a stereotypical time course: an initial damage phase dominated by cell loss, inflammation and behavioral impairment for about 3 weeks, which is followed by a chronic phase (studied for up to 20 month in mice), characterized by partial behavioral recovery, neurochemical and molecular adaptations, and – to a certain degree – axonal sprouting of remaining DA neurons (Bez, Francardo,

83 and Cenci 2016; Cenci and Björklund 2020; Kirik, Rosenblad, and Björklund 1998; Schwarting and
84 Huston 1996; Winkler et al. 2002). This framework, with its distinct phases of impairment and
85 subsequent partial functional recovery, provides a well-suited platform to investigate if and how the
86 *in vivo* firing properties of surviving DA SN neurons change over time. Previous electrophysiological
87 investigations of viable post-6-OHDA DA neurons have been limited, with only Hollerman & Grace
88 providing a pioneering dataset (Hollerman and Grace 1990). They found lesion-size-dependent
89 changes in *in vivo* firing properties of putative DA neurons in rats, including a decrease of *in vivo* burst
90 firing occurring with larger lesions (Hollerman and Grace 1990). Therefore, conducting
91 electrophysiological investigations at two distinct time-points within the context of a non-progressive
92 partial 6-OHDA lesion is expected to provide novel insights into the homeostatic properties of
93 identified DA SN neurons.

94 Here, we explore the electrophysiological properties, both *in vivo* and *in vitro,* of surviving SN DA
95 neurons in an intra-striatal unilateral 6-OHDA lesion mouse model, titrated to about 40% surviving SN
96 DA neurons. We selected two time points for recordings based on the continuous behavioral
97 characterization of the motor phenotypes.

98

99 # Results
100

101 ## Early behavioral impairments and long-term adaptations after partial lesion of substantia
102 nigra dopamine neurons
103

104 To characterize electrophysiological properties in surviving and identified SN DA neurons, we
105 employed a C57Bl6N mouse model with a partial 6-OHDA lesion of the nigrostriatal pathway. We
106 explored different 6-OHDA concentrations (0.2µg/µl - 2µg/µl) and volumes (2µL and 6µL) resulting in
107 a range of 0.4µg to 12µg 6-OHDA) to titrate the ipsilateral loss of DA SN neurons (Suppl. Fig. 1E for
108 details). To target 40-50% cell loss, we slowly (250 nl/min) infused 6 µl of 2µg/µl 6-OHDA (i.e. 24 min
109 total infusion time, total of 12 µg 6-OHDA) into the right DS. For controls, we infused vehicle (ACSF)
110 with the same rate and same volume into the right DS without observing any damage (Fig. 1B; Suppl.
111 Fig. 1-C). The loss of TH-positive SN neurons was quantified by unbiased stereology at 21 days and 3
112 months post-lesion (Fig. 1A).

113 We continuously characterized the motor phenotype of the model (i.e. open field locomotion, cylinder
114 test) until the two different end points, either 21-days post-lesion (early phase) or more than 60 days
115 post-lesion (late phase). In the first cohorts, the mice were sacrificed for TH immunohistochemistry in
116 midbrain and striatum. As shown in Fig. 1B, at the early phase, the number of TH-positive (i.e.
117 dopaminergic) SN neurons was reduced post-6-OHDA (lower left panels) compared to vehicle-control
118 mice (upper left panels). The right panel in Fig. 1B displays the stereological results of TH-positive SN
119 neurons for N=9 vehicle-treated and N=9 6-OHDA-infused male mice 21 days after their respective
120 infusions. The data were normalized to the stereological results of respective contralateral SN DA
121 neurons. In contrast to vehicle-infusions, where no ipsilateral loss of SN DA neurons was detected, the
122 number of ipsilateral surviving SN DA neurons in the early post-6-OHDA phase was on average reduced
123 to about 40% (Fig. 1B; vehicle: 100 ± 2.64 %; 6-OHDA: 36.85 ± 3.46%; $p < 0.0001$, Mann-Whitney test).
124 We also carried out the unbiased stereology for TH-positive SN neurons in the late phase and detected

125 a very similar degree of loss (Suppl. Fig. 1C, vehicle: 102.6 ± 7.9 %; 6-OHDA: 39.96 ± 3.7 %; p = 0.0262,
126 Mann-Whitney test; please add N numbers). Importantly, these results indicated that SN DA cell loss
127 was non-progressive throughout our observation period of more than 2 months. In addition, we
128 analyzed the axonal compartment of DA midbrain neurons by determining striatal TH-optical
129 densities, both for early and late phase (Suppl. Fig. 1). Similar to the midbrain DA cell body counts, we
130 found a stable reduction of about 50% of TH-immunosignal in the ipsilateral DS, again normalized to
131 the contralateral side (Suppl. Fig. 1A 21st day - vehicle: 98.4 ± 2.2 %; 6-OHDA: 42.5 ± 3.0 %; Suppl. Fig.
132 1B > 64 days - vehicle: 94.4 ± 2.7 %; 6-OHDA: 48.3 ± 3 %), both in early and late phase. By comparison,
133 the ventral striatum was only mildly affected (ca. 20 % reduction, Suppl. Fig. 1A 21st day - vehicle: 94.6
134 ± 2.0 %; 6-OHDA: 81.4 ± 3.0 %; Suppl. Fig. 1B > 64 days - vehicle: 97.8 ± 2.0 %; 6-OHDA: 75.2 ± 5.0 %).
135 In summary and in accordance with previous studies, our model induced stable 60% loss of SN DA
136 neurons, associated with a stable 50% reduction of DS TH-immunoreactivity throughout the entire
137 observation period (Bez, Francardo, and Cenci 2016; Cenci and Björklund 2020; Schwarting and Huston
138 1996). This stability provided a suitable framework to identify time-dependent homeostatic changes
139 in surviving SN DA neurons.

140 Fig 1 C shows the data from continuous behavioral monitoring of unilateral 6-OHDA and vehicle-
141 treated mice before and up to 68 days post-infusion. Based on previous studies (Cenci and Björklund
142 2020; Schwarting and Huston 1996), we focused on the dynamics of drug-free spontaneous turning
143 behavior during open field locomotion (Fig. 1C, lefts panels). In contrast to vehicle-infused mice, which
144 displayed a stable symmetric ratio (ca. 50%) of ipsi- to contral-lateral turning throughout the entire
145 experiment, 6-OHDA-infused mice showed a dramatic shift to ipsilateral turning immediately after
146 treatment (Figure 1C, right panel). Interestingly, ipsilateral turns occurred in long sequences of up to
147 40 individual turns, a pattern not observed in controls (Suppl. Fig. 3). Importantly, these turning
148 sequences as well as the overall ipsilateral bias gradually recovered completely over a 2-months post-
149 lesion period (two-way-ANOVA, p-value across time p<0.0001, p-value across groups p<0.0001,
150 significant difference between vehicle and 6-OHDA group till day 40, Šídák's multiple comparisons
151 test). Analysis of turning features, such as diameter or velocity, revealed that the recovered

152 contralateral turns were similar to turns performed by vehicle-treated mice (Suppl. Fig. 4). Also, open
153 field locomotion, quantified as total track length per session, recovered almost completely (Suppl. Fig.
154 1D). However, other motor behavior, the contralateral paw use during spontaneous rearing in the
155 cylinder test, did not show significant recovery throughout the experimental period (Fig. 1D) (21st
156 post-infusion day: vehicle 38.5 ± 5.2%, 6-OHDA 5.7 ± 1.4%, $p < 0.0001$, Mann-Whitney test; 68th post-
157 infusion day: vehicle 63.7± 6.6%, 6-OHDA 3.2 ± 1.8%, $p < 0.0001$, Mann-Whitney test). Finally,
158 repeating the continuous behavioral monitoring and the quantification of TH immunohistochemistry
159 in midbrain and striatum with female C57Bl6N mice, infused with either 6-OHDA or vehicle, showed
160 very similar results and gave no indications for sex differences (Suppl. Fig. 2).

161 To investigate the functional properties in immunohistochemically-identified surviving SN DA neurons,
162 we performed *in vivo* extracellular recordings combined with juxtacellular neurobiotin (NB) labeling
163 and *in vitro* whole-cell patch-clamp recordings combined with neurobiotin filling for two timepoints:
164 at an early timepoint (21st day after lesion, early phase), where a strong turning asymmetry was
165 present, and at a later time period (> 64 days post-lesion, late phase) when turning symmetry had
166 recovered.

167

168

169 Surviving SN DA neurons in the early post-6-OHDA phase exhibit impaired firing properties
170 both *in vivo* and *in vitro*

171

172 At the early post-6-OHDA phase, we explored the *in vivo* spontaneous activity of surviving identified
173 SN DA neurons in isoflurane-anesthetized mice, using single-unit extracellular recordings combined
174 with juxtacellular neurobiotin labelling and post-hoc TH immunohistochemistry (see schema Fig. 2A).
175 Figure 2B shows the *in vivo* extracellular electrical activity (top panel) and identification of a

representative SN DA neuron (lower right panel) from a control mouse, 3 weeks after vehicle infusion. Note the typical combination of irregular single spike firing with the occurrence of transient fast burst discharges (bursts were defined by the 80/160ms Grace criteria; see methods for details) and longer pauses. The interspike interval (ISI) histogram, which captures ISIs from the entire recording time of 10 min for this cell, displays the typical features of an *in vivo* bursty DA neuron, i.e. a bimodal ISI distribution representing intra- and interburst intervals over a broad dynamic range between ~30-1000 ms (lower left panel). This recorded and labelled cell was localized in the medial SN and characterized as TH-immunopositive. In comparison, Fig. 2C displays the representative *in vivo* activity of a surviving and identified SN DA neuron 3 weeks after 6-OHDA-infusion. Here, while irregular single-spike pacemaking was present similar to controls, fast burst events and slow pauses were almost completely absent (top panel). Indeed, the ISI histogram of this neuron, for the entire 10 min of recording, showed a compressed dynamic firing range and was well-described by a unimodal, Gaussian-like distribution without fast intraburst and slow interburst intervals (Fig. 2C, lower left panel). This recorded and labelled cell was also localized in the medial SN and identified as TH-immunopositive.

All *in vivo* recorded DA neurons, like the two representative cells shown above, from the early phase were successfully juxtacellularly labeled with NB, post-hoc immunohistochemically identified and localized within the ventral midbrain (Fig 2D, vehicle: n =28, N =15; 6-OHDA: n =18, N =16). For best comparison, we restricted our analysis to those DA midbrain neurons localized in the medial half of the SN (mSN), where it was possible to sample a sufficient number of surviving and spontaneously active DA neurons after 6-OHDA lesion. In contrast, we only managed to detect a small number of active DA neurons in the lateral SN (lSN), the most vulnerable part of the DA midbrain (Figure 2D). Consequently, Figure 2 E-H compares the group data of surviving mSN DA neurons at early phase between vehicle and 6-OHDA treatment. We detected an about 60% reduction of the mean firing rates for post-6-OHDA mSN DA neurons compared to vehicle-treated controls (Fig.2E; vehicle: mean frequency = 7.5 ± 0.9 Hz, 6-OHDA: mean frequency = 4.7 ± 0.6 Hz, p = 0.0184, Mann-Whitney test) and no significant differences in overall firing regularity (Fig. 2F; vehicle: CV = 53.9 ± 7.8 %, 6-OHDA: CV =

203 36.1 ± 3.7 %, p = 0.1694, Mann-Whitney test). Moreover, we observed a significant 10-fold reduction
204 of bursting - expressed as the percentage of spikes fired in bursts (SFB) and burst rate - in mSN DA
205 neurons in the 6-OHDA group compared to vehicle controls (Fig. 2G, vehicle: SFB = 31.2 ± 7.7; 6-OHDA:
206 SFB = 2.2 ± 1.1 %; p = 0.0032, Welch's t test; Fig. 2H, vehicle: burst rate = 0.34 ± 0.09 Hz, 6-OHDA: burst
207 rate = 0.04 ± 0.02 Hz; p = 0.0066, Welch's t test).

208 All other analyzed firing parameters, such as intra-burst firing frequencies, identified no additional
209 differences between the two groups (Suppl. Fig. 5A-G). In summary, we detected a rightward shift to
210 lower firing frequencies with a corresponding compression of the dynamic *in vivo* firing range in mSN
211 DA neurons surviving the 6-OHDA lesion (Suppl. Fig. 5I). Thus, in addition to DA cell loss, the
212 dysfunction of surviving DA neurons might be a novel contributing factor to the extensive motor
213 impairment , observed during the early post-6-OHDA phase. In particular, transient bursts of DA SN
214 neurons have been shown to provide start and stop signals for motor control (see discussion for
215 details).

216 Burst discharges in DA neurons are orchestrated by the interplay of patterned synaptic inputs with
217 their intrinsic excitability, giving rise to different types of *in vivo* bursting (Otomo et al. 2020). To
218 identify a potential contribution of cell-autonomous changes in intrinsic excitability of surviving mSN
219 DA neurons to their impaired *in vivo* dynamics, we also studied these cells *in vitro* in synaptic isolation
220 (see Schema 2I). Figure 2J shows a representative, stable and regular pacemaker activity of an
221 identified mSN DA neuron from a vehicle-infused control (lower right panel), as well as a subthreshold
222 response to hyperpolarizing current injection (lower left panel). In contrast, pacemaker activity of mSN
223 DA neurons post-6-OHDA infusion was unstable and characterized by intermittent periods of action
224 potential failure (see Fig. 2K, upper panel). However, subthreshold responses were similar to controls
225 (lower right panel). Analogous to the *in vivo* experiments, all *in vitro* recorded DA neurons were NB
226 filled, identified, and mapped, resulting in a similar medial localization of surviving SN DA neurons (Fig.
227 2L). When *in vitro* pacemaker properties were compared between identified mSN DA neurons from
228 the vehicle and the 6-OHDA groups (Fig. 2L), we detected no differences in mean firing rates (Fig. 2M,

229 vehicle: firing rate = 1.7 ± 0.2 Hz, 6-OHDA: firing rate = 2.4 ± 0.3 Hz, p = 0.1448, Mann-Whitney test),
230 rebound delays or sag-amplitudes (Fig. 2O, vehicle: rebound delay = 584.9 ± 95.8 ms, 6-OHDA:
231 rebound delay = 429.6 ± 56.1 ms, p = 0.1738, Mann-Whitney test; Fig. 2P, vehicle: sag-amplitude =
232 15.3 ± 1.1 mV, 6-OHDA: sag-amplitude = 13.5 ± 0.96 mV, p = 0.1395, Mann-Whitney test). In contrast,
233 a significant, about 5-fold increase of pacemaker irregularity expressed as CV was detected (Fig.2N,
234 vehicle: CV = 6.5 ± 0.7 %; 6-OHDA: CV = 33.9 ± 5.8; p = 0.0007, Mann-Whitney test). Detailed
235 observation of the raw traces revealed that the increased CV was mainly mediated by a combination
236 of intermittent phases of firing failure, similar to the one shown in Fig. 2K, and episodes of higher
237 frequency firing (as quantified in the ISI distribution histogram, Suppl. Fig. 6H). We also showed that
238 these differences were preserved both in on-cell and whole-cell recordings indicating the latter did
239 not induce a differential bias in any of the two groups (e.g. different calcium buffering) (Suppl. Fig. 6
240 F-G).

241 In short, this data demonstrates functional alterations in DA SN neurons surviving three weeks after a
242 6-OHDA infusion. These neurons exhibited a compressed dynamic range, including a 10-fold reduction
243 of *in vivo* bursting. Furthermore, we observed a 5-fold decrease of *in vitro* cell-autonomous pacemaker
244 stability with intermittent failure of action potential firing. This compromised intrinsic *in vitro*
245 excitability likely contributes to the 10-fold reduction of high frequency *in vivo* firing.

246 In order to address the question of whether these altered properties represent stable adaptations or
247 reflect a transient state of damage, we also studied *in vivo* and *in vitro* electrophysiology of surviving
248 mSN DA neurons in the late phase after lesion, characterized by partial behavioral recovery of motor
249 functions.

250

251 Surviving mSN DA neurons in the late post-6-OHDA phase display full recovery of the *in vivo*
252 dynamic range associated with an accelerated *in vitro* pacemaker

253

254 We recorded and analyzed surviving mSN DA neurons in the late 6-OHDA phase analogous to the early
255 phase (compare Fig. 3A/I and Fig. 2A/I). In contrast to the early phase, we found no significant
256 differences in the electrophysiological *in vivo* properties between the post-lesional and vehicle-
257 infused groups in the late phase (compare Fig 3B with Fig. 3C). Among others (Suppl. Fig. 7), this
258 implies that mean firing frequencies, dynamic ranges, CV, SFB and burst rates did not differ in
259 chronically surviving mSN DA neurons compared to those in controls (Fig. 3E, vehicle: mean firing rate
260 = 6.9 ± 0.8 Hz; 6-OHDA: mean firing rate = 7.5 ± 1.1 Hz; $p = 0.6038$, Mann-Whitney test; Fig. 3F, vehicle:
261 CV = 54.9 ± 12.2% ; 6-OHDA: CV = 53.3 ± 12.6%, $p > 0.9999$, Mann-Whitney test; Fig. 3G, vehicle: SFB
262 = 20.2 ± 9.1%, 6-OHDA: SFB = 22.2 ± 8.9%, $p = 0.8784$, Mann-Whitney test; Fig. 3H, vehicle: burst rate
263 = 0.17 ± 0.08 Hz; 6-OHDA: burst rate = 0.30 ± 0.15 Hz, $p = 0.4308$, Mann-Whitney test). This suggests
264 that surviving mSN DA neurons show full recovery of their electrophysiological properties within 2-
265 months after the lesion. However, our *in vivo* results alone cannot distinguish between two scenarios:
266 first, a slow functional recovery process that eventually leads to return of the physiological activity
267 range or second, the return to the full dynamic firing range *in vivo* is more than simple repair to the
268 *status quo ante* but involves a homeostatic adaptation of the functional properties of the DA neuron
269 itself. To resolve this question, we also recorded the *in vitro* pacemaker properties of the surviving DA
270 mSN neurons in the late post-6-OHDA phase. Here, we found clear evidence for allostatic adaptation
271 of these DA neurons (i.e the presence of new homeostatic setpoint). When comparing intrinsic
272 pacemaker frequencies, we noticed that late 6-OHDA survivors discharged almost 2-fold faster
273 compared to vehicle-controls (compare Fig. 3J with 3K, Fig. 3M vehicle: firing rate = 1.7 ± 0.2 Hz; 6-
274 OHDA: firing rate = 2.7 ± 0.2 Hz, $p = 0.0035$, Mann-Whitney test). In contrast to speed, no significant
275 difference in pacemaker regularity was observed (Fig. 3N, vehicle: CV = 9.19 ± 1.30 %, 6-OHDA: CV =
276 16.10 ± 6.66 %, $p = 0.1245$, Mann-Whitney test). Also, the sag components and the rebound delay
277 were not significantly different (Fig 3O, vehicle: rebound delay = 512.8 ± 93.8 ms, 6-OHDA: rebound
278 delay = 375.0 ± 58.9 ms, $p = 0.1994$, Mann-Whitney test; Fig. 3P, vehicle: sag-amplitude = 16.4 ± 1.2
279 mV, 6-OHDA: sag-amplitude = 19.1 ± 0.9 mV, $p = 0.0528$, Mann-Whitney test). Other *in vitro* spike
280 features were also not significantly different between the two groups (Suppl. Fig. 8). This accelerated

281 pacemaker phenotype was also observed in metabolically intact DA neurons recorded in the on-cell
282 configuration but further accelerated in the whole-cell mode (Suppl. Fig. 8 F-G).

283 In summary, functional recovery of the *in vivo* dynamic firing range of surviving mSN DA neurons was
284 associated with homeostatic plasticity of pacemaking (i.e. an allostatic shift of pacemaker setpoint).
285 Surviving mSN DA neurons not only recovered from instable pacemaking at the early phase but
286 doubled their discharge rates in late phase.

287

288

289 Accelerated pacemaker caused by downregulation of Kv4.3 channels in late surviving mSN
290 DA neurons

291

292 As Kv4.3 A-type channels have been shown to be powerful regulators of DA pacemaker frequency
293 (Subramaniam, Althof, et al. 2014; Subramaniam, Kern, et al. 2014; Liss et al. 2001; Khaliq and Bean
294 2008; Tarfa, Evans, and Khaliq 2017), we tested their potential role for the observed pacemaker
295 acceleration in late phase DA mSN neurons by pharmacological occlusion experiments using 1µM
296 AmmTx3, a selective Kv4.3 channel blocker (see scheme Fig. 4A). The presence of 1µM AmmTx3 not
297 only accelerated discharge rates in both identified mSN DA neurons from vehicle- and 6-OHDA-infused
298 mice (see Fig. 4BC for representative cells; Fig. 4D for mapping) but, importantly, also eliminated
299 significant rate differences between the two treatment groups (Fig. 4E, vehicle: mean firing rate = 4.5
300 ± 0.2 Hz, 6-OHDA: mean firing rate = 4.8 ± 0.3 Hz, p = 0.285; Fig. 4 F, vehicle: CV = 7.8 ± 1.3 %, 6-OHDA:
301 CV = 5.5 ± 0.4 %, p = 0.2517; both Mann-Whitney test). This result demonstrated that differences in
302 Kv4.3 channel function were the main driver of the late post-6OHDA accelerated pacemaker
303 phenotype. In addition, 1µM AmmTx3 also abolished the more subtle differences in rebound delays
304 and sag amplitudes (Fig. 4G, vehicle: rebound delay = 31.7 ± 2.4 ms, 6-OHDA: rebound delay = 28.4 ±

305 4.0 ms, p = 0.0952; Fig. 4H. vehicle: sag-amplitude = 15.6 ± 1.1 mV, 6-OHDA: sag-amplitude = 16.4 ±
306 0.9 mV, p = 0.7434; both Mann-Whitney test, Suppl. Fig. 9). In summary, these experiments
307 demonstrated that reduced Kv4.3 channel function in post-6-OHDA late phase DA mSN neurons had
308 a causal role in the phenotype of accelerated *in vitro* pacing.

309 To directly quantify the gating properties of transient outward (A-type) potassium currents mediated
310 by Kv4.3 channels, we carried out whole-cell voltage-clamp recordings (see scheme Fig. 4I-O). As
311 reported before (Liss et al. 2001), voltage-steps from negative holding potentials to the relevant
312 subthreshold range (e.g. -60 mV to -30 mV) activated large, fast inactivating outward currents in the
313 range of 1-10 nA in vehicle injected controls. In contrast, the same voltage steps activated smaller fast-
314 inactivating outward currents in post-6-OHDA late phase DA mSN neurons. These experiments
315 demonstrated about 50% smaller maximal A-type Kv4.3 potassium currents in late surviving DA mSN
316 neurons from 6-OHDA-treated mice compared to vehicle-treated controls (Fig. 4 M. vehicle: Kv4.3
317 channel current at -30mV = 3.8 ± 0.4 nA , 6-OHDA: Kv4.3 channel current at -30mV = 1.7 ± 0.3 nA, p <
318 0.0001, Mann-Whitney test). When comparing voltage-dependent gating parameters, we found no
319 changes in the biophysical channel properties apart from differences in the slope of the steady-state
320 activation curves (Fig. 4M, Suppl. Fig. 10 A-C).

321 By comparison, recordings of HCN currents in whole-cell voltage-clamp recordings showed no
322 differences in current amplitudes between the groups (Fig. 4N, vehicle: ΔHCN = 90.8 ± 10.7 pA, 6-
323 OHDA: ΔHCN = 94.9 ± 19.1 pA, p = 0.7375, Mann-Whitney test). These results substantiated the
324 selective role of reduced Kv4.3 function in causing the accelerated pacemaker in the post-6-OHDA late
325 phase surviving mSN DA neurons. As the reduction of Kv4.3 function might be caused by a number of
326 different mechanisms, including e.g. reduced protein expression and/or membrane delivery of Kv4.3
327 subunits as well as post-translational modifications of existing Kv4.3 channel complexes (e.g.
328 phosphorylation, redox-modification), we decided to assess Kv4.3 protein expression via
329 immunohistochemistry.

330 We performed Kv4.3 immunohistochemistry and confocal imaging in vehicle and 6-OHDA treated mice
331 both on the ipsilateral and contralateral infusion side (see scheme in Fig. 5A). We defined DA-selective
332 ROIs by using TH-immunopositive areas to determine the intensity of Kv4.3-immunosignals exclusively
333 within DA neurons (i.e. TH-signal based mask) (Subramaniam, Althof, et al. 2014). Figure 5B and 5C
334 compare Kv4.3-immunoreactivities in the midbrain between the contralateral control side and the
335 affected ipsilateral side during the late post-6-OHDA phase. Ipsilateral post-lesional TH-positive
336 neurons showed reduced Kv4.3-immunosignals compared to the control side. Semi-quantitative
337 comparison of TH-ROIs of the entire SN between contralateral control side and 6-OHDA-treated side
338 revealed a significant reduction of average Kv4.3-immunosignal on the 6-OHDA treated side of about
339 25% (Figure 5D, contralateral side $n = 4004$, ipsilateral side, $n = 2645$, $D = 0.2014$, $p < 0.0001$, two-
340 sample Kolmogorov–Smirnov test). A more detailed analysis of regional differences within the SN
341 revealed that the reduction in Kv4.3 immunoreactivity was significant for the medial SN (Figure 5E,
342 contralateral side, $n = 4004$: 73.03 ± 0.39, ipsilateral side, $n = 2645$: 54.8 ± 0.49, $p < 0.0001$, unpaired
343 t-test), where we recorded Kv4-currents, but even more pronounced in the lateral parts of the SN
344 (Suppl. Fig. 11C). As Kv4.3 channel subunits are expected to be mainly located on the cell membrane,
345 we also investigated whether Kv4.3-immunosignals were differentially distributed across cell
346 compartments. A robust, about 17% reduction of Kv4.3-immunosignals was observed in ipsilateral
347 post-lesional TH-positive neurons both for cell membrane and cytoplasm ROIs (Suppl. Fig. 11D). In
348 contrast, analogous quantification in vehicle-treated mice revealed no contra-ipsilateral differences
349 in Kv4.3-immunoreactivity (Suppl. Fig. 11 E-F). In summary, these immunohistochemical experiments
350 provided evidence for a reduced expression of Kv4.3 channel proteins in late post-6OHDA mSN DA
351 neurons. Reduced Kv4.3 protein expression is consistent with a reduction of functional Kv4.3 channels
352 in surviving mSN DA neurons as described above and suggests that pacemaker acceleration is
353 mediated by a reduced number of Kv4.3 channels.

354 ## Discussion

355

356 Our study provides the first combined *in vitro* & *in vivo* electrophysiological characterization of
357 identified DA neurons in the substantia nigra surviving a partial 6-OHDA lesion. Studying these
358 surviving SN DA neurons at two time points, we discovered time-dependent post-6-OHDA-selective
359 differences of firing properties both *in vivo* and *in vitro*. Early after lesion, and coinciding with
360 prominent behavioral impairments, we detected a selective and dramatic (about 10-fold) reduction
361 of *in vivo* burst firing in identified surviving SN DA neurons. This is reminiscent of an early study by
362 Hollermann & Grace (Hollerman and Grace 1990), who reported reduced bursting in putative SN DA
363 neurons one week after a partial lesion. Considering the Berretta et al 2005 study (Berretta et al.
364 2005), these early electrophysiological effects may reside from 6-OHDA triggering a cascade of events,
365 e.g. hyperpolarization via activation of K-ATP channels. At this early time point, we also found unstable
366 and more irregular *in vitro* pacemaker activity in these cells, with no differences in mean firing rates,
367 compared to those from vehicle-infused controls.

368 Conversely, at a later post-lesion time point (>2 months), when partial motor recovery had occurred,
369 we detected no differences in the *in vivo* firing range – including high frequency bursts– between
370 surviving SN DA neurons post-6-OHDA and those from vehicle-infused mice. Surprisingly, the *in vitro*
371 pacemaker rates in post-6-OHDA DA survivors were not only stable but almost twice as fast compared
372 to those from vehicle-controls. Finally, we pinpointed functional and protein Kv4.3 channel
373 downregulation as the leading cause for this chronic post-lesional pacemaker acceleration, while the
374 HCN channel function remained relatively stable. In essence, we identified a slow recovery of the
375 dynamic *in vivo* firing range of surviving post-lesional DA SN neurons, linked to an allostatic
376 acceleration of the intrinsic pacemaker by Kv4.3 channel downregulation.

377 Our results suggest a simple homeostatic scheme, where reducing the population size of DA SN
378 neurons by half is at least in part compensated by a two-fold increase of pacemaker speed in the

379 remaining half of the DA SN cell population. Given the 10-fold reduction of *in vivo* bursting in the initial
380 period after the lesion, it further suggests that the pacemaker setpoint rate is coupled to the *in vivo*
381 high frequency burst rate in DA mSN neurons. It is possible that a burst-related calcium signal might
382 be detected and integrated over time to control pacemaker rate via e.g. tuning Kv4.3 expression.
383 Recent studies have implicated the mitochondrial calcium uniporter (MCU) in coupling bursts to
384 mitochondrial Ca^{2+}, acting as a calcium sensor for neuronal firing rate homeostasis (Katsenelson et al.
385 2022). Future mechanistic studies will be necessary to investigate how *in vivo* bursting and intrinsic
386 pacemaking are coupled in distinct DA subpopulations. It is however interesting to note that the very
387 first descriptive study of in vivo SN DA firing patterns had already found a positive correlation between
388 the degree of in vivo burst firing and single spike firing rate (A. A. Grace and Bunney 1984). In
389 agreement with this proposal, it was also previously found that an about 4-fold-reduction of *in vivo*
390 burst rate via DA-selective NR1 knockout resulted in a scaled reduction of *in vivo* firing rate (Zweifel
391 et al. 2009).

392 In contrast to the homeostatic role of flexible Kv4.3 expression identified in this study, we previously
393 identified Kv4.3 channels in SN DA neurons as a pathophysiological target in a transgenic mutant
394 (A53T-SNCA) α-synuclein mouse model (without cell loss) (Subramaniam, Althof, et al. 2014). In this
395 model, we found a pacemaker acceleration caused by oxidative impairment of Kv4.3 channels.
396 However, the activity of SN DA neurons in the α-synuclein model was accelerated also *in vivo.* Thus,
397 mutant α-synuclein expression also caused a shift of the *in vivo* firing range of SN DA neurons towards
398 higher frequency. While Kv4.3 subunits were downregulated at the protein level in post-lesional SN
399 DA neurons, mutant α-synuclein induced oxidative Kv4.3 dysfunction as well as protein upregulation
400 (Subramaniam, Althof, et al. 2014). It will be interesting to test in follow up studies if and how α-
401 synuclein pathology affects firing and burst rate homeostasis in DA SN neurons.

402 Beyond pacemaker adaptations in surviving SN DA neurons, we assume that their chronic *in vivo*
403 electrophysiological phenotype might also be reshaped by network level plasticity in response to
404 dopamine-depletion.

405 Our finding that the mean *in vivo* discharge rates were not different to controls in the presence of an
406 accelerated intrinsic pacemaker strongly suggests a shift of the synaptic excitation-inhibition (E-I)
407 balance towards more inhibition. Numerous studies have found altered synaptic inhibition in the
408 dopamine-depleted basal ganglia (recently reviewed in (Zhang et al. 2021)). In particular, Heo and
409 colleagues recently demonstrated a chronic E-I balance shift toward more inhibition across several PD
410 models including 6-OHDA (Heo et al. 2020). They identified a substantial contribution of additional
411 GABA synthesis and release from reactive astrocytes in the midbrain. It has also been well-established
412 that basal ganglia GABA neurons fire in more synchronized hence more effective fashion after DA
413 depletion (Cagnan, Duff, and Brown 2015; Milosevic et al. 2018; Phillips et al. 2020; Tinkhauser et al.
414 2020; Wichmann, Bergman, and DeLong 2018; Evans et al. 2020). This has recently been confirmed by
415 elegant *in vivo* single cell resolved studies using either gCAMP-based calcium monitoring or *in vivo*
416 patch-clamp approaches (Ketzef et al. 2017; Kravitz et al. 2010; J. G. Parker et al. 2018; P. R. L. Parker,
417 Lalive, and Kreitzer 2016; Sitzia et al. 2020). The accelerated pacemaker in response to enhanced net
418 inhibition would also be expected within the framework of homeostatic plasticity (Turrigiano 2012).

419 Our study has several limitations. First, we explored a single-hit, non-progressive partial lesion model,
420 which needs to be differentiated from *state-of-the-art* PD rodent models, which develop disease-
421 relevant α-synuclein pathology and show progressive loss of DA SN neurons (Thakur et al. 2017).
422 Second, we do not differentiate between DA SN subtypes. We recently showed that lateral SN DA
423 neurons projecting to DLS possess a distinct *in vivo* firing phenotype compared to medial SN DA
424 neurons projecting to either DLS or DMS in mice (Farassat et al. 2019). Therefore, recording from
425 lateral DA SN population in lesion models would be important. However, in our current partial 6-OHDA
426 lesion model, these lateral SN DA neurons were too severely lost to allow for more than anecdotal
427 post-lesion electrophysiological analysis (see Fig. 3). A milder version of the current model would be
428 needed to identify their properties and responses to partial lesion. Regarding the surviving DA neuron
429 in the medial SN, we previously showed that they have distinct projection targets including DLS, DMS
430 and lateral shell of nucleus accumbens (Farassat et al. 2019). In the current study, we have not aimed
431 for identification of axonal projections to avoid potentially confounding effects of additional brain

432 surgery. Nevertheless, this important issue should be addressed in follow-up studies by e.g. molecular
433 subtyping approaches (Heymann et al. 2020; Poulin et al. 2018; Saunders et al. 2018). Third, we are
434 aware that *in vivo* recordings carried out in isoflurane do not display the full dynamic spectrum of DA
435 SN firing compared to awake, freely moving animals (we have discussed the aspect extensively in
436 Farassat et al. 2019).

437 Finally, we would like to speculate about the possible implications of our findings for PD. In principle,
438 cell-loss induced pacemaker plasticity, as identified here, might have a dual nature. On one hand, they
439 might render the surviving DA SN neurons more robust in defending their phenotype and function. On
440 the other hand, the allostatic pacemaker acceleration may amplify the innate vulnerability of an
441 already at baseline metabolically and oxidatively challenged neuron type. The latter would be an
442 extension of the "stressful pacemaker" hypothesis of DA vulnerability (Chan et al. 2007; Surmeier
443 2007; Surmeier, Obeso, and Halliday 2017; Surmeier, Halliday, and Simuni 2017) with its potential
444 clinical implications(Guzman et al. 2018; Liss and Striessnig 2019; Ortner et al. 2017; Ortner 2021; The
445 Parkinson Study Group STEADY-PD 2020) . In summary, we identified the homeostatic capacity and
446 pacemaker allostasis of surviving DA SN neurons in response to cell loss.

447 # Methods

448 ## Animals

449 Male and female C57Bl6/N mice (Charles River Laboratories) were used for the study. The mice were
450 8 weeks old, group housed and maintained on a 12-hour light-dark cycle. All experiments and
451 procedures involving mice were approved by the German Regierungspräsidium Darmstadt (V54-
452 19c20/15-F40/30). In total, 152 mice were used for this study (see table below).

	Early phase		**Late phase**	
	Mice (#)	Cells (#)	Mice (#)	Cells (#)
***In vivo* juxta & behavior – vehicle**	15	12 – medial/ 28 – all	12	10 – medial/ 26 – all
***In vivo* juxta & behavior – 6-OHDA**	16	9 – medial/ 16 – all	10	9 – medial/ 11 – all
***In vitro* – vehicle**	3	16	3	12
***In vitro* – 6-OHDA**	6	37	5	25
***In vitro* & AmmTx3 – vehicle**	-	-	3	15
***In vitro* & AmmTx3 – 6-OHDA**	-	-	3	14
***In vitro* voltage clamp experiments – vehicle**	-	-	3	17
***In vitro* voltage clamp experiments – 6-OHDA**	-		3	15
Female behavior experiments – vehicle, 6-OHDA	-		10	
Female histology – vehicle, 6-OHDA	-		8	
6-OHDA dose response	12			
	Mice (#)		Mice (#)	
Kv4.3 Immunochemistry	8		8	
SN quantification – vehicle	9		3	
SN quantification – 6-OHDA	9		3	
Sum = 152				

453

454 ## Stereotactic 6-OHDA infusion

455 All surgeries were performed under general anesthesia in areflexic state. Prior to the induction of
456 anesthesia, a premedication of 0.2 mg/kg atropine (atropine-sulfate, Braun Melsungen AG,

457 Melsungen) was given as an intraperitoneal (i.p.) injection to stabilize circulation. Anesthesia was
458 induced in a plastic chamber, which was flooded with 5% Isoflurane (Florene®, AbbVie Deutschland
459 GmbH & Co. KG, Ludwigshafen, Germany) in pure oxygen (0.4 l/min). For maintenance of anesthesia,
460 isoflurane was delivered through a breathing mask with a flow rate of 0.35 l/min and its concentration
461 was regulated to 1.5-2.2% using an adjustable vaporizer (Uno, Zevenaar, Netherlands). The depth of
462 anesthesia was controlled by testing the toe pinch reflex and the breathing rate (1-2Hz). Body
463 temperature (36°C) and respiration were constantly monitored. Lidocaine/prilocaine ointment (25
464 mg/g, Emla® creme, AstraZeneca GmbH, 22876 Wedel) was applied prior to surgery and after suturing
465 of the wound as local anesthetics. Additional analgesia was provided by subcutaneous injection of
466 carprofen (4 mg/kg in NaCl, Rimadyl®, Pfilzer GmbH, Berlin, Germany) after infusion. Eye lubricant
467 (Visidic, Bausch and Lomb, Berlin, Germany) was used to protect eyes from desiccation.

468 Desipramine hydrochloride (20 mg/kg, Sigma Aldrich) was injected i.p. 20-40 min before intracranial
469 infusions to prevent 6-OHDA uptake by noradrenergic neurons. The desipramine solution was
470 prepared in sterile, isotonic NaCl solution (B. Braun Melsungen AG, Germany) at the day of surgery.
471 The infusion solutions are based on sterile artificial cerebrospinal fluid (ACSF, Harvard Apparatus,
472 Holliston, MA, USA) with 0.02% L-ascorbic acid (used also as a vehicle solution). The 6-OHDA solution
473 (0.2% 6-hydroxydopamine hydrochloride in ACSF with 0.02% L-ascorbic acid) was prepared at the day
474 of infusion, stored on ice, and shielded from light.

475 During surgery, the animals were placed on a heating pad and were fixed in a stereotactic frame
476 (Model 1900, Kopf Instruments, Tujunga, USA) with a stereotactic arm and a connected three-way
477 digital positioning display. The scalp was opened by a longitudinal cut to expose the skull with bregma
478 and lambda on display. With a centering scope (Model 1915, Kopf Instruments, Tujunga, USA), the
479 bregma-lambda distance was measured and examined for suitable anatomy (4.4 ± 0.2 mm distance).
480 Afterwards, the skull was aligned to a reference frame with a stereotaxic alignment indicator (Model
481 1905, Kopf Instruments, Tujunga, USA) and the manipulator system was referenced to bregma.

482 Using a stereotaxic drill (Model 1911, Kopf Instruments, Tujunga, USA) with a 500 µm diameter drill
483 bit, a hole above the right striatum was drilled (coordinates: ML: +1.9 mm, AP: +0.5 mm to bregma).
484 ACSF or 6-OHDA solution were loaded to a 10 µl NanoFil syringe (World Precision Instruments Inc.,
485 Sarasota, FL, USA) with a 35G blunt needle, which was mounted on a MicroSyringe Pump (UMP3-1,
486 World Precision Instruments) and controlled by a SYSMicro4 Controller (World Precision Instruments).
487 Using the stereotactic arm, the needle was slowly lowered (about 750 µm/min) to a position of -2.2
488 mm below the brain surface (infusion site coordinates: ML: +1.9 mm, AP: +0.5 mm, DV: -2.2 mm to
489 bregma). Anatomical references are based on Franklin and Paxinos (2008). A volume of 6 µl was
490 infused with a flow rate of 250 nl/min. Once the volume was infused, the needle rested for 5 minutes
491 in that position before it was slowly moved out of the brain. Directly before and after infusion, proper
492 functioning of the syringe system and the needle was checked. Finally, after suture the animal was
493 placed on a heating pad for full recovery. Oats, wet food pallets and water were placed inside the cage
494 to ease consumption.

495

496 ## Behavioral testing

497 ### *Open field*

498 Spontaneous locomotion (track length, wall distance, time in center and number of rearings) and
499 rotations of all mice were monitored in open field (50 × 50 cm, center 30 × 30 cm; red illumination, 3
500 lx) for 10 min in 3 baseline sessions and every 4th or 7th day post-infusion of ACSF/6-OHDA till the day
501 of *in vivo* or *in vitro* experiment (e.g. 21st or >68th post-operative day). The open field was cleaned
502 before and after each mouse with 0,1% acetic acid in distilled water. Using a video tracking system
503 (Viewer II/III, Biobserve) spontaneous behavior was recorded and analyzed both online and offline.
504 Data was extracted from Viewer as Excel-tables and the final analysis was made with custom made
505 Matlab-scripts.

506

507 *Cylinder test*

508 Forelimb use during explorative activity was explored with cylinder test. The test was performed at
509 corresponding termination time point (20-21st and 64th post-infusion day). Mice were placed
510 individually in a glass beaker (9 cm diameter, 19 cm height) at room light and were video recorded
511 with a camera (Logitech HD Webcam C615) for about 5 min. No habituation was allowed before video
512 recording. The glass cylinder was cleaned before and after every mouse with 0,1% acetic acid in
513 distilled water. Only weight-bearing wall contacts made by each and both forelimb on the cylinder
514 wall were scored. Wall exploration was expressed in terms of the percentage of contralateral to the
515 infusion side (in the 6-OHDA-infused mice also impaired forepaw) to all forelimb wall contacts.

516

517 ## *In vivo* electrophysiology

518 *Extracellular recording*

519 *In vivo* extracellular single-unit activities of SN and VTA neurons were recorded in ACSF-infused
520 (vehicle) and 6-OHDA-infused mice, similar procedures were used in other studies from our lab
521 (Farassat et al. 2019; Schiemann et al. 2012; Subramaniam, Althof, et al. 2014). Briefly, mice were
522 anesthetized (isoflurane; induction 4.5-5%, maintenance 1–2% in 0.4 l/min O2) and placed into a
523 stereotactic frame. The craniotomies were performed as described above to target the lateral SN (AP:
524 -3.08 mm, ML: 1.4 mm) and medial SN (AP: -3.08 mm, ML: 0.9 mm). Borosilicate glass electrodes (10–
525 25 MΩ; Harvard Apparatus, Holliston, MA, USA) were made using a horizontal puller (DMZ-Universal
526 Puller, Zeitz, Germany) and filled with 0.5 M NaCl, 10 mM HEPES (pH 7.4) and 1.5% neurobiotin (Vector
527 Laboratories, Burlingame, CA, USA). A micromanipulator (SM-6; Luigs & Neumann, Ratingen,
528 Germany) was used to lower the electrodes to the recording site. The single-unit activity of each
529 neuron was recorded for at least 10 minutes at a sampling rate of 12.5 kHz (for firing pattern analyses),
530 and then for another one minute at a sampling rate of 20 kHz (for the fine analysis of AP waveforms).
531 Signals were amplified 1000x (ELC-03M; NPI electronics, Tamm, Germany), notch- and bandpass-
532 filtered 0.3–5000 Hz (single-pole, 6 dB/octave, DPA-2FS, NPI electronics) and recorded on a computer

533 with an EPC-10 A/D converter (Heka, Lambrecht, Germany). Simultaneously, the signals were
534 displayed on an analog oscilloscope and an audio monitor (HAMEG Instruments CombiScope HM1508;
535 AUDIS-03/12M NPI electronics). Midbrain DA neurons were initially identified by their broad biphasic
536 AP (> 1.2 ms duration) and slow frequency (1–8 Hz) (Anthony A. Grace and Bunney 1984; Ungless and
537 Grace 2012). AP duration was determined as the interval between the start of initial upward
538 component and the minimum of following downward component.

539

540 *Juxtacellular labeling of single neurons*

541 In order to identify the anatomical location and neurochemical identity of the recorded neurons, they
542 were labeled post-recording with neurobiotin using the juxtacellular *in vivo* labeling technique (Pinault
543 1996). Microiontophoretic currents were applied (1–10 nA positive current, 200ms on/off pulse, ELC-
544 03M, NPI Electronics) via the recording electrode in parallel to the monitoring of single-unit activity.
545 Labeling was considered successful, when: the firing pattern of the neuron was modulated during
546 current injection (i.e., increased activity during on-pulse and absence of activity in the off-pulse), the
547 process was stable for at least 20s, and was followed by the recovery of spontaneous activity. This
548 procedure allowed for the exact mapping of the recorded DA neuron within the SN and VTA subnuclei
549 (Franklin and Paxinos 2012) using custom written scripts in Matlab (MathWorks, Natick, MA, USA),
550 combined with neurochemical identification using TH-immunostaining.

551

552 ## *In vitro* electrophysiology

553 *Slice preparation*

554 Animals were anesthetized by intraperitoneal injection of ketamine (250 mg/kg, Ketaset, Zoetis) and
555 medetomidine-hydrochloride (2.5 mg/kg, Domitor, OrionPharma) prior to intracardial perfusion using
556 ice-cold ACSF consisting of the following (in mM): 50 sucrose, 125 NaCl, 2.5 KCl, 25 NaHCO3, 1.25
557 NaH2PO4, 2.5 glucose, 6 MgCl2, 0.1 CaCl2 and 2.96 kynurenic acid (Sigma-Aldrich), oxygenated with

558 95% O2 and 5% CO2. Rostral coronal midbrain slices (bregma: -2.92 mm to -3.16 mm) were sectioned
559 at 250 µm using a vibrating blade microtome (VT1200s, Leica). Slices were incubated for 1 h before
560 recordings in a 37°C bath with oxygenated extracellular solution with extra 1µM AmmTx3, containing
561 the following (in mM): 22.5 sucrose, 125 NaCl, 3.5 KCl, 25 NaHCO3, 1.25 NaH2PO4, 2.5 glucose, 1.2
562 MgCl2 and 1.2 CaCl2.

563

564 *In vitro patch-clamp recordings*

565 Slices were placed in a heated recording chamber (37°C) that was perfused with oxygenated
566 extracellular solution at 2-4 ml min_{-1}. CNQX (20 µM; Biotrend), gabazine (SR95531, 4 µM; Biotrend)
567 DL-AP5 (10 µM; Cayman Chemical) were added to inhibit excitatory and inhibitory synaptic
568 transmission. For voltage clamp recordings, TTX (500nM; Tocris) was added to the extracellular
569 solution. Neurons were visualized using infrared differential interference contrast videomicroscopy
570 with a digital camera (VX55, Till Photonics) connected to an upright microscope (Axioskop 2, FSplus,
571 Zeiss). Patch pipettes were pulled from borosilicate glass (GC150TF-10; Harvard Apparatus LTD) using
572 a temperature-controlled, horizontal pipette puller (DMZ-Universal Puller, Zeitz). Patch pipettes (4-6
573 MΩ) were filled with a solution containing the following (in mM): 135 KGlu, KCl, 10 HEPES, 0.1 EGTA,
574 5 MgCl2, 0.075 CaCl2, 5 NaATP, 1 LiGTP, 0.1% neurobiotin, adjusted to a pH of 7.35 with KOH.
575 Recordings were performed using an EPC-10 patch-clamp amplifier (Heka electronics) with a sampling
576 rate of 20 kHz and a low-pass filter (Bessel, 5 kHz). For voltage clamp recordings only experiments with
577 uncompensated series resistance <10MO were included in this study and series resistance was
578 electronically compensated 75%. Neurons were held at a holding potential of -40mV to minimize HCN
579 activation. To determine Kv4.3 activation kinetics neurons were hyperpolarized to -80mV for 500ms
580 followed by varying voltage steps from -60mV to -20mV in increments of 5mV for 1s. For inactivation
581 kinetics neurons were hyperpolarized from -120mV to -20mV in increments of 10 mV for 1s followed
582 by a fixed voltage step to -20mV for 1s. For analysis of HCN currents neurons were hyperpolarized

583 from -80mV to -120mV in increments of 20mV for 1s. For analysis, action potential thresholds (mV)
584 were determined at $dV_m/dt > 10$ mV/ms.

585 ## Immunohistochemistry

586 Following *in vivo* recordings, animals were transcardially perfused, as described previously (Farassat
587 et al. 2019; Schiemann et al. 2012; Subramaniam, Althof, et al. 2014). Fixed brains were sectioned into
588 60µm (midbrain) or 100µm (forebrain) coronal sections using a vibrating microtome (VT1000S, Leica).
589 *In vitro* slices were fixed in paraformaldehyde after finishing the experiment. Sections were rinsed in
590 PBS and then incubated (in blocking solution (0.2 M PBS with 10% horse serum, 0.5% Triton X-100,
591 0.2% BSA). Afterwards, sections were incubated in carrier solution (room temperature, overnight)
592 with the following primary antibodies: polyclonal guinea pig anti-tyrosine hydroxylase (TH; 1:1000;
593 Synaptic Systems), monoclonal mouse anti-TH (1:1000; Synaptic Systems) or polyclonal rabbit anti-TH
594 (1:1000; Synaptic Systems); mouse anti-Kv4.3 (1:1000, Alomone Labs). In sequence, sections were
595 again washed in PBS and incubated (room temperature, overnight) with the following secondary
596 antibodies: goat anti-guinea pig 488, goat anti-rabbit 488, goat anti-mouse 488, goat anti-mouse 568
597 (all 1:750; Thermofisher). Streptavidin AlexaFluor-568 and Streptavidin AlexaFluor-488 (both 1:1000;
598 Invitrogen) were used for identifying neurobiotin-filled cells. Sections were then rinsed in PBS and
599 mounted on slides with fluorescent mounting medium (Vectashield, Vector Laboratories).

600

601 ## DAB immunocytochemistry

602 For DAB (3,3'-diaminobenzidine) staining procedures, a Vectastain ABC Staining Kit (Vector
603 Laboratories) was used. Coronal sections of midbrain (30 µm) areas were cut and rinsed in PBS (3x10
604 min). Similar to previous immunolabeling procedures, unspecific antigen binding sites were blocked
605 by incubation of the sections with blocking solution (60 min, room temperature). Subsequently,
606 sections were incubated with primary antibody against TH (rabbit anti TH) overnight, rinsed in PBS
607 (3x10 min), and were incubated with biotinylated secondary antibodies (biotinylated anti-rabbit) for

608 two hours at RT. In parallel, an avidin-biotin complex (ABC) was formed by pre-incubation of avidin
609 (1:1000) with biotinylated HRP (1:1000) in PBS for two hours at room temperature. Sections were
610 rinsed in PBS (3x10 min) prior to incubation with ABC solution (60 min, room temperature). Next,
611 sections were rinsed in PBS (2x10 min) and Tris-buffer (1x10 min). Finally, DAB oxidation was
612 developed by application of 2 % H_2O_2, 2 % $NiCl_2$ and 4 % DAB in Tris-buffer using a DAB Substrate Kit
613 (Vector Laboratories, Burlingame, USA). $NiCl_2$ enhances sensitivity and intensity of DAB precipitation
614 product. DAB oxidation was developed for 2 to 5 minutes and was stopped with Tris-buffer once a
615 specific high-contrast signal was detectable. Sections were rinsed in Tris-buffer (3x10 min) and
616 transferred onto gelatin-covered slides, air-dried overnight, and dehydrated in consecutive ascending
617 alcohol concentrations (50 %, 70 %, 90 % and 2x 100 %; 10 min each) followed by dehydration in xylol
618 (2x 100 %; 10 min each). Finally, sections were mounted under glass coverslips with hardening
619 mounting medium (Vectamount, Vector Laboratories, Burlingame, USA).

620

621 ## Unbiased stereology measurements

622 For quantification of total cell loss, TH-DAB labeled SN DA neurons were counted using unbiased
623 stereology based on optical dissection (Gundersen 1986). In coronal sections (30 µm), the region of
624 interest was selected based on anatomical landmarks including the medial lemniscus, which separates
625 SN and adjacent VTA. Stereological counting provides unbiased data based on random, systematic
626 sampling using an optical fractionator. This method involves counting of neurons with an optical
627 dissector, a three-dimensional probe placed through a reference space (Gundersen 1986). The optical
628 dissector forms a focal plane with a thin depth of field through the selected sections. Objects in focus
629 of this focal plane are located within the reference section and are counted, while objects outside of
630 the focal plane are not counted. On top of the optical dissector, a counting frame is applied. Counting
631 frames ensure that all neurons have equal probabilities of being selected, regardless of shape, size,
632 orientation, and distribution. To avoid counting capped neurons at the border of a section, an
633 additional guard zone was deployed at the upper and lower borders of each section. DA neurons

634 within the counting frame as well as those crossing the green line (acceptance line) were counted,
635 while DA neurons crossing the red line (rejection line) excluded. Moreover, only neurons with a
636 detectable nucleus in focus within the optical dissector were counted. For quantification of total cell
637 loss, StereoInvestigator software (V5, MicroBrightField, Colchester, USA) was used in combination
638 with BX61 microscope (Olympus, Hamburg, Germany). The region of interest was selected and marked
639 using a low magnification objective lens (2x, NA 0.25, Olympus) and 12-30 serial sections of 30 µm
640 thickness were counted, covering the entire caudo-rostral extent of the SN. To count the number of
641 DA neurons in the area of the SN pars compacta, a high magnification oil-immersion objective lens
642 (100x, NA 1.30, Olympus) (counting frame, 50 × 50 µm; sampling grid, 125 × 100 µm) was used. After
643 counting was finished, the total number of neurons was calculated by the software using the formula
644 described by West et al (West 1993).

645

646 ## Optical density measurements

647 Optical density measurements of TH-DAB labeled striatal sections were performed using ImageJ
648 software (http://rsbweb.nih.gov/ij/). Following TH-DAB labeling and TH-immunohistochemistry,
649 images of five coronal sections (100 µm) covering the rostrocaudal axis of the striatum were captured
650 using laser-scanning microscope (Nikon Eclipse90i, Nikon GmbH). Images were gray scale converted
651 and mean gray values of desired striatal areas were encircled and measured. Unspecific mean gray
652 values were measured in a defined cortical area (100x100 pixels) that displayed no specific TH signal
653 due to the absence of DA innervation and were subtracted. The ventral edge of lateral ventricles
654 served as an anatomical landmark to separate dorsal and ventral areas. For all animals, the
655 measurement from the ipsilateral to the infusion side were divided by the contralateral side to
656 calculate the relative optical density of the striatum.

657

658 ## Immunohistochemical Kv4.3 channel signal quantification

659 A Nikon Eclipse 90i microscope was used for fluorescent signal detection, excitation wavelength of
660 488 nm for TH-signal and 568 nm for Kv4.3-channel signal. From each animal, 4 midbrain slices
661 covering the caudal, intermedial and rostral regions, were selected and imaged for overview with 4x
662 magnification. Then 60x magnification was used to acquire data from 4 areas within each SN (4 images
663 on the ipsilateral and 4 images on the contralateral to infusion side). All images were acquired using
664 the same laser and camera settings. Images were exported from Nikon NIS-Elements Advanced
665 Research (Version 4.20.03) software as 8-bit TIFF files for quantification. Data was analyzed using
666 custom made Python 3.0 scripts with matplotlib, numpy, scimage and scipy modules. First, TH
667 immunosignals were converted to a binary image via Otsu-thresholding algorithm to detect TH areas
668 bigger than 400 pixels. Then, the resulting binary image was used as a mask for Kv4.3 channel
669 immunosignal detection. For all ROIs surface areas and mean Kv.4.3 channel signal intensity was
670 measured. By applying erosion and dilatation algorithms on the ROIs, membrane and cytoplasm areas
671 were segregated, allowing isolation of Kv4.3 channel immunosignal intensity for these cell
672 compartments. Background Kv4.3 channel immunosignal was quantified in TH-immunosignal areas
673 below the Otsu-threshold. All data were then grouped according to medio-lateral and ipsi-
674 /contralateral position for both vehicle and 6-OHDA group. Graphs and statistical analysis for this data
675 was performed using Python custom made scripts.

676

677 ## Statistical Analysis

678 ### *Spike train analyses*

679 Spike time-stamps were extracted by thresholding above noise levels with IgorPro 6.02 (WaveMetrics,
680 Lake Oswego, OR, USA). Firing pattern properties such as mean frequency, coefficient of variation (CV)
681 and bursting measures were analyzed using custom scripts in Matlab. In order to estimate burstiness
682 and intra-burst properties, we used the burst detection methods described in Grace & Bunney (A. A.
683 Grace and Bunney 1984; Anthony A. Grace and Bunney 1984; Ungless and Grace 2012). All non-burst

684 related ISIs (excluding all ISIs that followed the Grace and Bunney criteria, as well as all pre- and post-
685 burst ISIs) were used to calculate the single spike firing frequency and single spike coefficient of
686 variation.

687 For analysis of general firing patterns, autocorrelation histograms (ACH) were plotted using custom
688 Matlab scripts. We used established criteria for classification of *in vivo* firing patterns based on visual
689 inspection of autocorrelograms (Farassat et al. 2019; Schiemann et al. 2012; Subramaniam, Althof, et
690 al. 2014): single spike-oscillatory (≥3 equidistant peaks with decreasing amplitudes), single spike-
691 irregular (<3 peaks, increasing from zero approximating a steady state), bursty-irregular (narrow peak
692 with steep increase at short ISIs) and bursty-oscillatory (narrow peak reflecting fast intraburst ISIs
693 followed by clear trough and repetitive broader peaks).

694 ### Statistics

695 Categorical data is represented as stacked bar graphs. To investigate the assumption of normal
696 distribution, we performed the single-sample Kolmogorov-Smirnov test. The Mann-Whitney-Test,
697 one-/two-way ANOVA were performed in non-parametric data to determine statistical significance.
698 Categorical parameters, such as ACH-based firing pattern, were analyzed with the Chi-squared test.
699 Statistical significance level was set to $p < 0.05$. All data values are presented as means ± SEM.
700 Statistical tests were performed using GraphPad Prism 9 (GraphPad Software, San Diego, CA, USA),
701 Matlab and Python. The scatter plots are represented with median or mean ± SEM. The resulting p
702 values were compared with Bonferroni-corrected α-level or Tukey *post hoc* comparison. A value of p
703 ≤ 0.05 was considered to be statistically significant; $p \leq 0.05$ = *$p \leq 0.005$ = **$p \leq 0.0005$ = ***. Graphs
704 were plotted using GraphPad Prism software (9.0c), Matlab and Python.

705 ## Acknowledgements

706 This study was supported by research grants to JR (DFG, CRC 1451). LK is a MD/PhD candidate at
707 TransMed, Gutenberg University Mainz. We thank Beatrice Fischer and Jasmine Sonntag for technical
708 assistance, Alexander Prinz for preliminary data on post-6-OHDA stereology.

Additional information

Author contributions

LK & JR designed the study. LK performed the lesions, behavioral & *in vivo* electrophysiology, JS & JM performed the *in vitro* experiments. JZ performed dose response lesion and female experiments. Analysis was carried out jointly by LK, JZ, KMC, JO and JR. NF taught LK *in vivo* electrophysiology and juxtacellular labelling. LK & JR wrote the manuscript.

Declaration of Interests

The authors declare no conflict of interests.

Author ORCIDs

Jochen Roeper https://orcid.org/0000-0003-2145-8742

Lora Kovacheva https://orcid.org/0000-0001-6999-1533

Josef Shin https://orcid.org/0000-0002-3556-125X

Kauê Machado Costa https://orcid.org/0000-0002-5562-6495

Poonam Thakur https://orcid.org/0000-0002-4462-5550

Josefa Zaldivar-Diez https://orcid.org/0000-0003-2317-3898

Ethics

Animal experimentation: All experiments and procedures involving mice were approved by the German Regierungspräsidium Darmstadt (V54-19c20/15-F40/30).

References

Berretta, Nicola, Peter S. Freestone, Ezia Guatteo, Denis De Castro, Raffaella Geracitano, Giorgio Bernardi, Nicola B. Mercuri, and Janusz Lipski. 2005. “Acute Effects of 6-Hydroxydopamine on Dopaminergic Neurons of the Rat Substantia Nigra Pars Compacta in Vitro.” *NeuroToxicology* 26

731 (5): 869–81. https://doi.org/10.1016/j.neuro.2005.01.014.

732 Bez, Francesco, Veronica Francardo, and M. Angela Cenci. 2016. "Dramatic Differences in
733 Susceptibility to L-DOPA-Induced Dyskinesia between Mice That Are Aged before or after a
734 Nigrostriatal Dopamine Lesion." *Neurobiology of Disease* 94 (October): 213–25.
735 https://doi.org/10.1016/j.nbd.2016.06.005.

736 Cagnan, Hayriye, Eugene Paul Duff, and Peter Brown. 2015. "The Relative Phases of Basal Ganglia
737 Activities Dynamically Shape Effective Connectivity in Parkinson's Disease." *Brain* 138 (6): 1667–
738 78. https://doi.org/10.1093/brain/awv093.

739 Cenci, M. Angela, and Anders Björklund. 2020. "Animal Models for Preclinical Parkinson's Research:
740 An Update and Critical Appraisal." *Progress in Brain Research* 252: 27–59.
741 https://doi.org/10.1016/bs.pbr.2020.02.003.

742 Chan, C. Savio, Jaime N. Guzman, Ema Ilijic, Jeff N. Mercer, Caroline Rick, Tatiana Tkatch, Gloria E.
743 Meredith, and D. James Surmeier. 2007. "'Rejuvenation' Protects Neurons in Mouse Models of
744 Parkinson's Disease." *Nature* 447 (7148): 1081–86. https://doi.org/10.1038/nature05865.

745 Evans, Rebekah C., Emily L. Twedell, Manhua Zhu, Jefferson Ascencio, Renshu Zhang, and Zayd M.
746 Khaliq. 2020. "Functional Dissection of Basal Ganglia Inhibitory Inputs onto Substantia Nigra
747 Dopaminergic Neurons." *Cell Reports* 32 (11): 108156.
748 https://doi.org/10.1016/j.celrep.2020.108156.

749 Farassat, Navid, Kauê Machado Costa, Strahinja Stojanovic, Stefan Albert, Lora Kovacheva, Josef Shin,
750 Richard Egger, et al. 2019. "In Vivo Functional Diversity of Midbrain Dopamine Neurons within
751 Identified Axonal Projections." *ELife* 8 (October). https://doi.org/10.7554/eLife.48408.

752 Franklin, KBJ, and George Paxinos. 2012. *Paxinos and Franklin's The Mouse Brain in Stereotaxic*
753 *Coordinates. Elsevier*.

754 Grace, A. A., and B. S. Bunney. 1984. "The Control of Firing Pattern in Nigral Dopamine Neurons: Burst
755 Firing." *Journal of Neuroscience* 4 (11): 2877–90. https://doi.org/10.1523/jneurosci.04-11-
756 02877.1984.

757 Grace, Anthony A., and Benjamin S. Bunney. 1984. "The Control of Firing Pattern in Nigral Dopamine
758 Neurons: Single Spike Firing." *Journal of Neurosc* 4 (11): 2866–76.

759 Gundersen, H. J.G. 1986. "Stereology of Arbitrary Particles." *Journal of Microscopy* 143 (1): 3–45.
760 https://doi.org/10.1111/j.1365-2818.1986.tb02764.x.

761 Guzman, Jaime N., Ema Ilijic, Ben Yang, Javier Sanchez-Padilla, David Wokosin, Dan Galtieri, Jyothisri
762 Kondapalli, Paul T. Schumacker, and D. James Surmeier. 2018. "Systemic Isradipine Treatment
763 Diminishes Calcium-Dependent Mitochondrial Oxidant Stress." *Journal of Clinical Investigation*
764 128 (6): 2266–80. https://doi.org/10.1172/JCI95898.

765 Heo, Jun Young, Min Ho Nam, Hyung Ho Yoon, Jeongyeon Kim, Yu Jin Hwang, Woojin Won, Dong Ho
766 Woo, et al. 2020. "Aberrant Tonic Inhibition of Dopaminergic Neuronal Activity Causes Motor
767 Symptoms in Animal Models of Parkinson's Disease." *Current Biology* 30 (2): 276-291.e9.
768 https://doi.org/10.1016/j.cub.2019.11.079.

769 Heymann, Gabriel, Yong S. Jo, Kathryn L. Reichard, Naomi McFarland, Charles Chavkin, Richard D.
770 Palmiter, Marta E. Soden, and Larry S. Zweifel. 2020. "Synergy of Distinct Dopamine Projection
771 Populations in Behavioral Reinforcement." *Neuron* 105 (5): 909-920.e5.
772 https://doi.org/10.1016/j.neuron.2019.11.024.

773 Hollerman, Jeffrey R., and Anthony A. Grace. 1990. “The Effects of Dopamine-Depleting Brain Lesions
774 on the Electrophysiological Activity of Rat Substantia Nigra Dopamine Neurons.” *Brain Research*
775 533 (2): 203–12. https://doi.org/10.1016/0006-8993(90)91341-D.

776 Katsenelson, Maxim, Ilana Shapira, Eman Abbas, Kristina Jevdokimenko, Boaz Styr, Antonella
777 Ruggiero, Saba Aïd, et al. 2022. “IGF-1 Receptor Regulates Upward Firing Rate Homeostasis via
778 the Mitochondrial Calcium Uniporter.” *Proceedings of the National Academy of Sciences of the*
779 *United States of America* 119 (33): 1–10. https://doi.org/10.1073/pnas.2121040119.

780 Ketzef, M., G. Spigolon, Y. Johansson, A. Bonito-Oliva, G. Fisone, and G. Silberberg. 2017. “Dopamine
781 Depletion Impairs Bilateral Sensory Processing in the Striatum in a Pathway-Dependent
782 Manner.” *Neuron* 94 (4): 855-865.e5. https://doi.org/10.1016/j.neuron.2017.05.004.

783 Khaliq, Zayd M., and Bruce P. Bean. 2008. “Dynamic, Nonlinear Feedback Regulation of Slow
784 Pacemaking by A-Type Potassium Current in Ventral Tegmental Area Neurons.” *Journal of*
785 *Neuroscience* 28 (43): 10905–17. https://doi.org/10.1523/JNEUROSCI.2237-08.2008.

786 Kirik, Deniz, Carl Rosenblad, and Anders Björklund. 1998. “Characterization of Behavioral and
787 Neurodegenerative Changes Following Partial Lesions of the Nigrostriatal Dopamine System
788 Induced by Intrastriatal 6-Hydroxydopamine in the Rat.” *Experimental Neurology* 152 (2): 259–
789 77. https://doi.org/10.1006/exnr.1998.6848.

790 Kravitz, Alexxai V., Benjamin S. Freeze, Philip R.L. Parker, Kenneth Kay, Myo T. Thwin, Karl Deisseroth,
791 and Anatol C. Kreitzer. 2010. “Regulation of Parkinsonian Motor Behaviours by Optogenetic
792 Control of Basal Ganglia Circuitry.” *Nature* 466 (7306): 622–26.
793 https://doi.org/10.1038/nature09159.

794 Liss, Birgit, Oliver Franz, Sabine Sewing, Ralf Bruns, Henrike Neuhoff, and Jochen Roeper. 2001.
795 “Tuning Pacemaker Frequency of Individual Dopaminergic Neurons by Kv4.3L and KChip3.1
796 Transcription.” *EMBO Journal* 20 (20): 5715–24. https://doi.org/10.1093/emboj/20.20.5715.

797 Liss, Birgit, and Jorg Striessnig. 2019. “The Potential of L-Type Calcium Channels as a Drug Target for
798 Neuroprotective Therapy in Parkinson’s Disease.” *Annual Review of Pharmacology and*
799 *Toxicology* 59: 263–89. https://doi.org/10.1146/annurev-pharmtox-010818-021214.

800 Milosevic, Luka, Suneil K. Kalia, Mojgan Hodaie, Andres M. Lozano, Alfonso Fasano, Milos R. Popovic,
801 and William D. Hutchison. 2018. “Neuronal Inhibition and Synaptic Plasticity of Basal Ganglia
802 Neurons in Parkinson’s Disease.” *Brain* 141 (1): 177–90. https://doi.org/10.1093/brain/awx296.

803 Ortner, Nadine J. 2021. “Voltage-Gated Ca2+ Channels in Dopaminergic Substantia Nigra Neurons:
804 Therapeutic Targets for Neuroprotection in Parkinson’s Disease?” *Frontiers in Synaptic*
805 *Neuroscience* 13 (February): 1–11. https://doi.org/10.3389/fnsyn.2021.636103.

806 Ortner, Nadine J., Gabriella Bock, Antonios Dougalis, Maria Kharitonova, Johanna Duda, Simon Hess,
807 Petronel Tuluc, et al. 2017. “Lower Affinity of Isradipine for L-Type Ca2+ Channels during
808 Substantia Nigra Dopamine Neuron-like Activity: Implications for Neuroprotection in Parkinson’s
809 Disease.” *Journal of Neuroscience* 37 (28): 6761–77. https://doi.org/10.1523/JNEUROSCI.2946-
810 16.2017.

811 Otomo, Kanako, Jessica Perkins, Anand Kulkarni, Strahinja Stojanovic, Jochen Roeper, and Carlos A.
812 Paladini. 2020. “In Vivo Patch-Clamp Recordings Reveal Distinct Subthreshold Signatures and
813 Threshold Dynamics of Midbrain Dopamine Neurons.” *Nature Communications* 11 (1): 1–15.
814 https://doi.org/10.1038/s41467-020-20041-2.

815 Parker, Jones G., Jesse D. Marshall, Biafra Ahanonu, Yu Wei Wu, Tony Hyun Kim, Benjamin F. Grewe,
816 Yanping Zhang, et al. 2018. *Diametric Neural Ensemble Dynamics in Parkinsonian and Dyskinetic*

States. *Nature*. Vol. 557. https://doi.org/10.1038/s41586-018-0090-6.

Parker, Philip R.L., Arnaud L. Lalive, and Anatol C. Kreitzer. 2016. "Pathway-Specific Remodeling of Thalamostriatal Synapses in Parkinsonian Mice." *Neuron* 89 (4): 734–40. https://doi.org/10.1016/j.neuron.2015.12.038.

Phillips, Ryan S., Ian Rosner, Aryn H. Gittis, and Jonathan E. Rubin. 2020. "The Effects of Chloride Dynamics on Substantia Nigra Pars Reticulata Responses to Pallidal and Striatal Inputs." *ELife* 9: 1–35. https://doi.org/10.7554/ELIFE.55592.

Pinault, Didier. 1996. "A Novel Single-Cell Staining Procedure Performed in Vivo under Electrophysiological Control: Morpho-Functional Features of Juxtacellularly Labeled Thalamic Cells and Other Central Neurons with Biocytin or Neurobiotin." *Journal of Neuroscience Methods* 65 (2): 113–36. https://doi.org/10.1016/0165-0270(95)00144-1.

Poulin, Jean Francois, Giuliana Caronia, Caitlyn Hofer, Qiaoling Cui, Brandon Helm, Charu Ramakrishnan, C. Savio Chan, Daniel A. Dombeck, Karl Deisseroth, and Rajeshwar Awatramani. 2018. "Mapping Projections of Molecularly Defined Dopamine Neuron Subtypes Using Intersectional Genetic Approaches." *Nature Neuroscience* 21 (9): 1260–71. https://doi.org/10.1038/s41593-018-0203-4.

Rubi, Lena, and Jean Marc Fritschy. 2020. "Increased GABAergic Transmission in Neuropeptide Y-Expressing Neurons in the Dopamine-Depleted Murine Striatum." *Journal of Neurophysiology* 123 (4): 1496–1503. https://doi.org/10.1152/jn.00059.2020.

Saunders, Arpiar, Evan Z. Macosko, Alec Wysoker, Melissa Goldman, Fenna M. Krienen, Heather de Rivera, Elizabeth Bien, et al. 2018. "Molecular Diversity and Specializations among the Cells of the Adult Mouse Brain." *Cell* 174 (4): 1015-1030.e16. https://doi.org/10.1016/j.cell.2018.07.028.

Schiemann, Julia, Falk Schlaudraff, Verena Klose, Markus Bingmer, Susumu Seino, Peter J. Magill, Kareem A. Zaghloul, Gaby Schneider, Birgit Liss, and Jochen Roeper. 2012. "K-ATP Channels in Dopamine Substantia Nigra Neurons Control Bursting and Novelty-Induced Exploration." *Nature Neuroscience* 15 (9): 1272–80. https://doi.org/10.1038/nn.3185.

Schwarting, R. K.W., and J. P. Huston. 1996. "Unilateral 6-Hydroxydopamine Lesions of Meso-Striatal Dopamine Neurons and Their Physiological Sequelae." *Progress in Neurobiology* 49 (3): 215–66. https://doi.org/10.1016/S0301-0082(96)00015-9.

Sitzia, Giacomo, Ioannis Mantas, Xiaoqun Zhang, Per Svenningsson, and Karima Chergui. 2020. "NMDA Receptors Are Altered in the Substantia Nigra Pars Reticulata and Their Blockade Ameliorates Motor Deficits in Experimental Parkinsonism." *Neuropharmacology* 174 (May): 108136. https://doi.org/10.1016/j.neuropharm.2020.108136.

Subramaniam, Mahalakshmi, Daniel Althof, Suzana Gispert, Jochen Schwenk, Georg Auburger, Akos Kulik, Bernd Fakler, and Jochen Roeper. 2014. "Mutant α-Synuclein Enhances Firing Frequencies in Dopamine Substantia Nigra Neurons by Oxidative Impairment of A-Type Potassium Channels." *Journal of Neuroscience* 34 (41): 13586–99. https://doi.org/10.1523/JNEUROSCI.5069-13.2014.

Subramaniam, Mahalakshmi, Beatrice Kern, Simone Vogel, Verena Klose, Gaby Schneider, and Jochen Roeper. 2014. "Selective Increase of in Vivo Firing Frequencies in DA SN Neurons after Proteasome Inhibition in the Ventral Midbrain." *European Journal of Neuroscience* 40 (6): 2898–2909. https://doi.org/10.1111/ejn.12660.

Surmeier, D. James. 2007. "Calcium, Ageing, and Neuronal Vulnerability in Parkinson's Disease." *Lancet Neurology* 6 (10): 933–38. https://doi.org/10.1016/S1474-4422(07)70246-6.

Surmeier, D. James, Glenda M. Halliday, and Tanya Simuni. 2017. “Calcium, Mitochondrial Dysfunction and Slowing the Progression of Parkinson’s Disease.” *Experimental Neurology* 298: 202–9. https://doi.org/10.1016/j.expneurol.2017.08.001.

Surmeier, D. James, José A. Obeso, and Glenda M. Halliday. 2017. “Selective Neuronal Vulnerability in Parkinson Disease.” *Nature Reviews Neuroscience* 18 (2): 101–13. https://doi.org/10.1038/nrn.2016.178.

Tarfa, Rahilla A., Rebekah C. Evans, and Zayd M. Khaliq. 2017. “Enhanced Sensitivity to Hyperpolarizing Inhibition in Mesoaccumbal Relative to Nigrostriatal Dopamine Neuron Subpopulations.” *Journal of Neuroscience* 37 (12): 3311–30. https://doi.org/10.1523/JNEUROSCI.2969-16.2017.

Thakur, Poonam, Ludivine S. Breger, Martin Lundblad, Oi Wan Wan, Bengt Mattsson, Kelvin C. Luk, Virginia M.Y. Lee, John Q. Trojanowski, and Anders Björklund. 2017. “Modeling Parkinson’s Disease Pathology by Combination of Fibril Seeds and α-Synuclein Overexpression in the Rat Brain.” *Proceedings of the National Academy of Sciences of the United States of America* 114 (39): E8284–93. https://doi.org/10.1073/pnas.1710442114.

The Parkinson Study Group STEADY-PD. 2020. “Isradipine Versus Placebo in Early Parkinson Disease A Randomized Trial The.” *Ann Intern Med* 63 (8): 1–18. https://doi.org/10.7326/M19-2534.Isradipine.

Tinkhauser, Gerd, Flavie Torrecillos, Alek Pogosyan, Abteen Mostofi, Manuel Bange, Petra Fischer, Huiling Tan, et al. 2020. “The Cumulative Effect of Transient Synchrony States on Motor Performance in Parkinson⇔s Disease.” *Journal of Neuroscience* 40 (7): 1571–80. https://doi.org/10.1523/JNEUROSCI.1975-19.2019.

Turrigiano, Gina. 2012. “Homeostatic Synaptic Plasticity: Local and Global Mechanisms for Stabilizing Neuronal Function.” *Cold Spring Harbor Perspectives in Biology* 4 (1): 1–18. https://doi.org/10.1101/cshperspect.a005736.

Ungerstedt, Urban. 1968. “6-Hydroxy-Dopamine Induced Degeneration of Central Monoamine Neurons.” *European Journal of Pharmacology* 5 (1): 107–10. https://doi.org/10.1016/0014-2999(68)90164-7.

Ungless, Mark A., and Anthony A. Grace. 2012. “Are You or Aren’t You? Challenges Associated with Physiologically Identifying Dopamine Neurons.” *Trends in Neurosciences* 35 (7): 422–30. https://doi.org/10.1016/j.tins.2012.02.003.

West, Mark J. 1993. “New Stereological Methods for Counting Neurons.” *Neurobiology of Aging* 14 (4): 275–85. https://doi.org/10.1016/0197-4580(93)90112-O.

Wichmann, Thomas, Hagai Bergman, and Mahlon R. DeLong. 2018. “Basal Ganglia, Movement Disorders and Deep Brain Stimulation: Advances Made through Non-Human Primate Research.” *Journal of Neural Transmission* 125 (3): 419–30. https://doi.org/10.1007/s00702-017-1736-5.

Winkler, Christian, Deniz Kirik, Anders Björklund, and M. Angela Cenci. 2002. “L-DOPA-Induced Dyskinesia in the Intrastriatal 6-Hydroxydopamine Model of Parkinson’s Disease: Relation to Motor and Cellular Parameters of Nigrostriatal Function.” *Neurobiology of Disease* 10 (2): 165–86. https://doi.org/10.1006/nbdi.2002.0499.

Zhang, W., B.R. Xiong, L.Q. Zhang, X. Huang, X. Yuan, Y.K. Tian, and X.B. Tian. 2021. “The Role of the GABAergic System in Diseases of the Central Nervous System.” *Neuroscience*.

Zweifel, Larry S., Jones G. Parker, Collin J. Lobb, Aundrea Rainwater, Valeriez Wall, Jonathan P. Fadok, Martin Darvas, et al. 2009. “Disruption of NMDAR-Dependent Burst Firing by Dopamine Neurons

Provides Selective Assessment of Phasic Dopamine-Dependent Behavior." *Proceedings of the National Academy of Sciences of the United States of America* 106 (18): 7281–88. https://doi.org/10.1073/pnas.0813415106.

908 Figures
909

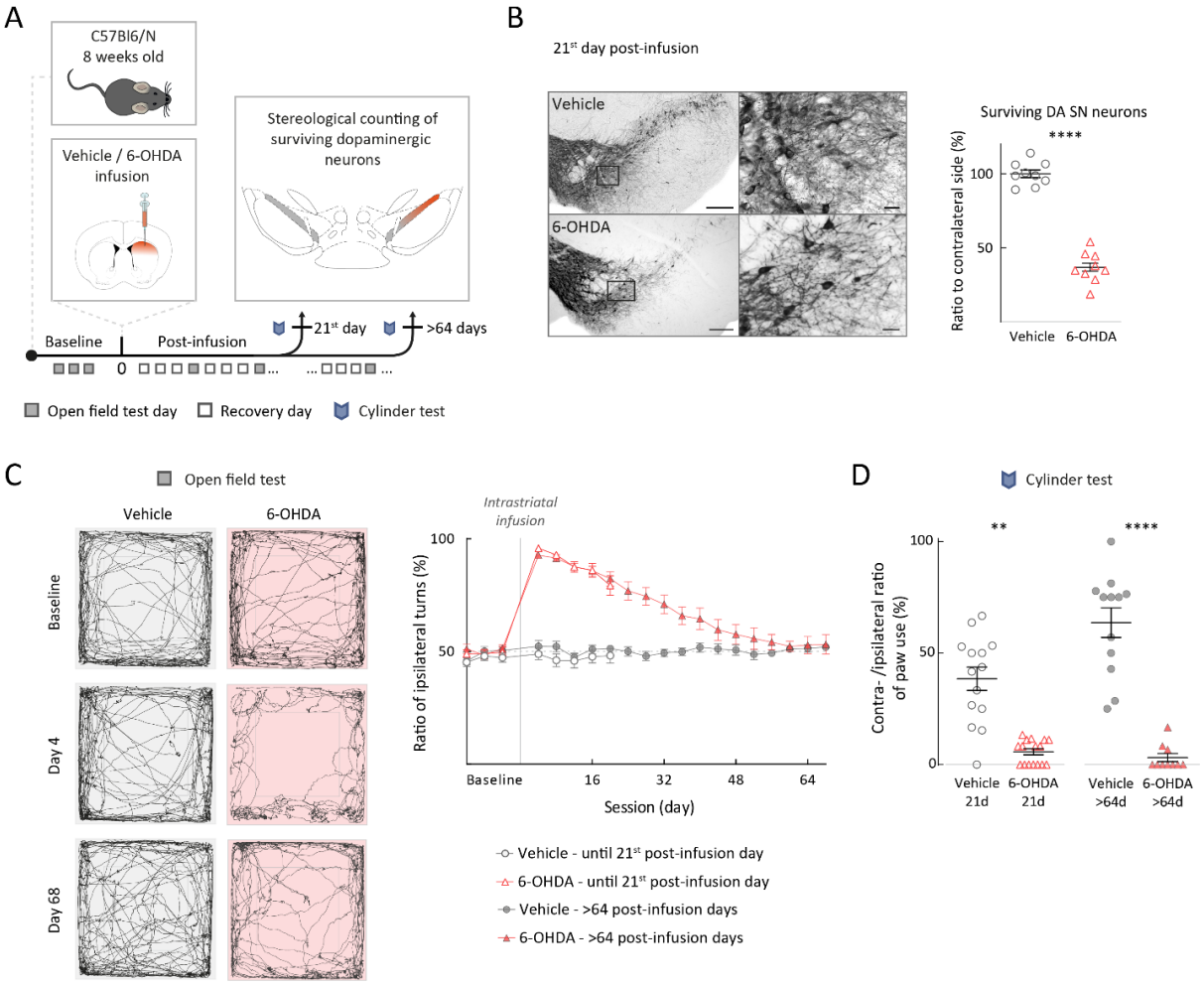

910

911

912 **Figure 1. Unilateral striatal 6-OHDA mouse model with stable loss of SN DA neurons resulted in delayed partial**
913 **behavioral recovery.**

914 (A) Experimental design, illustrating timeline of behavioral assays with termination points – groups ended either
915 on the 21st, or later than the 64th post-infusion day. (B) Left panel: TH-DAB staining of the SN, 10x magnification
916 and 60x magnification for vehicle and 6-OHDA-infused mouse. Scalebar left 200µm, scalebar right 25µm. Right
917 panel: ratio of ipsilateral (infusion side) to contralateral side of surviving TH-positive neurons in SN at 21st post-
918 infusion day. (C) Left: spontaneous locomotion of mice in open field arena for a 10 min session. Left, examples
919 of an ACSF-infused mouse (vehicle), right example of a 6-OHDA-infused mouse at baseline (upper panels), 4th
920 post-infusion day (middle panels) and 68th post-infusion day (lower panels). Right: ratio of ipsilateral to
921 contralateral turning behavior for all experimental groups plotted against session days. Note recovery in the 6-
922 OHDA-treated mice from day 4 to day 68 after initial strong turning bias (>90%). (D) Cylinder test quantified by
923 ratio of contra- to ipsilateral forepaw use. Note significant loss of contralateral forepaw involvement, both at 21
924 and 64 days. All data are presented as mean ± standard error of mean (SEM).

925

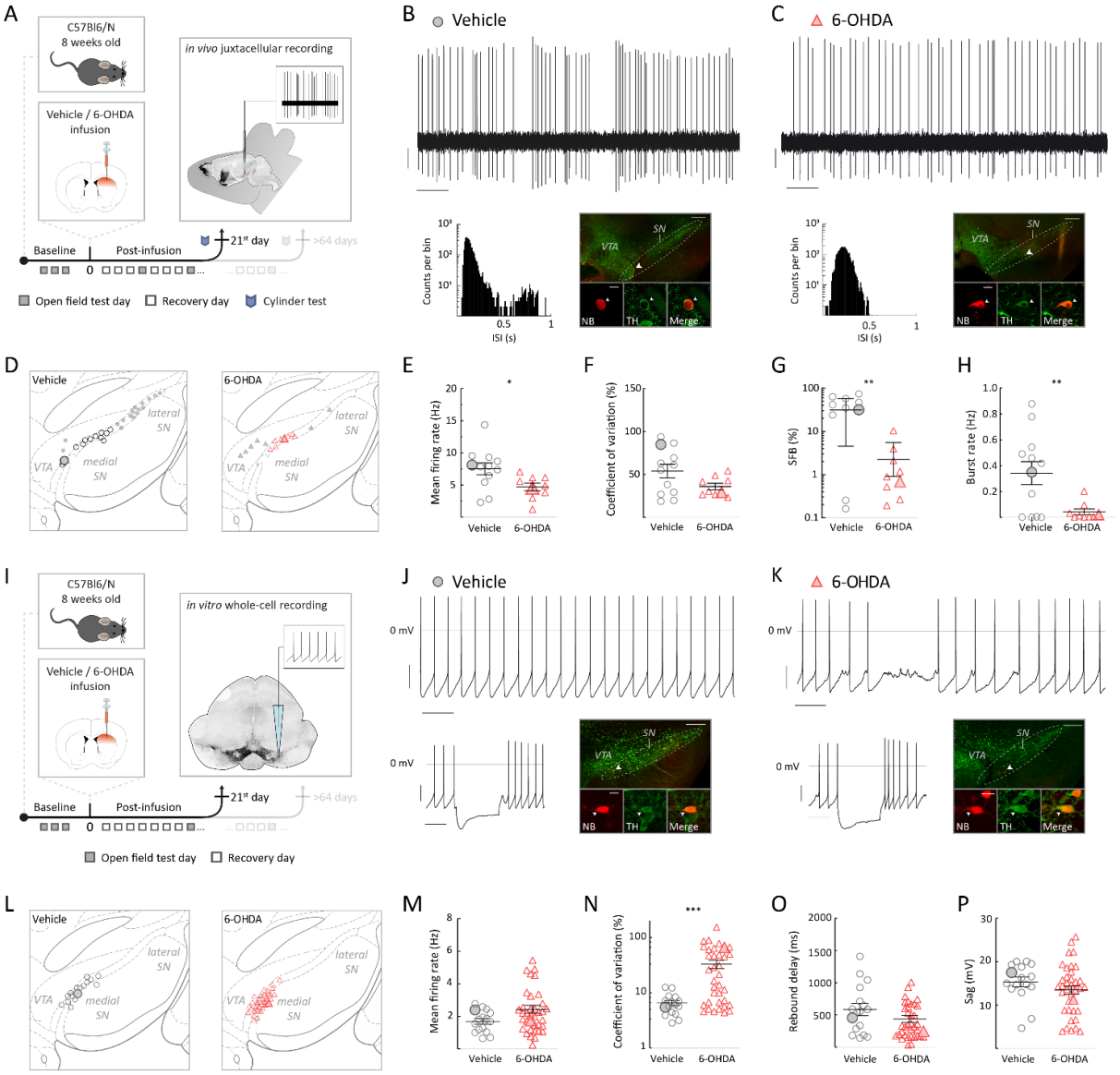

Figure 2. Surviving SN DA neurons at early post-6-OHDA phase exhibited a compressed dynamic range with a 10-fold decrease in *in vivo* bursting and a 5-fold decree in *in vitro* pacemaker regularity

(A), (I) Experimental design, illustrating timeline of behavioral assays, followed by terminal *in vivo* juxtacellular recordings (A) or by terminal *in vitro* whole-cell recordings (I) at the 21st post-infusion day. (B), (C) Top: 10s original recording trace of spontaneous *in vivo* single-unit activity from SN DA neurons in vehicle (B) and 6-OHDA-infused mouse (C). Scalebars: 1s, 0.2mV. Below, left: corresponding ISI histograms. Below, right: corresponding confocal images of juxtacellularly labelled and immunohistochemically identified DA neuron. Note the sparse bursting of the surviving SN DA neuron from the 6-OHDA-infused mouse at early phase. (D), (L) Anatomical mapping of all extracellularly recorded and juxtacellularly labelled DA neurons (D), and of all in vitro recorded and filled DA neurons (L), projected to bregma -3.08 mm. Location of example SN DA neurons in (B), (C), (J), (K) are highlighted. Smaller symbols represent DA neurons that have been recorded and identified, but not included in the group data analysis in (E-H). (E-H) Scatter dot-plots, showing significant decrease of *in vivo* mean firing rate (E), percentage of SFB (G) and burst rate (H) and no significant differences in CV (F) between the vehicle and 6-OHDA-infused mice. Note the 10-fold decrease in SFB for 6-OHDA-infused mice. (J), (K) Top: 10s original recording trace of *in vitro* whole-cell recording of spontaneous SN DA neuron activity in a vehicle (J) and 6-OHDA-infused (K) mouse. Scalebars: 1s, 20mV. Note that the 6-OHDA DA neuron has a highly irregular pacemaking. Below, left: corresponding to hyperpolarizing current injection. Below, right: confocal images of NB filled and immunohistochemically identified DA neuron. (M-P) Scatter dot-plots, showing no difference in *in vitro* mean firing rate (M), rebound delay (O) or sag-component (P) and a 5-fold increase in CV (N). Immunohistochemical imaging for all four DA neurons are displayed in 10x and 60x magnifications (green, TH; red, NB), scalebars: 200µm, 20µm. All data are presented as mean ± standard error of mean (SEM).

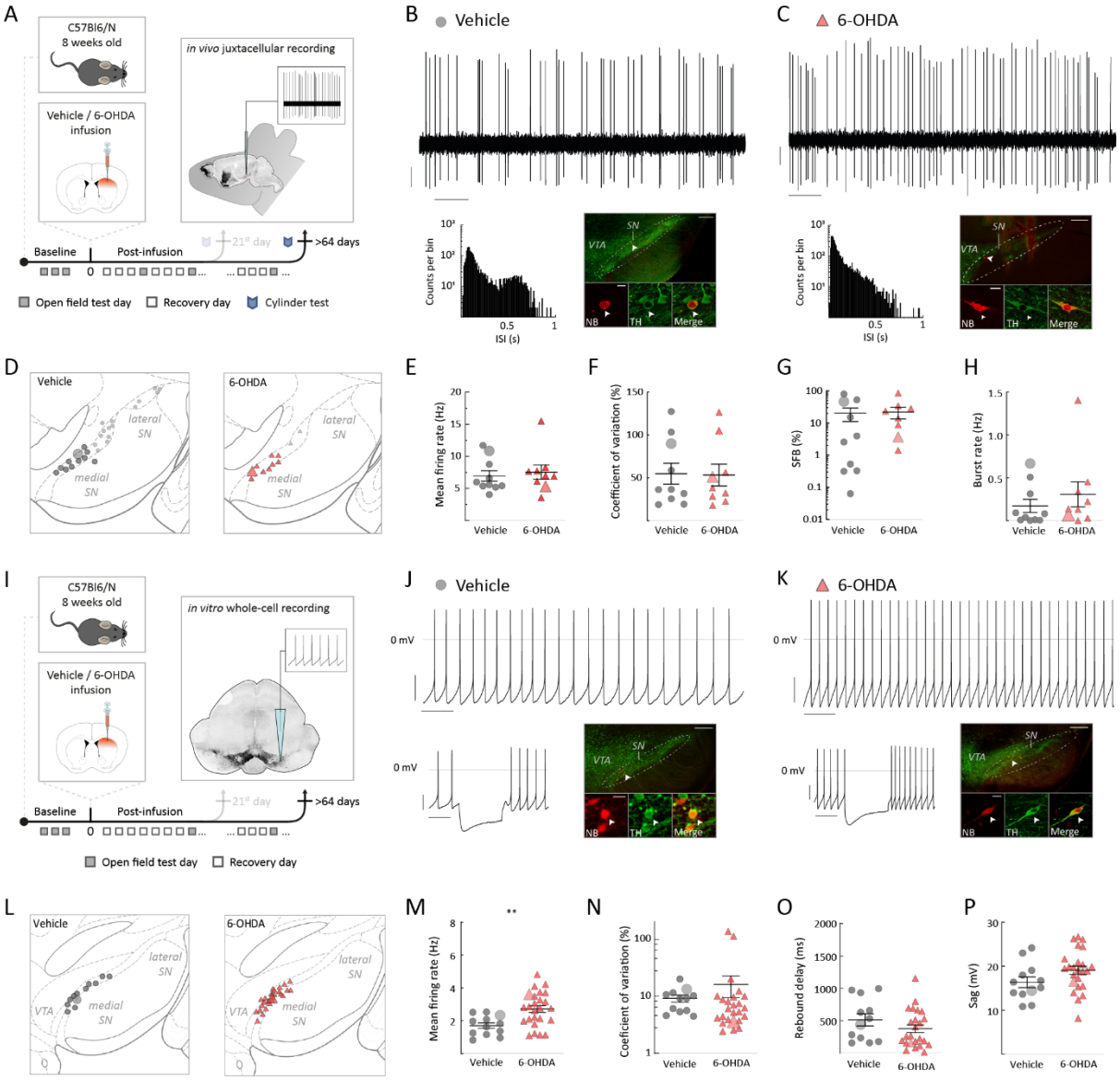

Figure 3. Surviving SN DA neurons at late 6-OHDA phase recovered *in vivo* burst firing and doubled their intrinsic pacemaker frequency *in vitro*.

(A), (I) Experimental design, illustrating timeline of behavioral assays, followed by terminal *in vivo* juxtacellular recordings (A) or by terminal *in vitro* whole-cell recordings (I) after >64 post-infusion days. (B), (C) Top: 10s original recording trace of spontaneous *in vivo* single-unit activity from SN DA neurons in vehicle (B) and 6-OHDA-infused mouse (C). Scalebars: 1s, 0.2mV. Below, left: corresponding ISI histograms. Below, right: corresponding confocal images of juxtacellularly labelled and immunohistochemically identified DA neuron. (D), (L) Anatomical mapping of all extracellularly recorded and juxtacellularly labelled DA neurons (D), and of all *in vitro* recorded and filled DA neurons (L), projected to bregma -3.40 mm (D) and -3.08mm (L). Location of example SN DA neurons in (B), (C), (J), (K) are highlighted. Smaller symbols represent DA neurons that have been recorded and identified, but not included in the group data analysis in (E-H). (E-H) Scatter dot-plots, showing no significant difference in mean firing rate (E), CV (F), SFB (G) and burst rate (H). (J), (K) Top: 10s original recording trace of *in vitro* whole-cell recording of spontaneous activity from SN DA neurons in a vehicle (J) and 6-OHDA-infused (K) mouse. Scalebars: 1s, 20mV. Note that the 6-OHDA DA neuron has enhanced, but regular pacemaking. Below, left, corresponding to hyperpolarizing current injection. Below, right, confocal images of NB filled and immunohistochemically identified DA neuron. (M-P) Scatter dot-plots, showing doubling of the firing rate (M), no difference in CV (N), decrease in rebound delay (O) and increase of sag-component (P) for the 6-OHDA-treated mice in comparison to vehicle group. Immunohistochemical imaging for all four DA neurons are displayed in 10x and 60x magnifications (green, TH; red, NB), scalebars: 200µm, 20µm. All data are presented as mean ± standard error of mean (SEM).

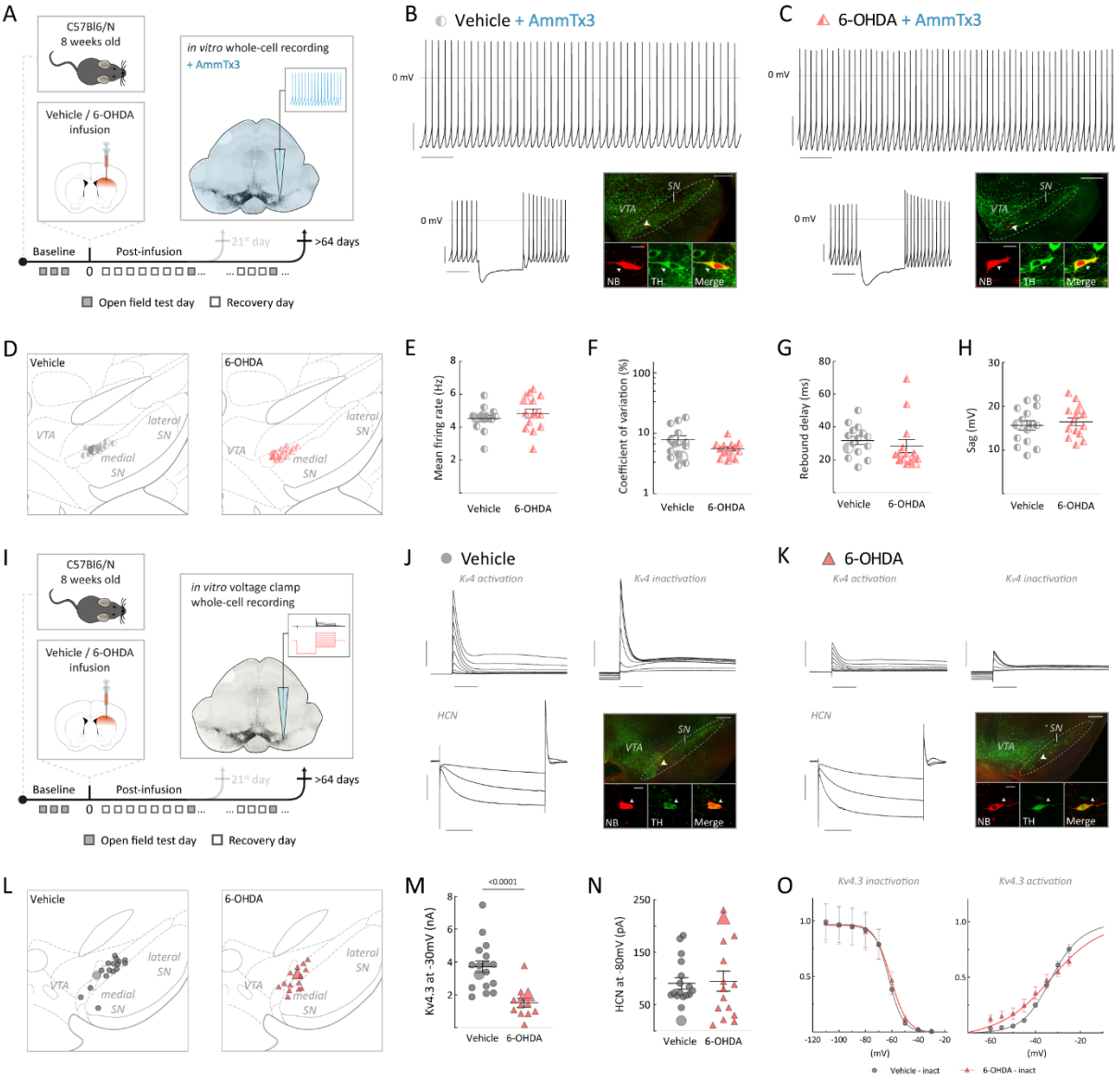

Figure 4. Enhanced pacemaker frequency of SN DA neurons at the late post-6-OHDA phase was mediated by K_v4.3 channel downregulation

(A), (I) Experimental design, illustrating timeline of behavioral assays, followed by terminal *in vitro* whole-cell recordings under K_v4.3 channel blocker AmmTx3 (A) or *in vitro* voltage-clamp whole-cell recordings (I) after >64 post-infusion days. (B), (C) Top: 10s original recording traces of *in vitro* whole-cell recording of spontaneous activity from DA SN neurons in AmmTx3-preincubated slices for a vehicle (B) and 6-OHDA-infused (C) mouse. Below, left: corresponding hyperpolarizing current injection. Scalebars: 1s, 20mV. Below, right: confocal images of NB filled and immunohistochemically identified DA neuron. (D), (L) Anatomical mapping of all in vitro recorded and filled DA neurons, projected to bregma -2.92 mm (D) and -3.16mm (L). (E-H) Scatter dot-plots, showing no differences in mean firing rate (E), coefficient of variation (F), rebound delay duration (G) and sag amplitude (H). (J), (K) Original recording trace of in vitro voltage-clamp recordings from DA SN neurons in a vehicle (J) and 6-OHDA-infused (K) mouse. Top, right: Zoom in from a K_v4.3 channel activation. Top, left: Zoom in from a K_v4.3 channel inactivation. Below, right: Zoom in from HCN-channel activation. Below, right, confocal images of NB filled and immunohistochemically identified DA neuron. Scalebars first row: 3nA, 100ms. Scalebars below, left: 5nA, 500ms. Note the small K_v4.3 channel in/activation peak in a surviving DA neuron from a 6-OHDA mouse in comparison the one from an ACSF treated mouse. Immunohistochemical imaging for all four DA neurons are displayed in 10x and 60x magnifications (green, TH; red, NB), scalebars: 200µm, 20µm. All data are presented as mean ± standard error of mean (SEM). (M) Scatter dot-plots, showing a significant, half of maximum K_v4.3 channel conductance in surviving DA neurons. (N) Scatter dot-plots, showing no difference in HCN channel delta current (I_{peak} - I_{steady}) between groups. (O) Normalized K_v4.3 current (I_{peak} - I_{steady}) at different voltage steps,

resulting in inactivation and activation curve for both groups. All data are presented as mean ± standard error of mean (SEM).

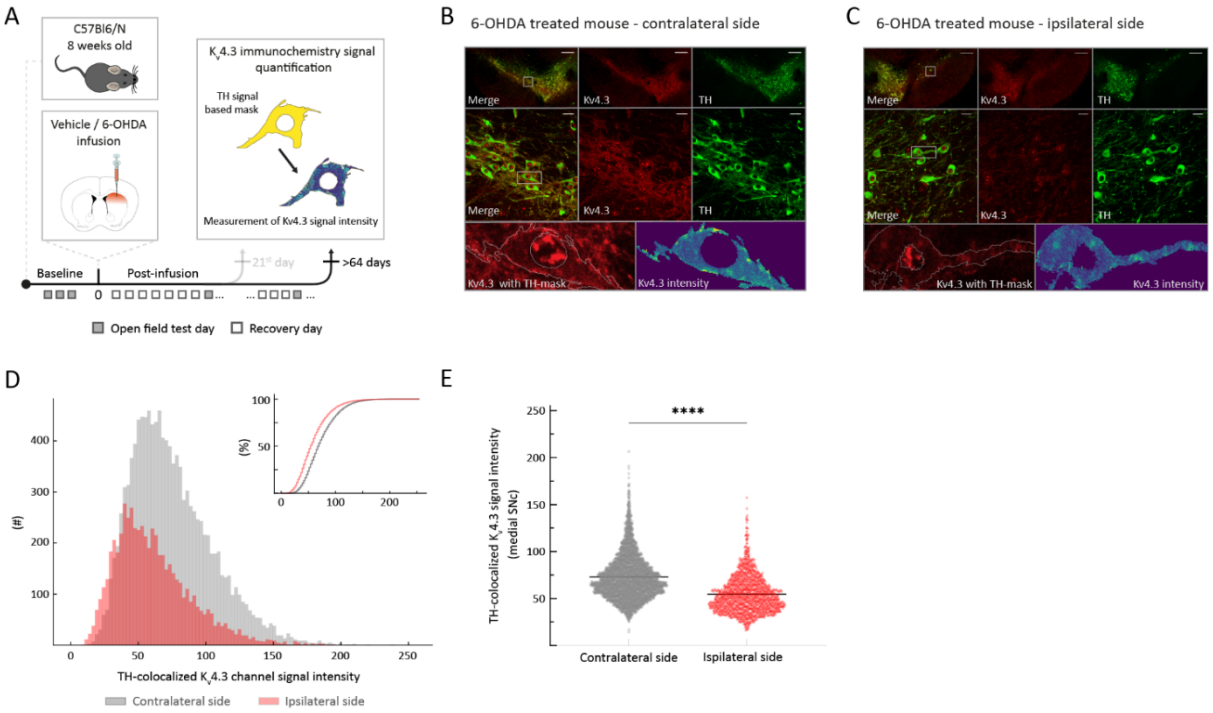

Figure 5. Surviving DA SN neurons at the late post-6-OHDA phase showed lower K_v4.3 channel immunohistochemical signal

(A) Experimental design, illustrating timeline of behavioral assays, followed by multi-labeling immunohistochemistry for exploring K_v4.3-channel expression differences after >64 post-infusion days. (B), (C) Top: 4x magnification of midbrain of a 6-OHDA-infused mouse, >64 days post-lesion – contralateral side (B), and corresponding ipsilateral side (C). Middle: 60x magnification in the highlighted area from 4x image (green, TH; red, K_v4.3). Bottom, left: zoom-in on an example ROI (highlighted in 60x image). Bottom, right: color-coded Kv4.3-channel immunohistochemical signal intensity in the example ROI. Note K_v4.3-channel signal decrease in surviving DA neurons on the ipsilateral to the injection side. (D) Histogram showing intensity of K_v4.3 immunosignals for all TH-positive ROIs, from ipsilateral, lesioned, side (in red) and from contralateral side (in grey). Inset, same data shown as a cumulative distribution. Note a clear right-shift to lower intensities for the ipsilateral side. (E) Comparison of mean TH-colocalized K_v4.3 immunosignals from medial SN from ipsilateral, lesioned, side, and contralateral, as control side. All data are presented as mean ± standard error of mean (SEM).

1008

1009 ## Supplementary Figures
1010

1011 **Supplementary Figure 1.**

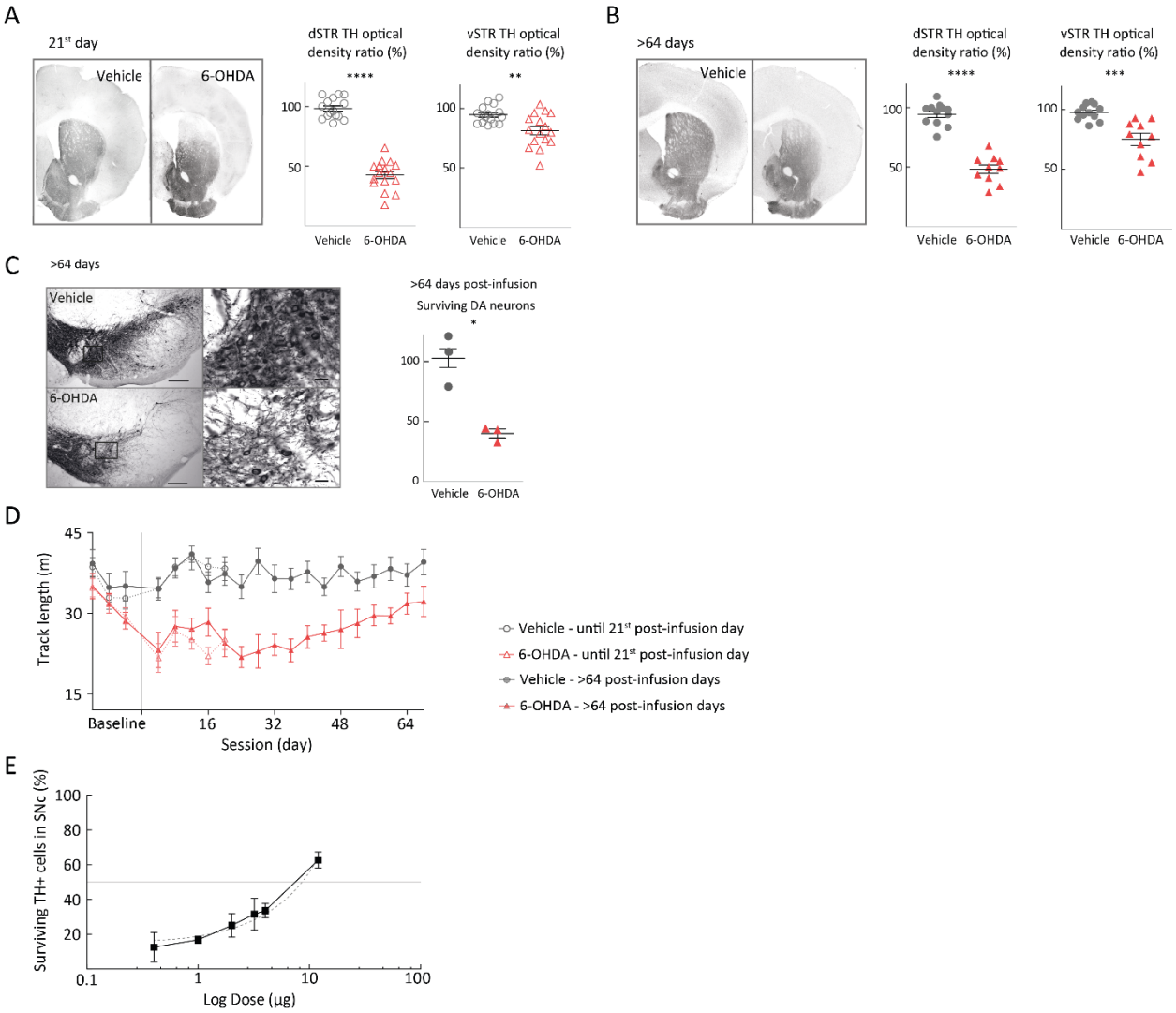

1012

1013 (A), (B) Comparison of ipsilateral, infusion side, to contralateral side as percentage of relative TH
1014 immunohistochemistry signal in the dorsal striatum (dSTR) and ventral striatum (vSTR), at the corresponding
1015 early (A) and late phase (B). Note the stability of TH density loss in the dorsal striatum through time. (C) Ratio of
1016 ipsilateral (infusion side) to contralateral side of surviving TH-positive neurons in SN in the late phase. (D) Mean
1017 track length from all mice for each open field session. Note the post-infusion drop in performed track in the 6-
1018 OHDA groups, which gradually recovers. (Infusion day marked as a thin gray line.) (E) Ratio of TH+ cell loss in SNc
1019 (ipsilateral (infusion side) to contralateral side) >21st post-infusion day from different infused 6-OHDA doses.

1020 **Supplementary Figure 2.**

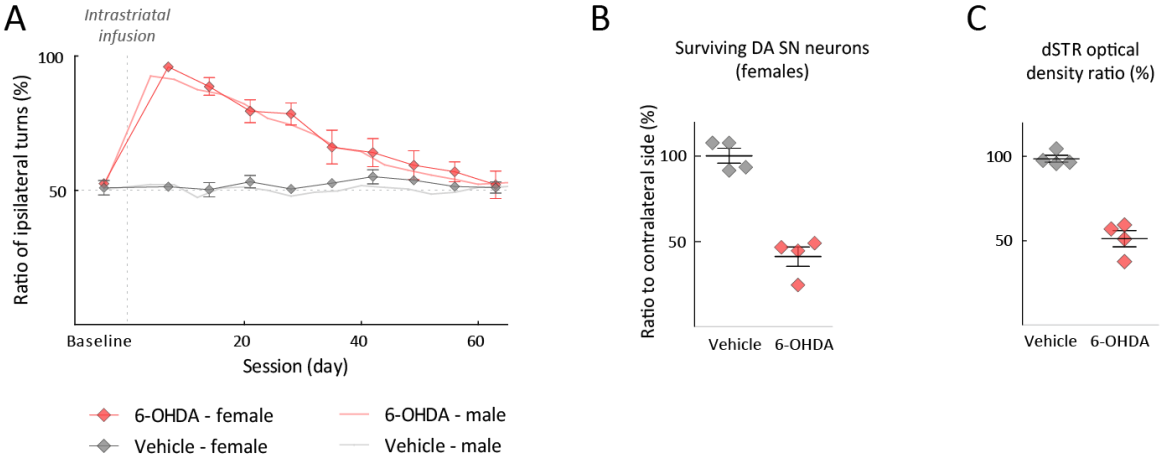

1021

1022 (A) Ratio of ipsilateral to contralateral turning behavior for female ACSF and 6-OHDA infused groups plotted
1023 against session days and with underlayed the corresponding ratio from the male ACSF and 6-OHDA groups as a
1024 mean-line. (B) Ratio of ipsilateral (infusion side) to contralateral side of surviving TH-positive neurons in SN at
1025 >64st post-infusion day from female ACSF and 6-OHDA infused mice. (C) Comparison of ipsilateral, infusion side,
1026 to contralateral side as percentage of relative TH immunohistochemistry signal in the dorsal striatum (dSTR) at
1027 >64st post-infusion day from female ACSF and 6-OHDA infused mice.

1028 **Supplementary Figure 3.**

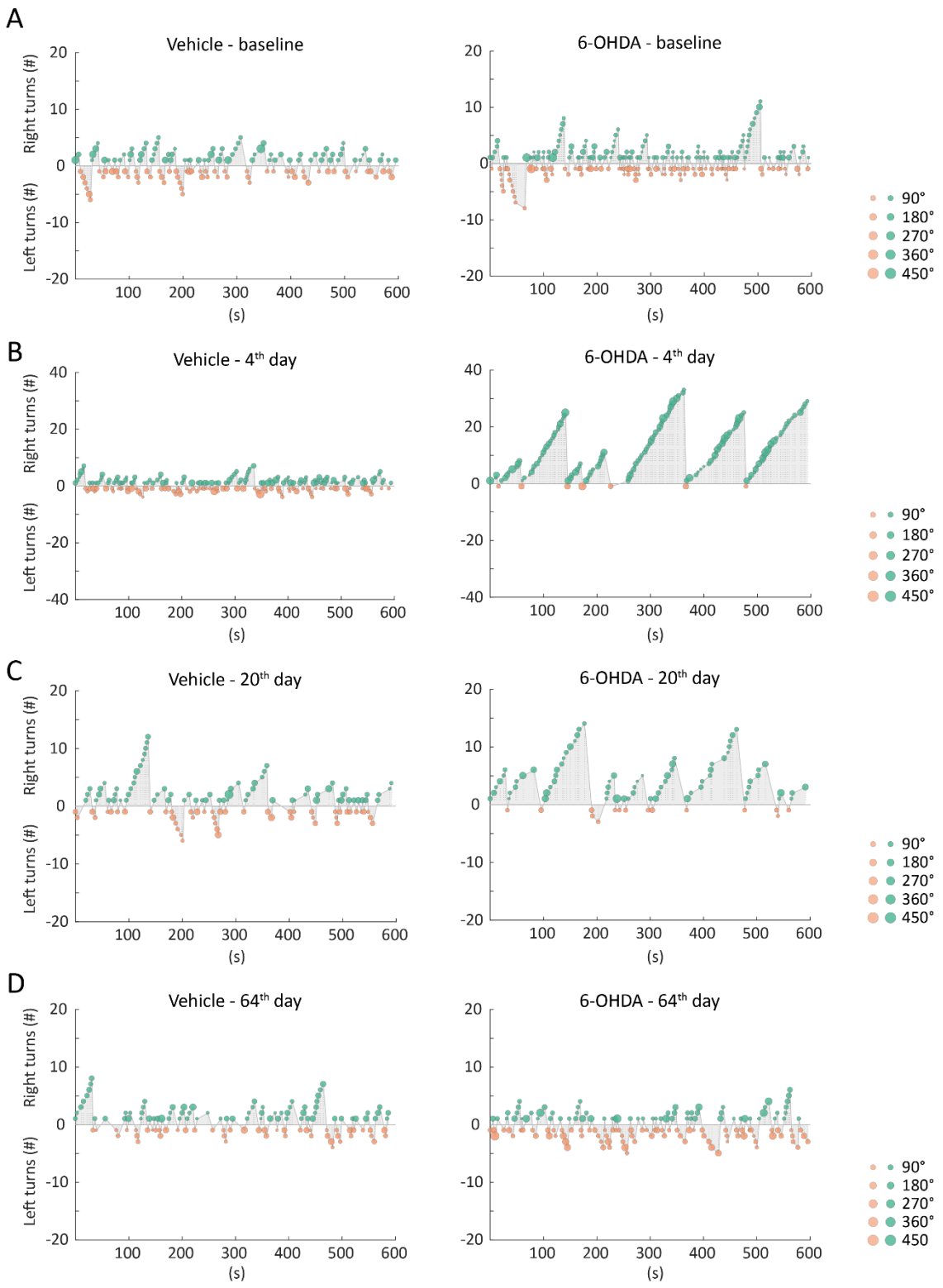

1029

1030 For two representative vehicle- and 6-OHDA-treated mice schematic representation of turning sequences. Left

1031 turn sequences are plotted as negative values, whereas right turn sequences are plotted as positive values. The

1032 count represents the number of same-direction turns within a sequence. On the left panels are turning

1033 sequences for the control animal and on the right panels for the 6-OHDA-infused animal, correspondingly in a

1034 baseline session (A), 4th post-operative day (B), 20th post-operative day (C) and 64th post-operative day (D).

1035

1036 **Supplementary Figure 4.**

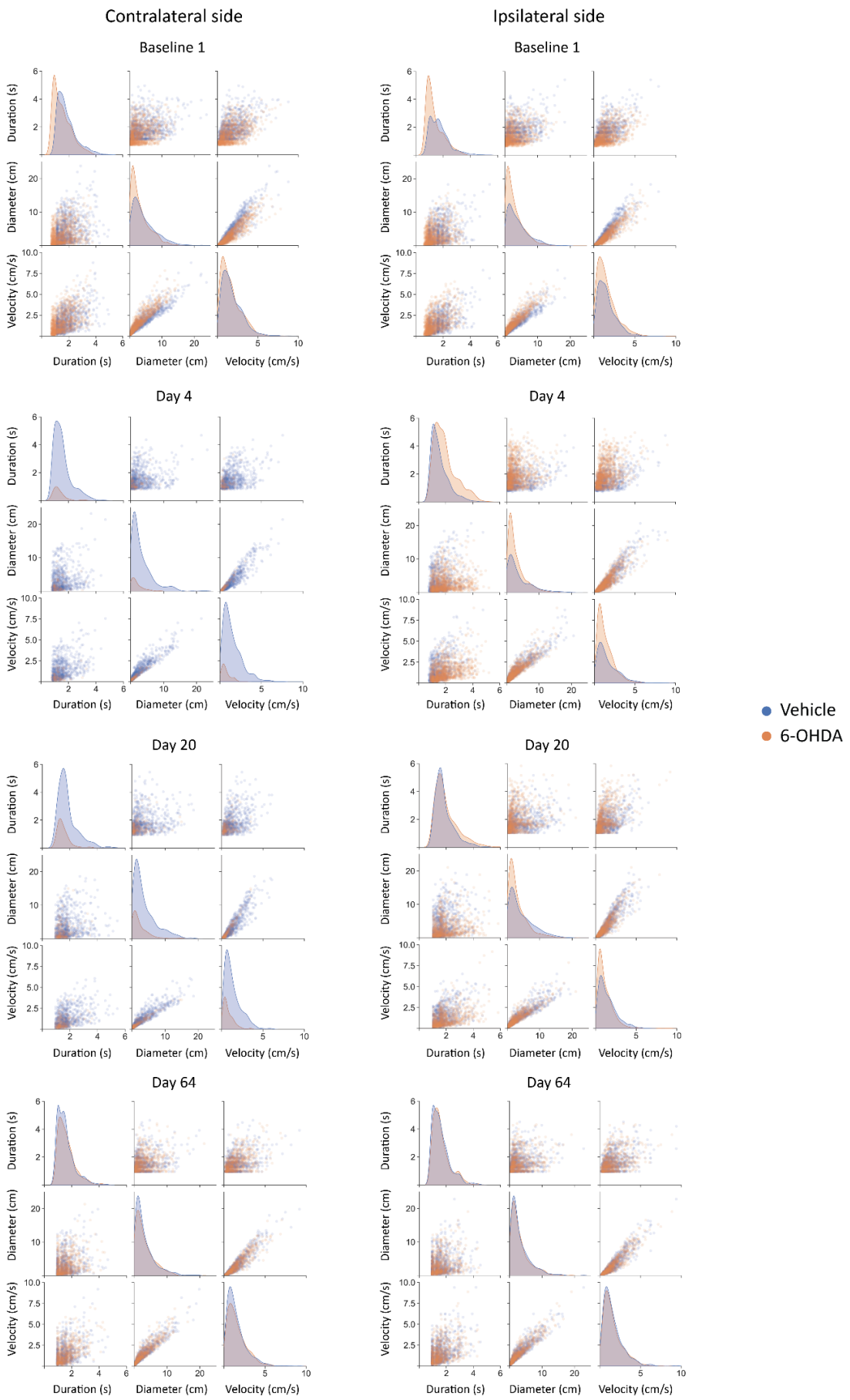

1037

1038 Correlation pair plots comparing turning features, such as velocity (cm/s), diameter (cm) and duration for all
1039 contralateral turns (left panels) and all ipsilateral turns performed from all vehicle-infused mice (in orange) and
1040 all 6-OHDA-treated mice (in blue) across different time points (baseline, 4th, 20th and 64th post-infusion day).

1041 **Supplementary Figure 5.**

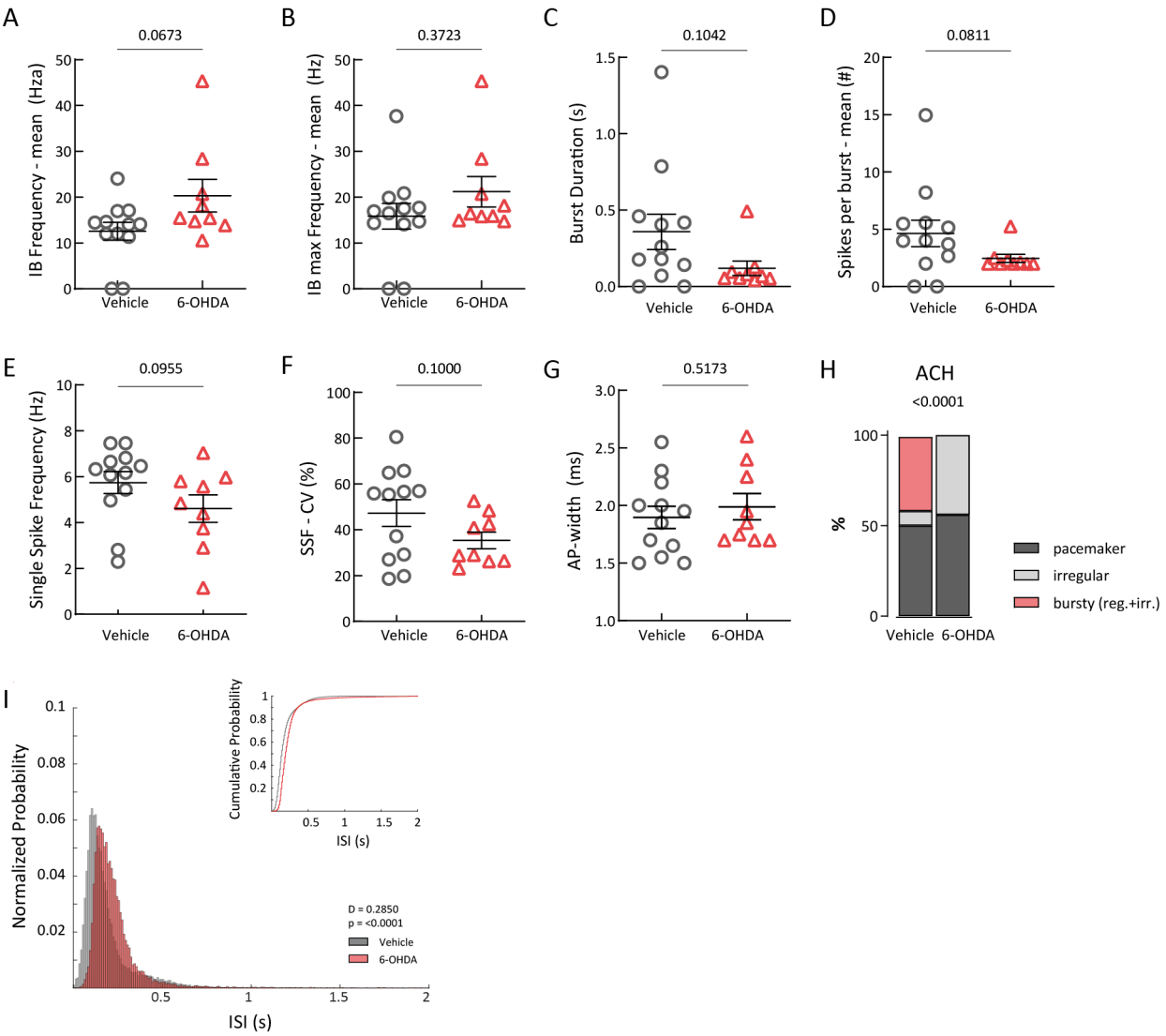

1042

1043 Scatter dot-plots, showing no significant difference of in vivo mean intra-burst (IB) frequency (A), mean
1044 maximum (max) intra-burst (IB) frequency (B), burst duration (C), number of spikes per burst (D), single spike
1045 frequency (SSF) (E), single spike coefficient of variance (CV) (F) and action potential (AP) width (G) (H) between
1046 the vehicle and 6-OHDA-infused mice in the early phase. (H) Normalized stacked bar plots of different in vivo
1047 firing patterns based on ACH. (I) ISI distributions from all in vivo recorded and labeled mSN DA neurons from
1048 vehicle- and 6-OHDA-treated mice in the early phase. Inset, cumulative representation of the same distributions.

1049

Supplementary Figure 6.

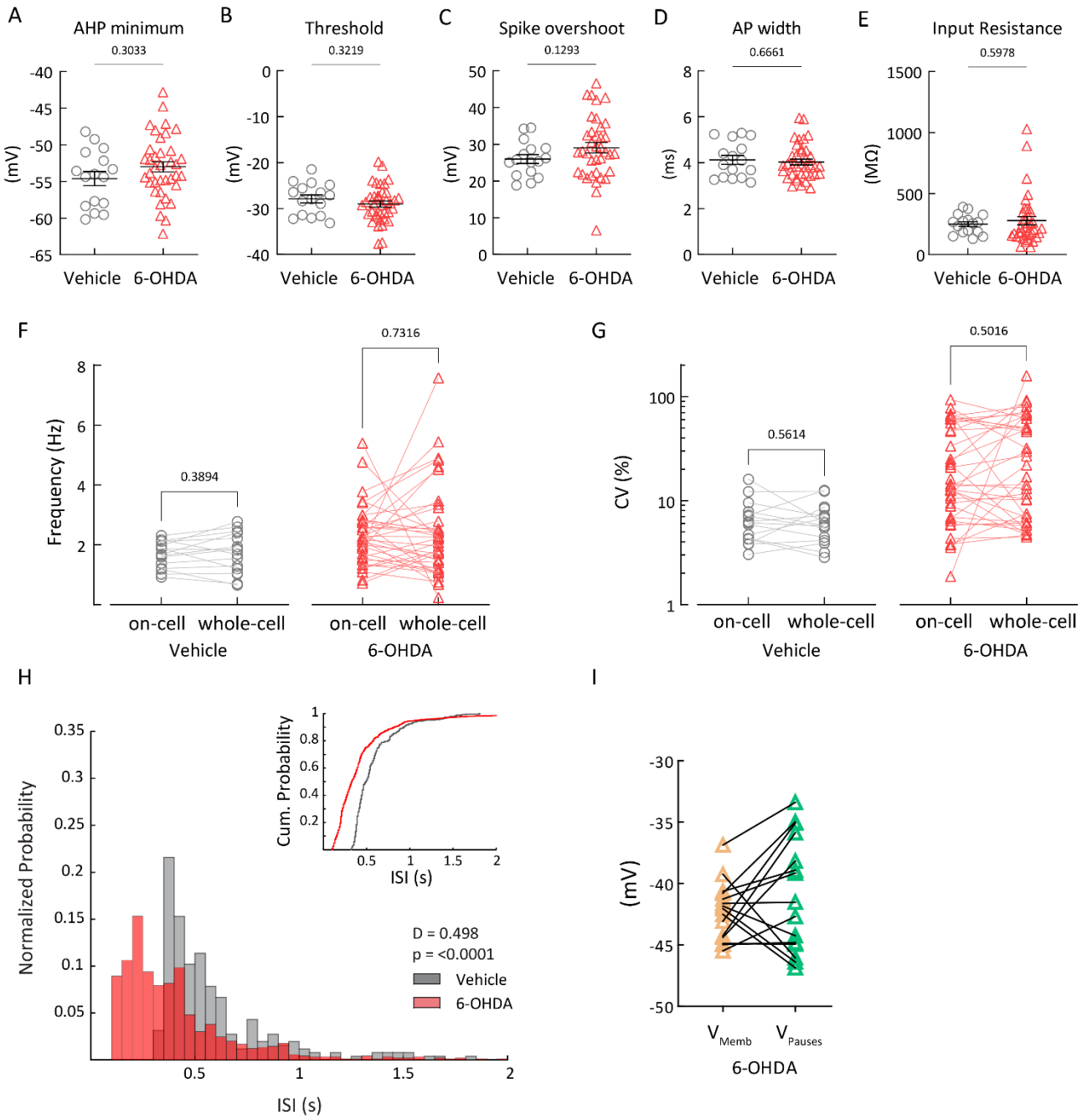

Scatter dot-plots, showing no significant difference of in vitro afterhyperpolarization (AHP) minimum (A), threshold (B), spike amplitude (C), action potential (AP) width (D) and input resistance (E) between the vehicle and 6-OHDA-infused mice in the early phase. (F), (G) Paired scatter dot-plots of firing frequency (F) and coefficient of variance (G) during on-cell recording and whole-cell recording in the early phase. (H) ISI distributions from all in vitro whole-cell recorded and labeled mSN DA neurons from vehicle- and 6-OHDA-treated mice in the early phase. Inset, cumulative representation of the same distributions. (I) Paired scatter dot-plot indicating no significant difference between the mean voltage during spike-pauses and the rest of the firing activity.

1060

1061

1062 **Supplementary Figure 7.**

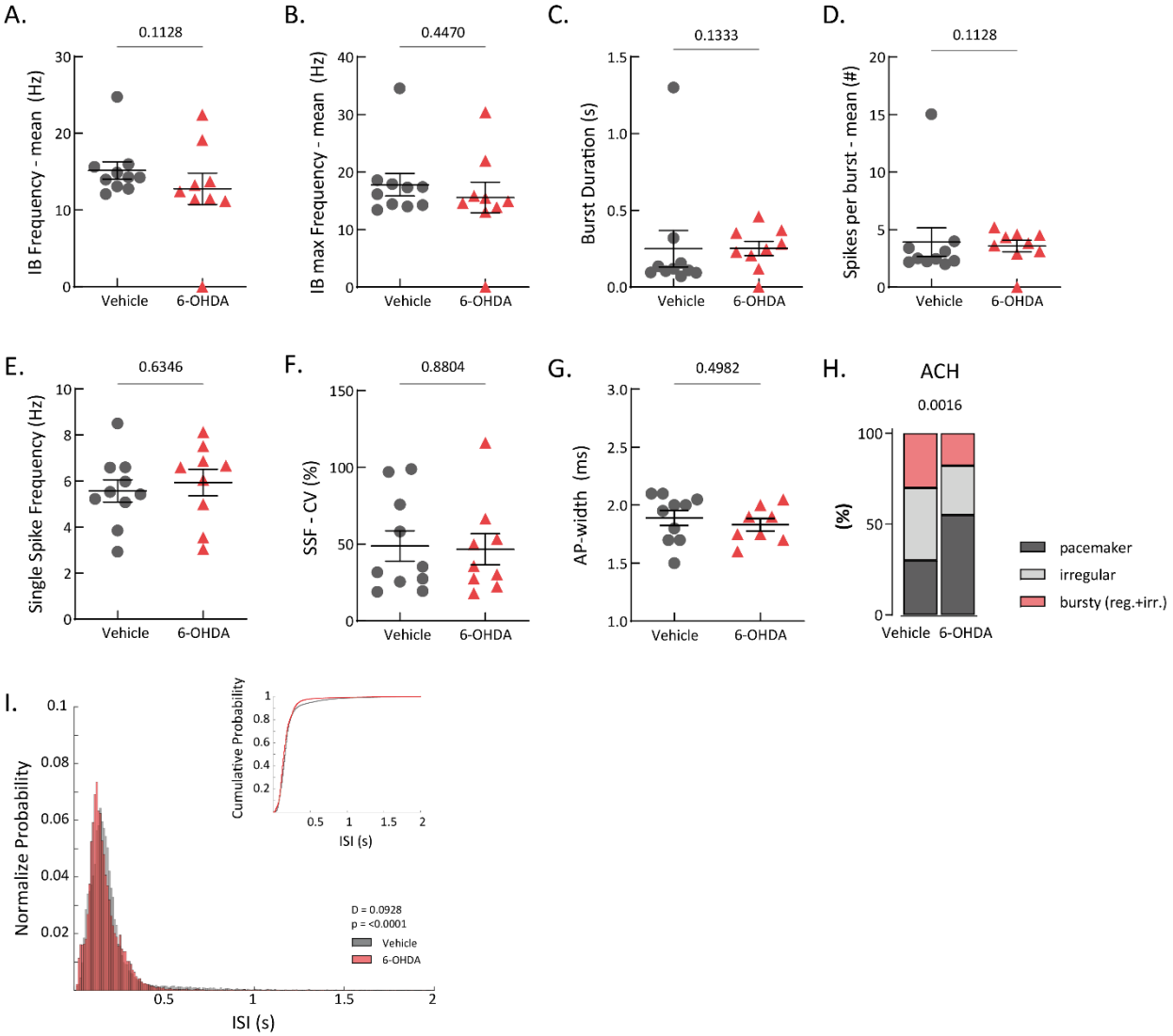

1063

1064 Scatter dot-plots, showing no significant difference of in vivo mean intra-burst (IB) frequency (A), mean
1065 maximum (max) intra-burst (IB) frequency (B), burst duration (C), number of spikes per burst (D), single spike
1066 frequency (SSF) (E), single spike coefficient of variance (CV) (F) and action potential (AP) width (G) (H) between
1067 the vehicle and 6-OHDA-infused mice in the late phase. (H) Normalized stacked bar plots of different in vivo
1068 firing patterns based on ACH. (I) ISI distributions from all in vivo recorded and labeled mSN DA neurons from
1069 vehicle- and 6-OHDA-treated mice in the late phase. Inset, cumulative representation of the same distributions.

1070 **Supplementary Figure 8.**

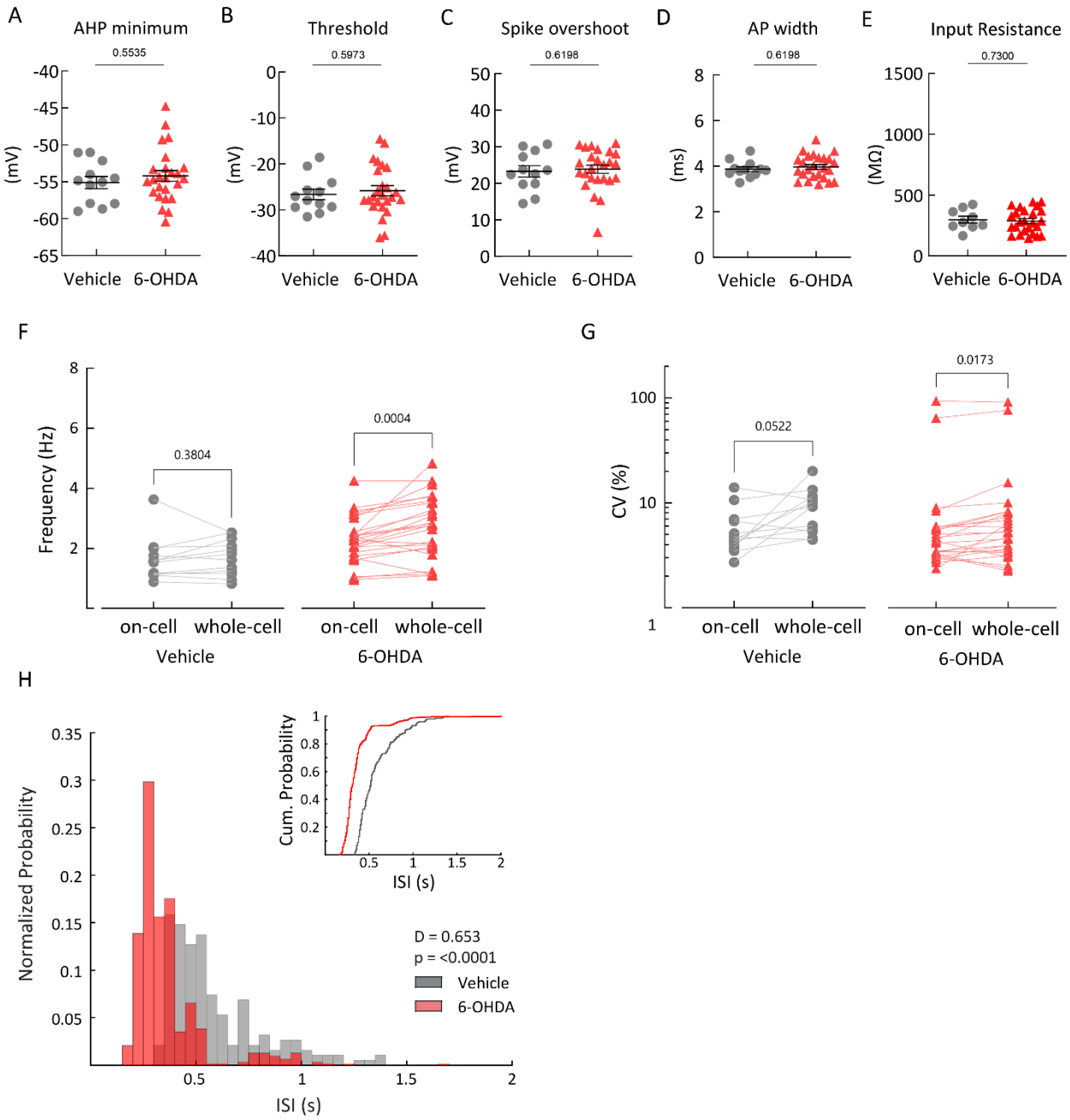

1071

1072 Scatter dot-plots, showing no significant difference of in vitro afterhyperpolarization (AHP) minimum (A),
1073 threshold (B), spike amplitude (C), action potential (AP) width (D) and input resistance (E) between the vehicle
1074 and 6-OHDA-infused mice in the late phase. (F), (G) Paired scatter dot-plots of firing frequency (F) and coefficient
1075 of variance (G) during on-cell recording and whole-cell recording in the late phase. (H) ISI distributions from all
1076 in vitro whole-cell recorded and labeled mSN DA neurons from vehicle- and 6-OHDA-treated mice in the late
1077 phase. Inset, cumulative representation of the same distributions.

1078 **Supplementary Figure 9.**

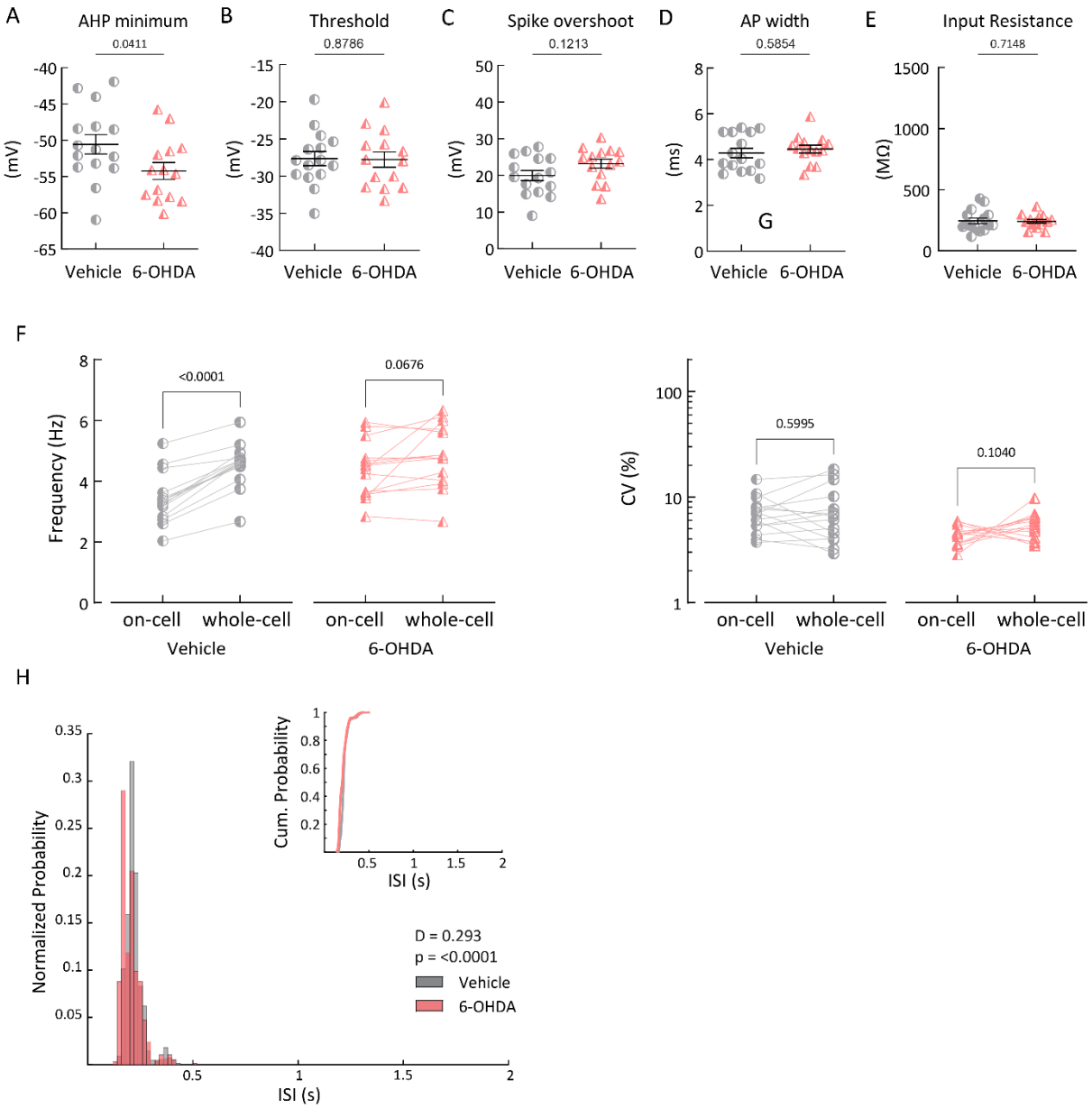

1079

1080 Scatter dot-plots, showing minor significant difference of in vitro afterhyperpolarization (AHP) minimum (A), and
1081 no difference in threshold (B), spike amplitude (C), action potential (AP) width (D) and input resistance (E)
1082 between the vehicle and 6-OHDA-infused mice in the late phase under 1µM AmmTx3. (F), (G) Paired scatter dot-
1083 plots of firing frequency (F) and coefficient of variance (G) during on-cell recording and whole-cell recording in
1084 the late phase under 1µM AmmTx3. (H) ISI distributions from all in vitro whole-cell recorded and labeled mSN
1085 DA neurons from vehicle- and 6-OHDA-treated mice in the late phase under 1µM AmmTx3. Inset, cumulative
1086 representation of the same distributions.

1087

1088 **Supplementary Figure 10.**

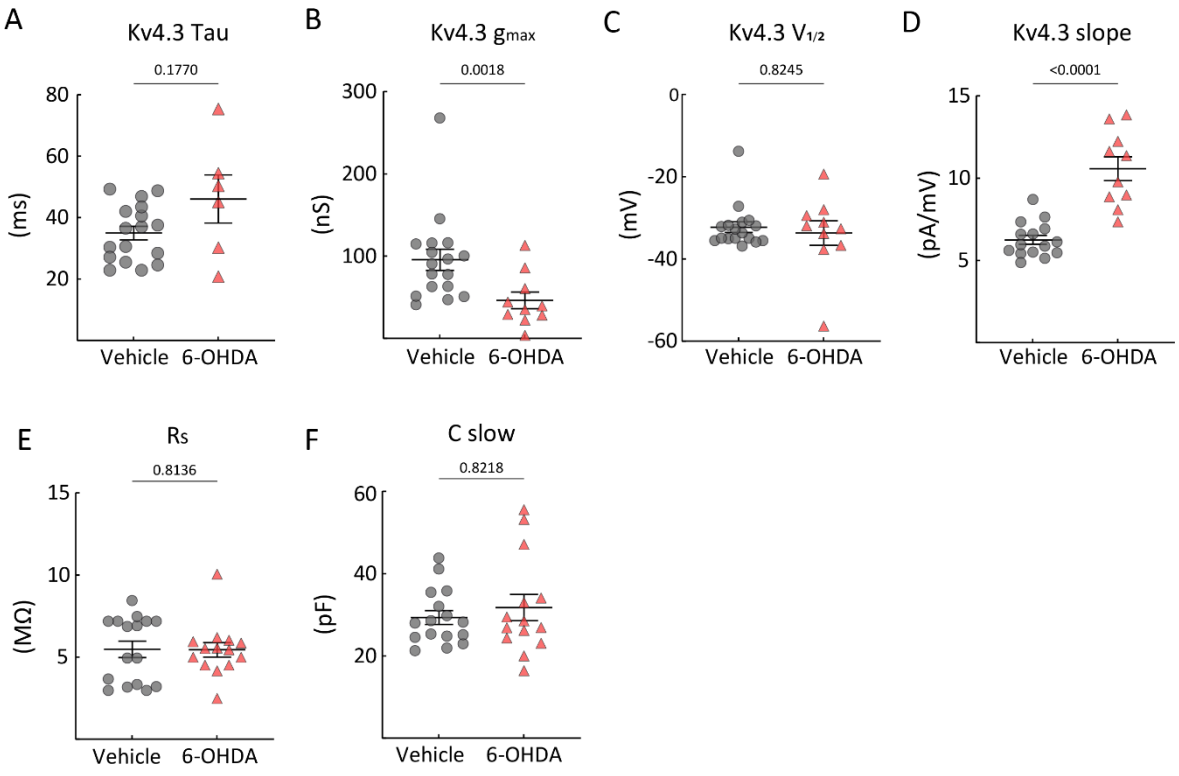

1089

1090 (A)-(D) Measurements of transient outward (A-type) potassium biophysical parameters in whole-cell voltage-

1091 clamp recordings of Kv4.3 channel activation and inactivation in vehicle relative to 6-OHDA infused mice. (E), (F)

1092 No difference in series resistance (Rs) or in slow capacitance between groups.

1093

Supplementary Figure 11.

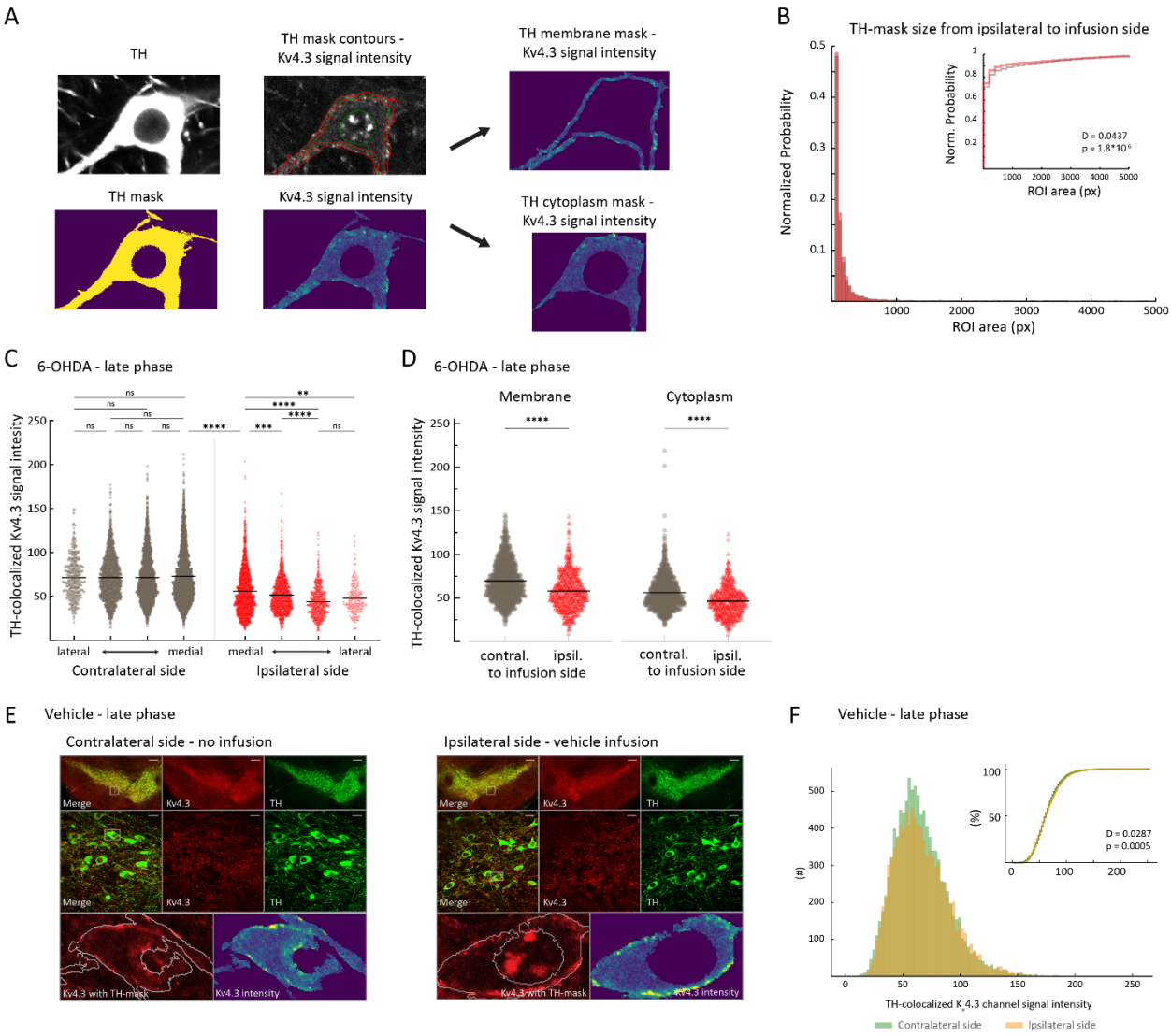

(A) Example illustration of an image from neuronal TH-immunosignal, transformed as a TH mask and overlayed on top of Kv4.3 immunosignal. Further segregation of the membrane and cytoplasm compartment with the corresponding Kv4.3 immunosignal intensity. (B) Distributions of all ROIs area sizes based on TH-masks from vehicle- (gray) and 6-OHDA-treated mice (red) in the late phase. Inset, cumulative representation of the same distributions. (C) Scatter dot-plots, illustrating the medio-lateral gradient of Kv4.3 immunosignal on the contralateral and ipsilateral side from 6-OHDA-treated mice in the late phase. (D) Scatter dot-plots, showing significant decrease in Kv4.3 immunosignal in both membrane and cytoplasm compartments in the ipsilateral (6-OHDA-infused) side compared to the contralateral (control) side. Membrane: $p = 0.0003$, contralateral side 67.2 ± 0.9, ipsilateral side 56.7 ± 1.1 (about 16% reduction); Cytoplasm: $p < 0.0001$, contralateral side 55.8 ± 0.9, ipsilateral side 45.9 ± 1.1 (about 18% reduction) (E) Top: 4x magnification of midbrain of a vehicle-infused mouse, >64 days post-lesion – contralateral side (left panel), and corresponding ipsilateral side (right panel). Middle: 60x

1107 magnification in the highlighted area from 4x image (green, TH; red, Kv4.3). Bottom, left: zoom-in on an example
1108 ROI (highlighted in 60x image). Bottom, right: color-coded Kv4.3-channel immunohistochemical signal intensity
1109 in the example ROI. (F) Histogram showing intensity of Kv4.3 immunosignals for all TH-positive ROIs, from
1110 ipsilateral, vehicle-infused, side (in orange) and from contralateral side (in green). Inset, same data shown as a
1111 cumulative distribution.

1112

1113

Figures

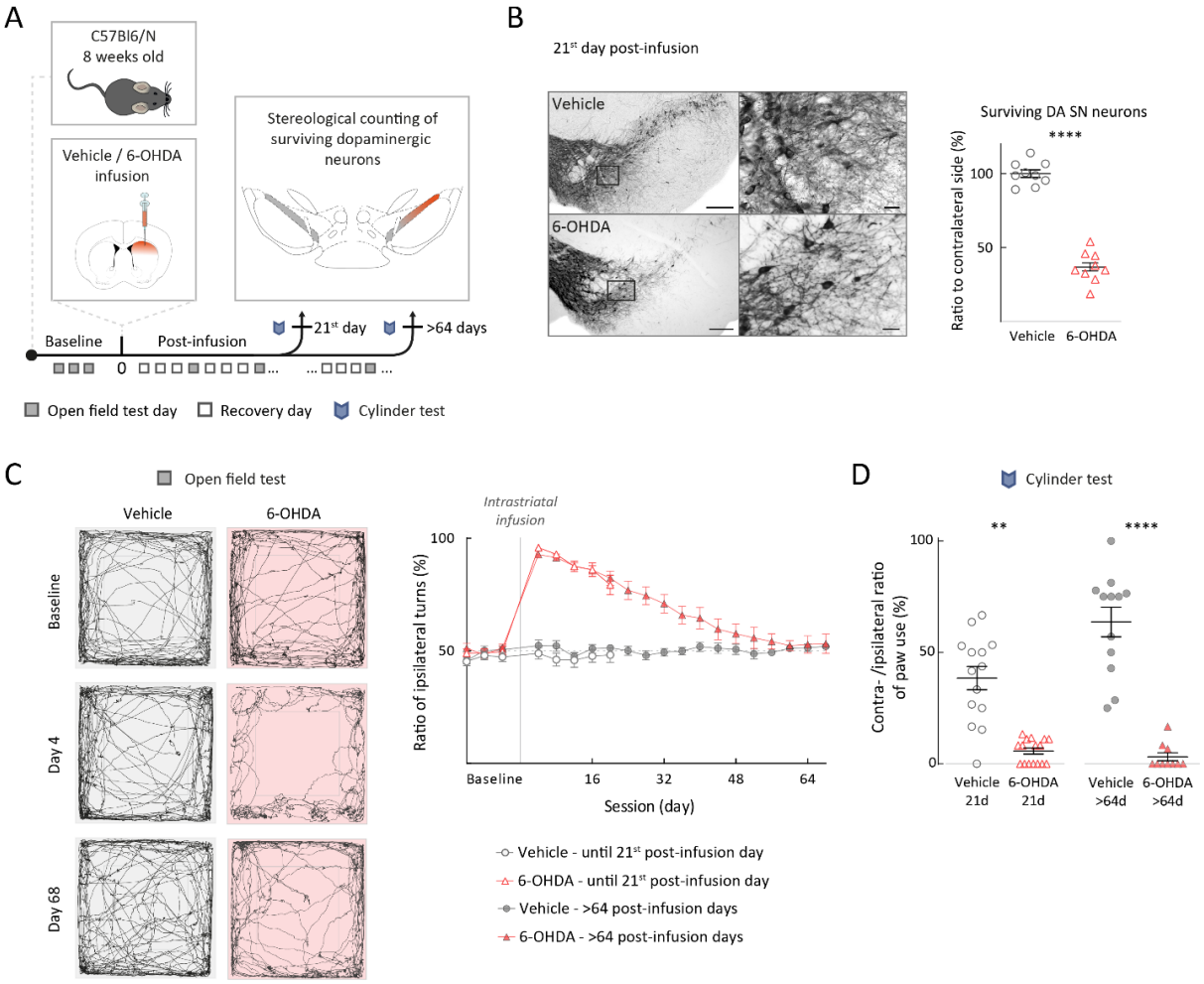

Figure 1. Unilateral striatal 6-OHDA mouse model with stable loss of SN DA neurons resulted in delayed partial behavioral recovery.

(A) Experimental design, illustrating timeline of behavioral assays with termination points – groups ended either on the 21st, or later than the 64th post-infusion day. (B) Left panel: TH-DAB staining of the SN, 10x magnification and 60x magnification for vehicle and 6-OHDA-infused mouse. Scalebar left 200µm, scalebar right 25µm. Right panel: ratio of ipsilateral (infusion side) to contralateral side of surviving TH-positive neurons in SN at 21st post-infusion day. (C) Left: spontaneous locomotion of mice in open field arena for a 10 min session. Left, examples of an ACSF-infused mouse (vehicle), right example of a 6-OHDA-infused mouse at baseline (upper panels), 4th post-infusion day (middle panels) and 68th post-infusion day (lower panels). Right: ratio of ipsilateral to contralateral turning behavior for all experimental groups plotted against session days. Note recovery in the 6-OHDA-treated mice from day 4 to day 68 after initial strong turning bias (>90%). (D) Cylinder test quantified by ratio of contra- to ipsilateral forepaw use. Note significant loss of contralateral forepaw involvement, both at 21 and 64 days. All data are presented as mean ± standard error of mean (SEM).

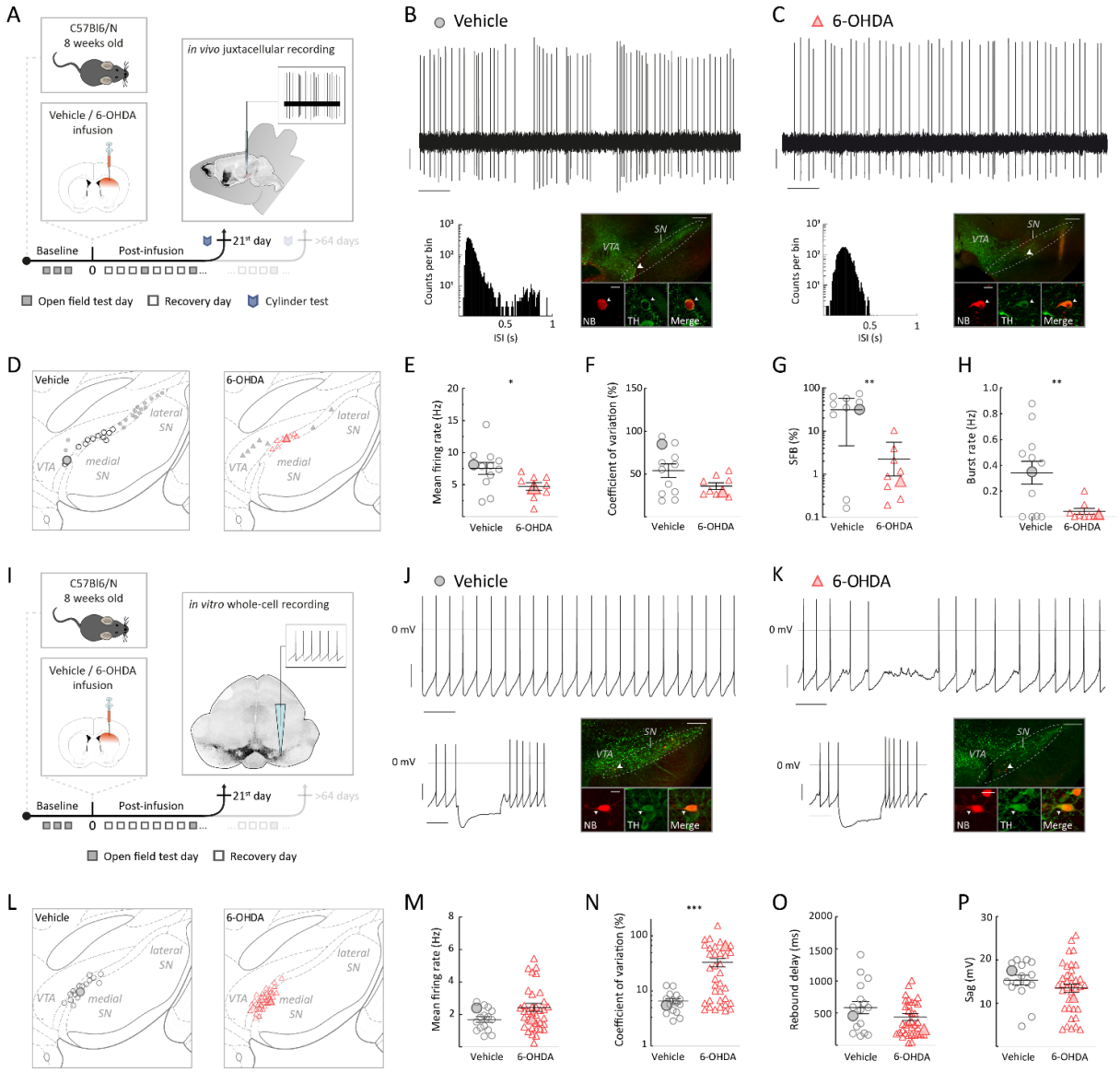

Figure 2. Surviving SN DA neurons at early post-6-OHDA phase exhibited a compressed dynamic range with a 10-fold decrease in *in vivo* bursting and a 5-fold decree in *in vitro* pacemaker regularity

(A), (I) Experimental design, illustrating timeline of behavioral assays, followed by terminal *in vivo* juxtacellular recordings (A) or by terminal *in vitro* whole-cell recordings (I) at the 21st post-infusion day. (B), (C) Top: 10s original recording trace of spontaneous *in vivo* single-unit activity from SN DA neurons in vehicle (B) and 6-OHDA-infused mouse (C). Scalebars: 1s, 0.2mV. Below, left: corresponding ISI histograms. Below, right: corresponding confocal images of juxtacellularly labelled and immunohistochemically identified DA neuron. Note the sparse bursting of the surviving SN DA neuron from the 6-OHDA-infused mouse at early phase. (D), (L) Anatomical mapping of all extracellularly recorded and juxtacellularly labelled DA neurons (D), and of all in vitro recorded and filled DA neurons (L), projected to bregma -3.08 mm. Location of example SN DA neurons in (B), (C), (J), (K) are highlighted. Smaller symbols represent DA neurons that have been recorded and identified, but not included in the group data analysis in (E-H). (E-H) Scatter dot-plots, showing significant decrease of *in vivo* mean firing rate (E), percentage of SFB (G) and burst rate (H) and no significant differences in CV (F) between the vehicle and 6-OHDA-infused mice. Note the 10-fold decrease in SFB for 6-OHDA-infused mice. (J), (K) Top: 10s original recording trace of *in vitro* whole-cell recording of spontaneous SN DA neuron activity in a vehicle (J) and 6-OHDA-infused (K) mouse. Scalebars: 1s, 20mV. Note that the 6-OHDA DA neuron has a highly irregular pacemaking. Below, left: corresponding to hyperpolarizing current injection. Below, right: confocal images of NB filled and immunohistochemically identified DA neuron. (M-P) Scatter dot-plots, showing no difference in *in vitro* mean firing rate (M), rebound delay (O) or sag-component (P) and a 5-fold increase in CV (N). Immunohistochemical imaging for all four DA neurons are displayed in 10x and 60x magnifications (green, TH; red, NB), scalebars: 200µm, 20µm. All data are presented as mean ± standard error of mean (SEM).

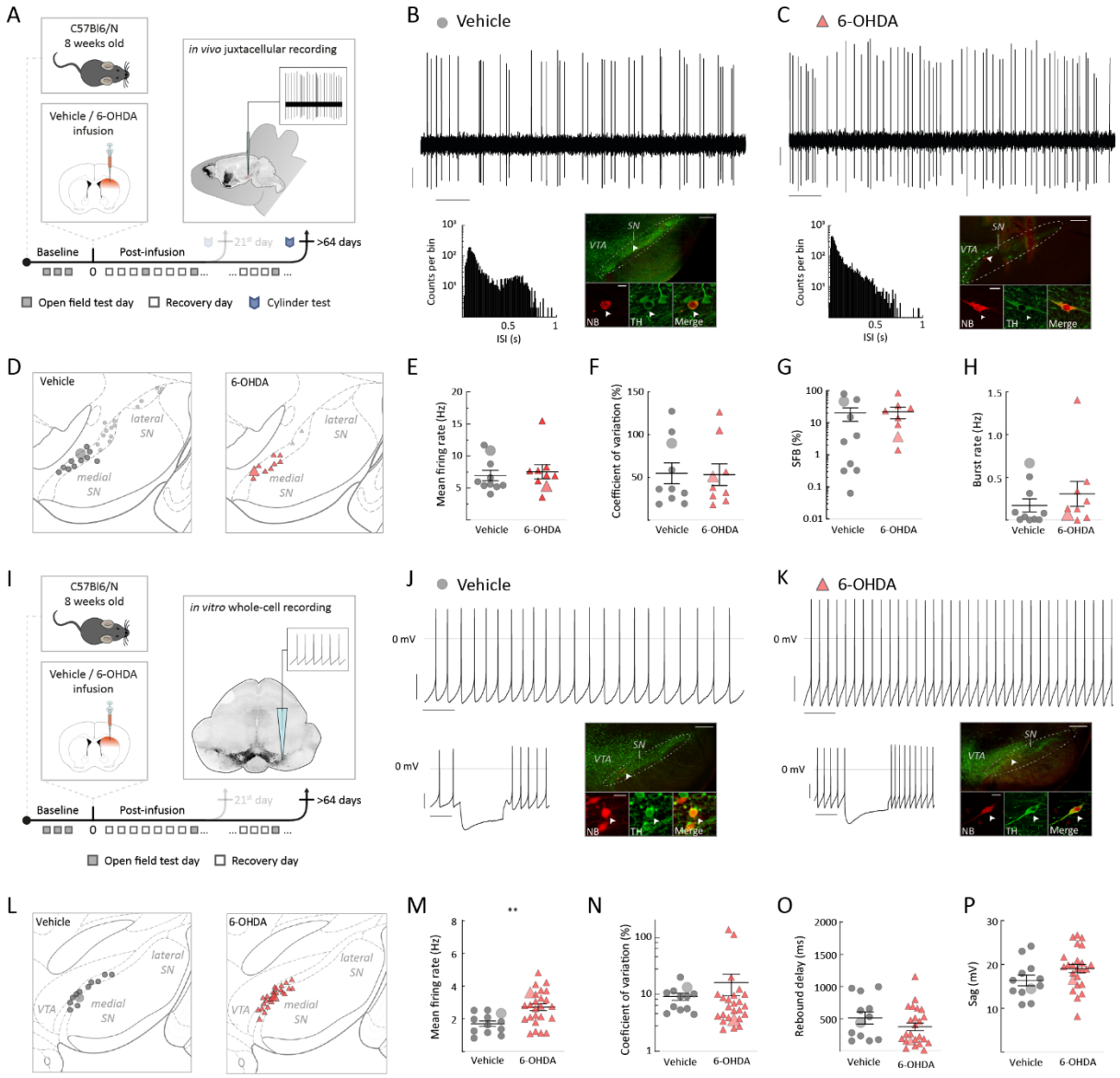

Figure 3. Surviving SN DA neurons at late 6-OHDA phase recovered *in vivo* burst firing and doubled their intrinsic pacemaker frequency *in vitro*.

(A), (I) Experimental design, illustrating timeline of behavioral assays, followed by terminal *in vivo* juxtacellular recordings (A) or by terminal *in vitro* whole-cell recordings (I) after >64 post-infusion days. (B), (C) Top: 10s original recording trace of spontaneous *in vivo* single-unit activity from SN DA neurons in vehicle (B) and 6-OHDA-infused mouse (C). Scalebars: 1s, 0.2mV. Below, left: corresponding ISI histograms. Below, right: corresponding confocal images of juxtacellularly labelled and immunohistochemically identified DA neuron. (D), (L) Anatomical mapping of all extracellularly recorded and juxtacellularly labelled DA neurons (D), and of all *in vitro* recorded and filled DA neurons (L), projected to bregma -3.40 mm (D) and -3.08mm (L). Location of example SN DA neurons in (B), (C), (J), (K) are highlighted. Smaller symbols represent DA neurons that have been recorded and identified, but not included in the group data analysis in (E-H). (E-H) Scatter dot-plots, showing no significant difference in mean firing rate (E), CV (F), SFB (G) and burst rate (H). (J), (K) Top: 10s original recording trace of *in vitro* whole-cell recording of spontaneous activity from SN DA neurons in a vehicle (J) and 6-OHDA-infused (K) mouse. Scalebars: 1s, 20mV. Note that the 6-OHDA DA neuron has enhanced, but regular pacemaking. Below, left, corresponding to hyperpolarizing current injection. Below, right, confocal images of NB filled and immunohistochemically identified DA neuron. (M-P) Scatter dot-plots, showing doubling of the firing rate (M), no difference in CV (N), decrease in rebound delay (O) and increase of sag-component (P) for the 6-OHDA-treated mice in comparison to vehicle group. Immunohistochemical imaging for all four DA neurons are displayed in 10x and 60x magnifications (green, TH; red, NB), scalebars: 200µm, 20µm. All data are presented as mean ± standard error of mean (SEM).

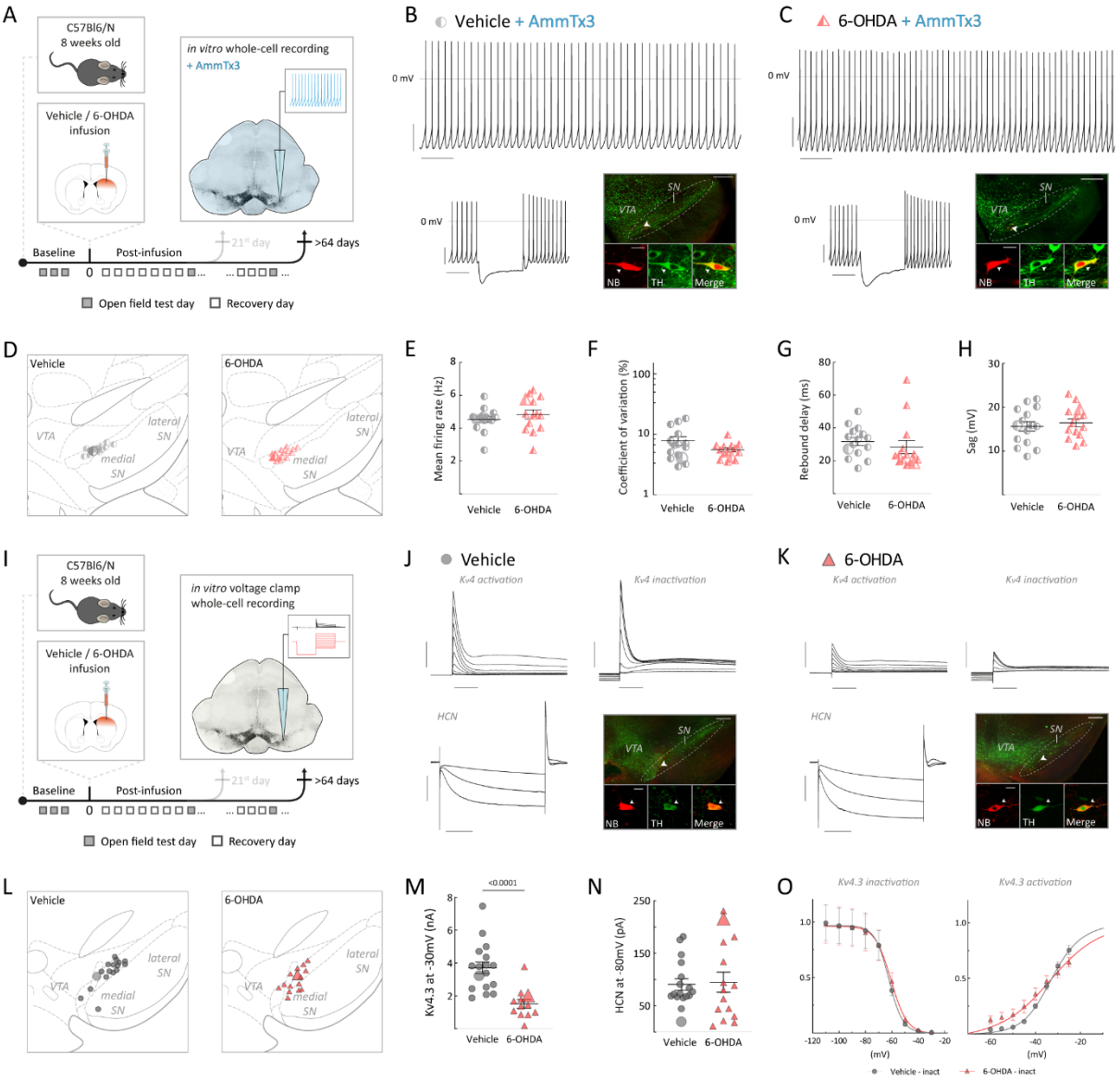

Figure 4. Enhanced pacemaker frequency of SN DA neurons at the late post-6-OHDA phase was mediated by K_v4.3 channel downregulation

(A), (I) Experimental design, illustrating timeline of behavioral assays, followed by terminal *in vitro* whole-cell recordings under K_v4.3 channel blocker AmmTx3 (A) or *in vitro* voltage-clamp whole-cell recordings (I) after >64 post-infusion days. (B), (C) Top: 10s original recording traces of *in vitro* whole-cell recording of spontaneous activity from DA SN neurons in AmmTx3-preincubated slices for a vehicle (B) and 6-OHDA-infused (C) mouse. Below, left: corresponding hyperpolarizing current injection. Scalebars: 1s, 20mV. Below, right: confocal images of NB filled and immunohistochemically identified DA neuron. (D), (L) Anatomical mapping of all in vitro recorded and filled DA neurons, projected to bregma -2.92 mm (D) and -3.16mm (L). (E-H) Scatter dot-plots, showing no differences in mean firing rate (E), coefficient of variation (F), rebound delay duration (G) and sag amplitude (H). (J), (K) Original recording trace of in vitro voltage-clamp recordings from DA SN neurons in a vehicle (J) and 6-OHDA-infused (K) mouse. Top, right: Zoom in from a K_v4.3 channel activation. Top, left: Zoom in from a K_v4.3 channel inactivation. Below, right: Zoom in from HCN-channel activation. Below, right, confocal images of NB filled and immunohistochemically identified DA neuron. Scalebars first row: 3nA, 100ms. Scalebars below, left: 5nA, 500ms. Note the small K_v4.3 channel in/activation peak in a surviving DA neuron from a 6-OHDA mouse in comparison the one from an ACSF treated mouse. Immunohistochemical imaging for all four DA neurons are displayed in 10x and 60x magnifications (green, TH; red, NB), scalebars: 200µm, 20µm. All data are presented as mean ± standard error of mean (SEM). (M) Scatter dot-plots, showing a significant, half of maximum K_v4.3 channel conductance in surviving DA neurons. (N) Scatter dot-plots, showing no difference in HCN channel delta current (I_{peak} - I_{steady}) between groups. (O) Normalized K_v4.3 current (I_{peak} - I_{steady}) at different voltage steps, resulting in inactivation and activation curve for both groups. All data are presented as mean ± standard error of mean (SEM).

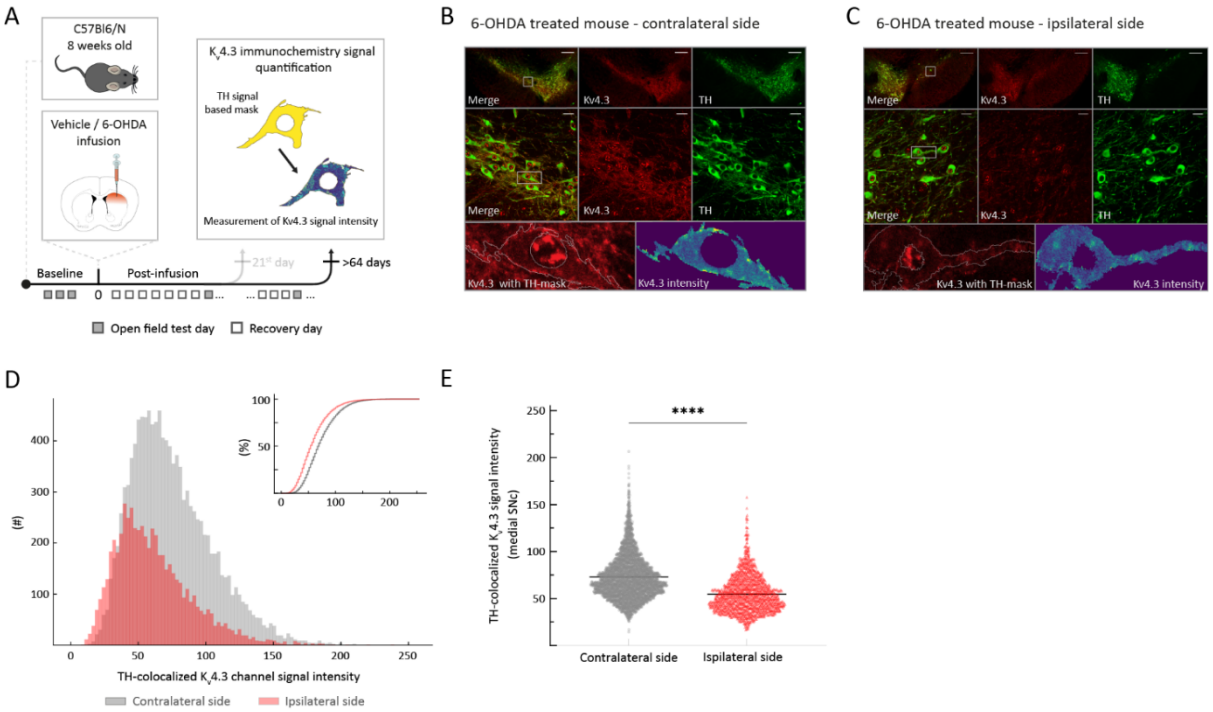

Figure 5. Surviving DA SN neurons at the late post-6-OHDA phase showed lower K_v4.3 channel immunohistochemical signal

(A) Experimental design, illustrating timeline of behavioral assays, followed by multi-labeling immunohistochemistry for exploring K_v4.3-channel expression differences after >64 post-infusion days. (B), (C) Top: 4x magnification of midbrain of a 6-OHDA-infused mouse, >64 days post-lesion – contralateral side (B), and corresponding ipsilateral side (C). Middle: 60x magnification in the highlighted area from 4x image (green, TH; red, K_v4.3). Bottom, left: zoom-in on an example ROI (highlighted in 60x image). Bottom, right: color-coded Kv4.3-channel immunohistochemical signal intensity in the example ROI. Note K_v4.3-channel signal decrease in surviving DA neurons on the ipsilateral to the injection side. (D) Histogram showing intensity of K_v4.3 immunosignals for all TH-positive ROIs, from ipsilateral, lesioned, side (in red) and from contralateral side (in grey). Inset, same data shown as a cumulative distribution. Note a clear right-shift to lower intensities for the ipsilateral side. (E) Comparison of mean TH-colocalized K_v4.3 immunosignals from medial SN from ipsilateral, lesioned, side, and contralateral, as control side. All data are presented as mean ± standard error of mean (SEM).

Supplementary Figures

Supplementary Figure 1.

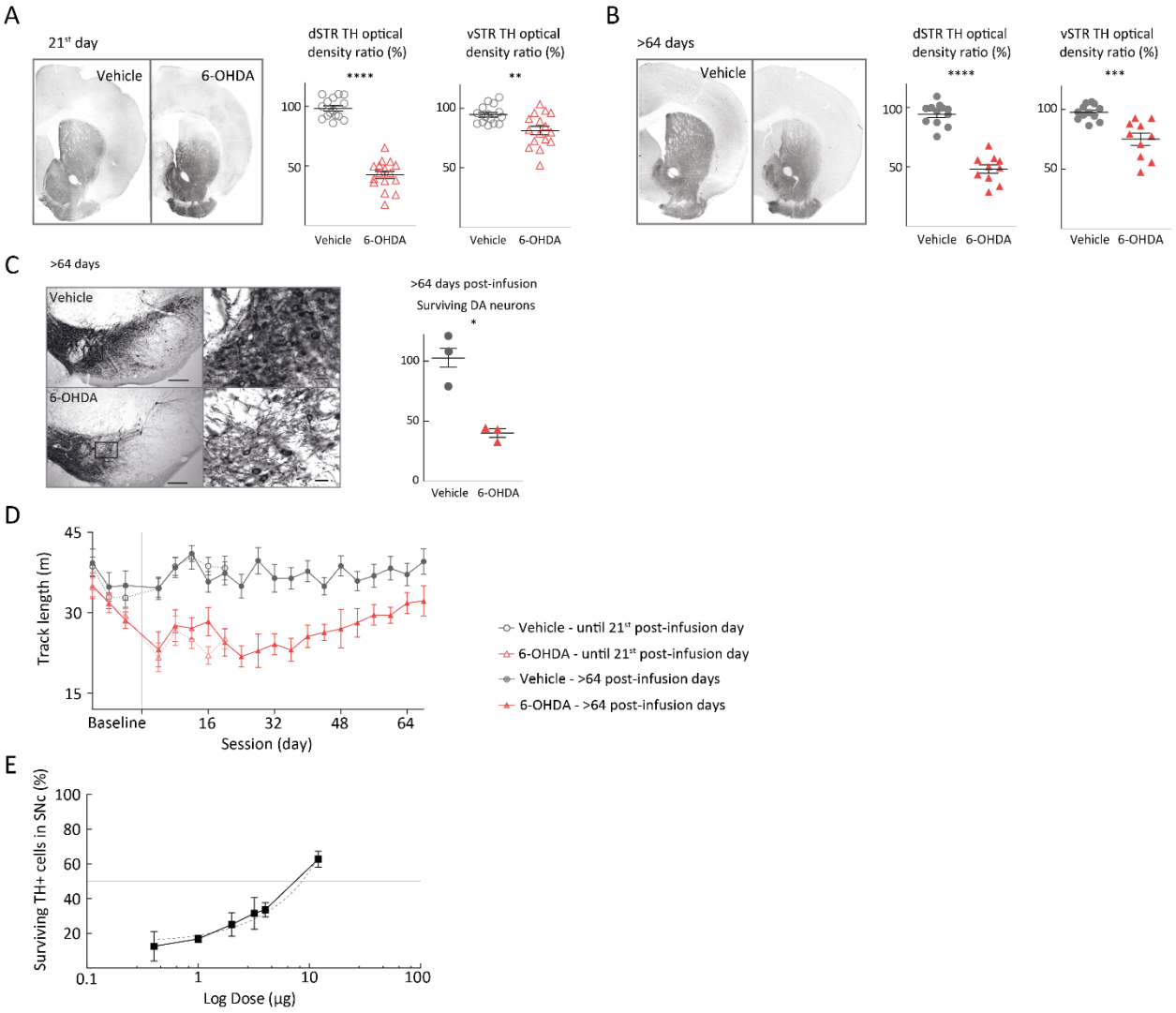

(A), (B) Comparison of ipsilateral, infusion side, to contralateral side as percentage of relative TH immunohistochemistry signal in the dorsal striatum (dSTR) and ventral striatum (vSTR), at the corresponding early (A) and late phase (B). Note the stability of TH density loss in the dorsal striatum through time. (C) Ratio of ipsilateral (infusion side) to contralateral side of surviving TH-positive neurons in SN in the late phase. (D) Mean track length from all mice for each open field session. Note the post-infusion drop in performed track in the 6-OHDA groups, which gradually recovers. (Infusion day marked as a thin gray line.) (E) Ratio of TH+ cell loss in SNc (ipsilateral (infusion side) to contralateral side) >21st post-infusion day from different infused 6-OHDA doses.

Supplementary Figure 2.

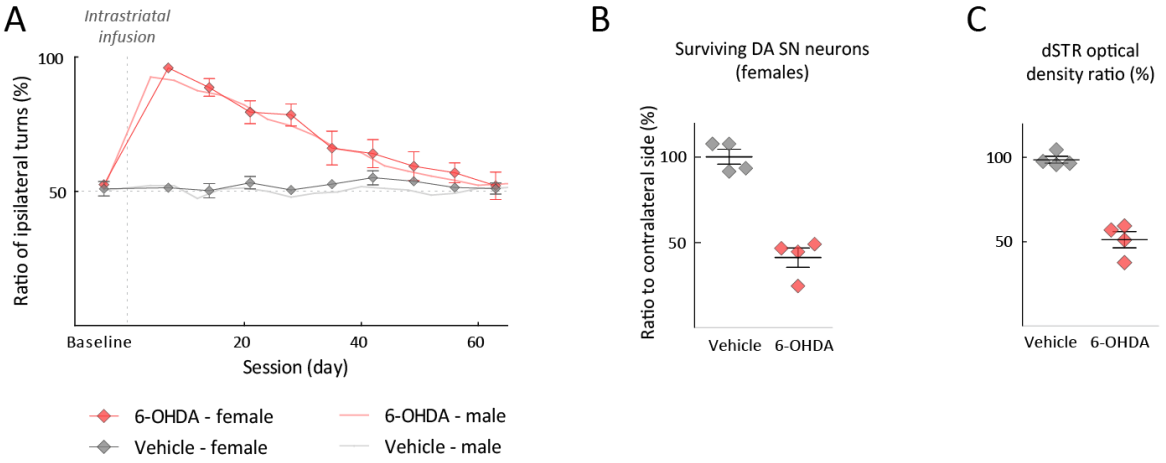

(A) Ratio of ipsilateral to contralateral turning behavior for female ACSF and 6-OHDA infused groups plotted against session days and with underlayed the corresponding ratio from the male ACSF and 6-OHDA groups as a mean-line. (B) Ratio of ipsilateral (infusion side) to contralateral side of surviving TH-positive neurons in SN at >64st post-infusion day from female ACSF and 6-OHDA infused mice. (C) Comparison of ipsilateral, infusion side, to contralateral side as percentage of relative TH immunohistochemistry signal in the dorsal striatum (dSTR) at >64st post-infusion day from female ACSF and 6-OHDA infused mice.

Supplementary Figure 3.

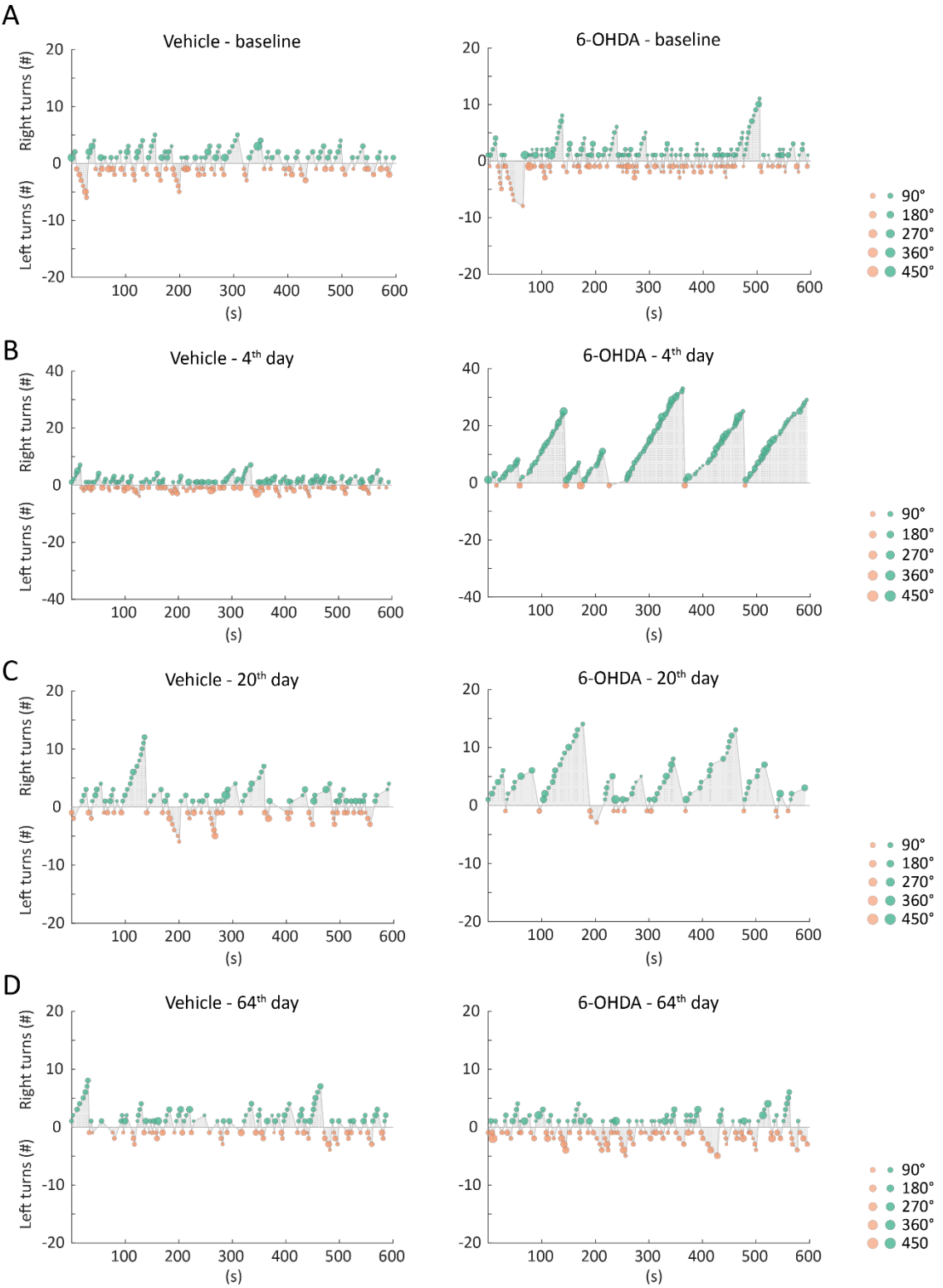

For two representative vehicle- and 6-OHDA-treated mice schematic representation of turning sequences. Left turn sequences are plotted as negative values, whereas right turn sequences are plotted as positive values. The count represents the number of same-direction turns within a sequence. On the left panels are turning sequences for the control animal and on the right panels for the 6-OHDA-infused animal, correspondingly in a baseline session (A), 4th post-operative day (B), 20th post-operative day (C) and 64th post-operative day (D).

Supplementary Figure 4.

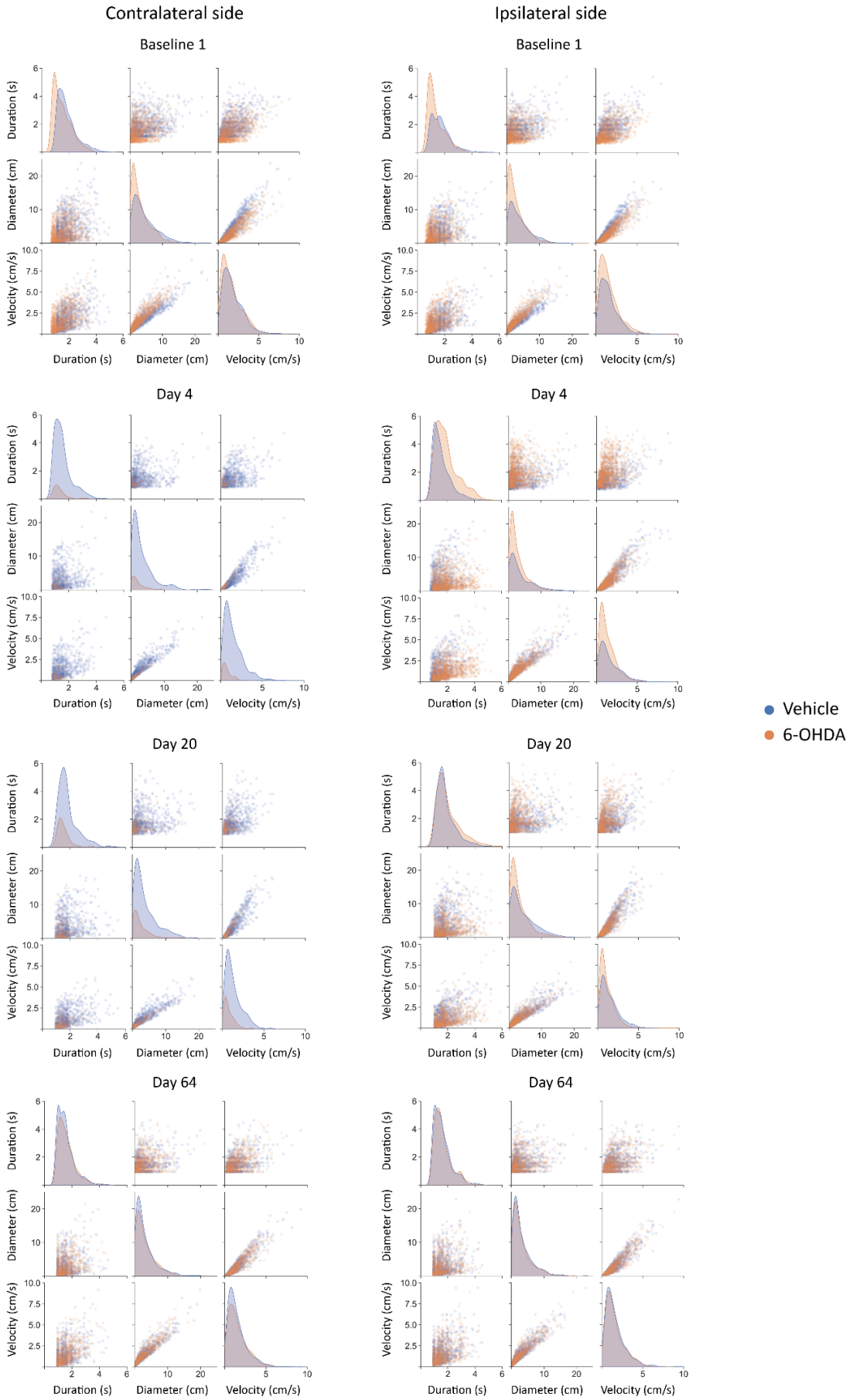

Correlation pair plots comparing turning features, such as velocity (cm/s), diameter (cm) and duration for all contralateral turns (left panels) and all ipsilateral turns performed from all vehicle-infused mice (in orange) and all 6-OHDA-treated mice (in blue) across different time points (baseline, 4th, 20th and 64th post-infusion day).

Supplementary Figure 5.

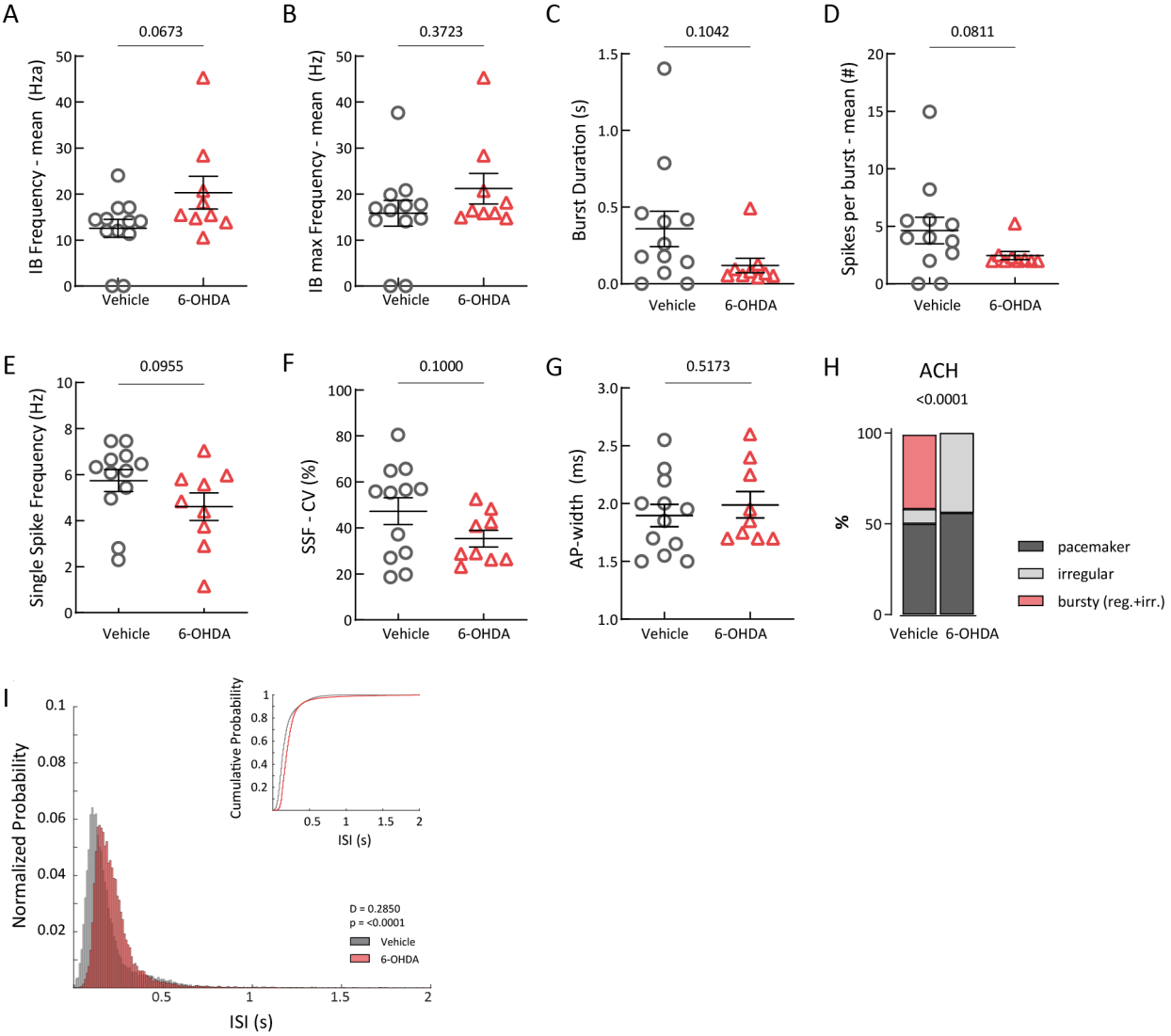

Scatter dot-plots, showing no significant difference of in vivo mean intra-burst (IB) frequency (A), mean maximum (max) intra-burst (IB) frequency (B), burst duration (C), number of spikes per burst (D), single spike frequency (SSF) (E), single spike coefficient of variance (CV) (F) and action potential (AP) width (G) (H) between the vehicle and 6-OHDA-infused mice in the early phase. (H) Normalized stacked bar plots of different in vivo firing patterns based on ACH. (I) ISI distributions from all in vivo recorded and labeled mSN DA neurons from vehicle- and 6-OHDA-treated mice in the early phase. Inset, cumulative representation of the same distributions.

Supplementary Figure 6.

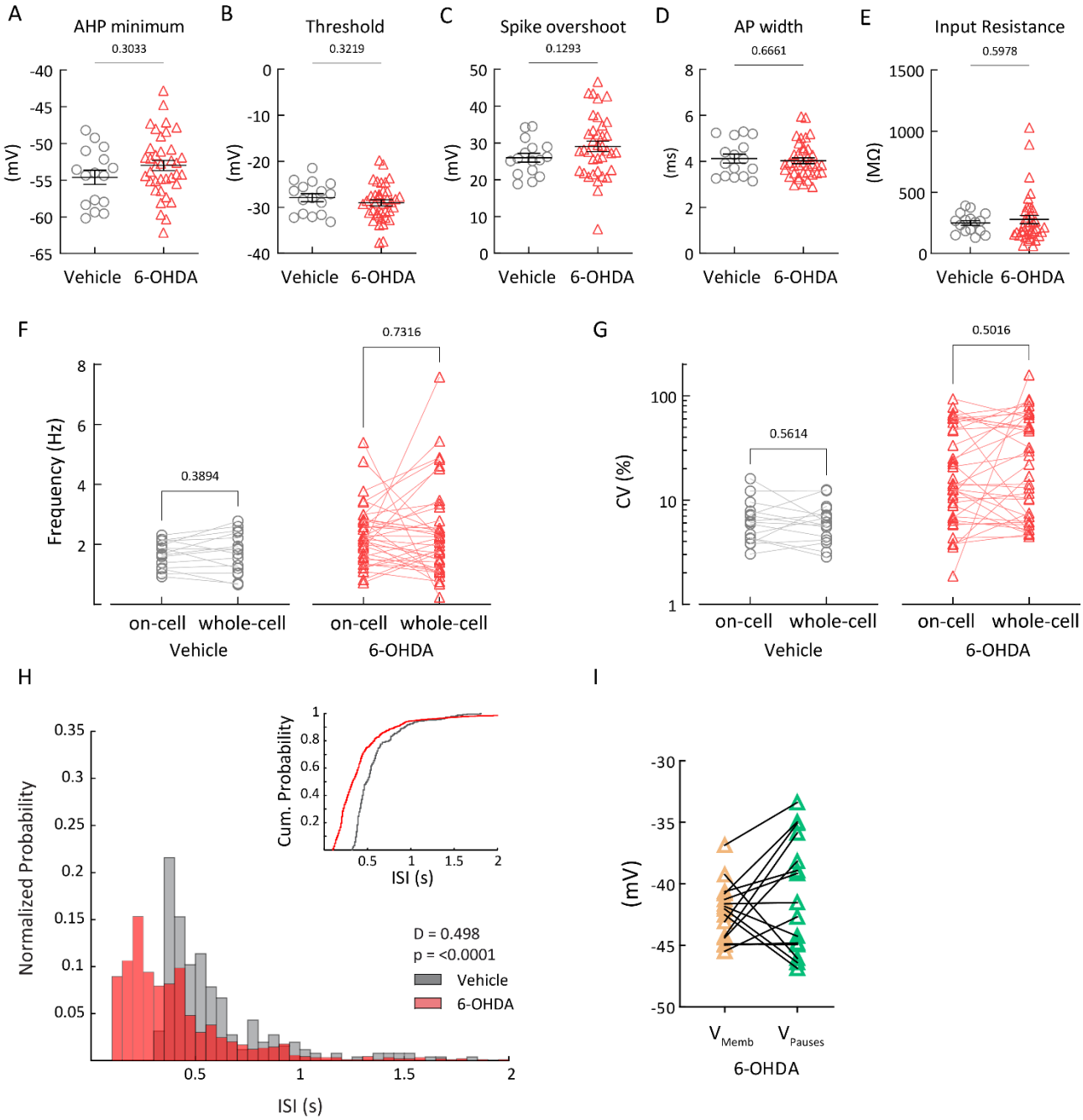

Scatter dot-plots, showing no significant difference of in vitro afterhyperpolarization (AHP) minimum (A), threshold (B), spike amplitude (C), action potential (AP) width (D) and input resistance (E) between the vehicle and 6-OHDA-infused mice in the early phase. (F), (G) Paired scatter dot-plots of firing frequency (F) and coefficient of variance (G) during on-cell recording and whole-cell recording in the early phase. (H) ISI distributions from all in vitro whole-cell recorded and labeled mSN DA neurons from vehicle- and 6-OHDA-treated mice in the early phase. Inset, cumulative representation of the same distributions. (I) Paired scatter dot-plot indicating no significant difference between the mean voltage during spike-pauses and the rest of the firing activity.

Supplementary Figure 7.

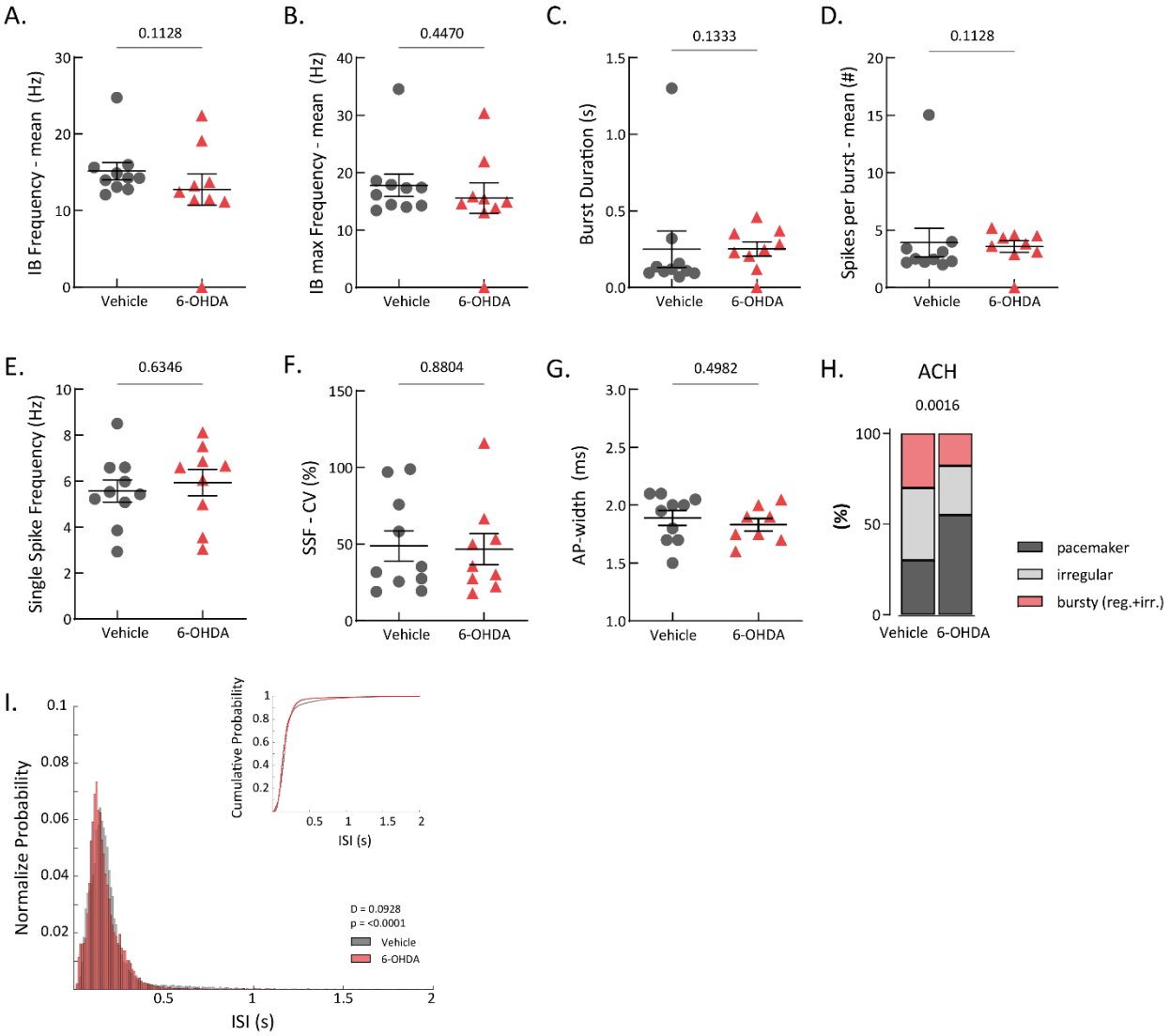

Scatter dot-plots, showing no significant difference of in vivo mean intra-burst (IB) frequency (A), mean maximum (max) intra-burst (IB) frequency (B), burst duration (C), number of spikes per burst (D), single spike frequency (SSF) (E), single spike coefficient of variance (CV) (F) and action potential (AP) width (G) (H) between the vehicle and 6-OHDA-infused mice in the late phase. (H) Normalized stacked bar plots of different in vivo firing patterns based on ACH. (I) ISI distributions from all in vivo recorded and labeled mSN DA neurons from vehicle- and 6-OHDA-treated mice in the late phase. Inset, cumulative representation of the same distributions.

Supplementary Figure 8.

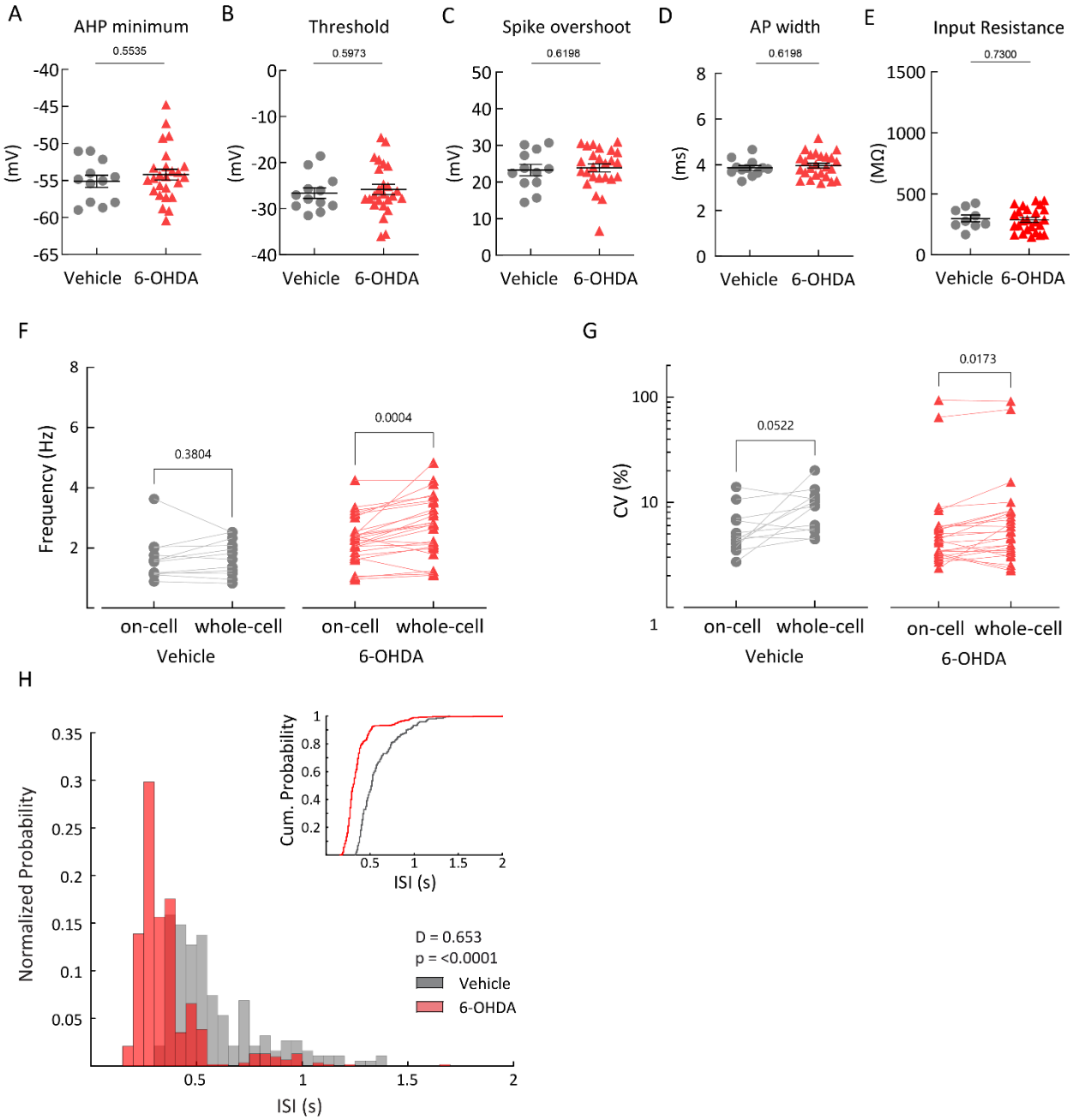

Scatter dot-plots, showing no significant difference of in vitro afterhyperpolarization (AHP) minimum (A), threshold (B), spike amplitude (C), action potential (AP) width (D) and input resistance (E) between the vehicle and 6-OHDA-infused mice in the late phase. (F), (G) Paired scatter dot-plots of firing frequency (F) and coefficient of variance (G) during on-cell recording and whole-cell recording in the late phase. (H) ISI distributions from all in vitro whole-cell recorded and labeled mSN DA neurons from vehicle- and 6-OHDA-treated mice in the late phase. Inset, cumulative representation of the same distributions.

Supplementary Figure 9.

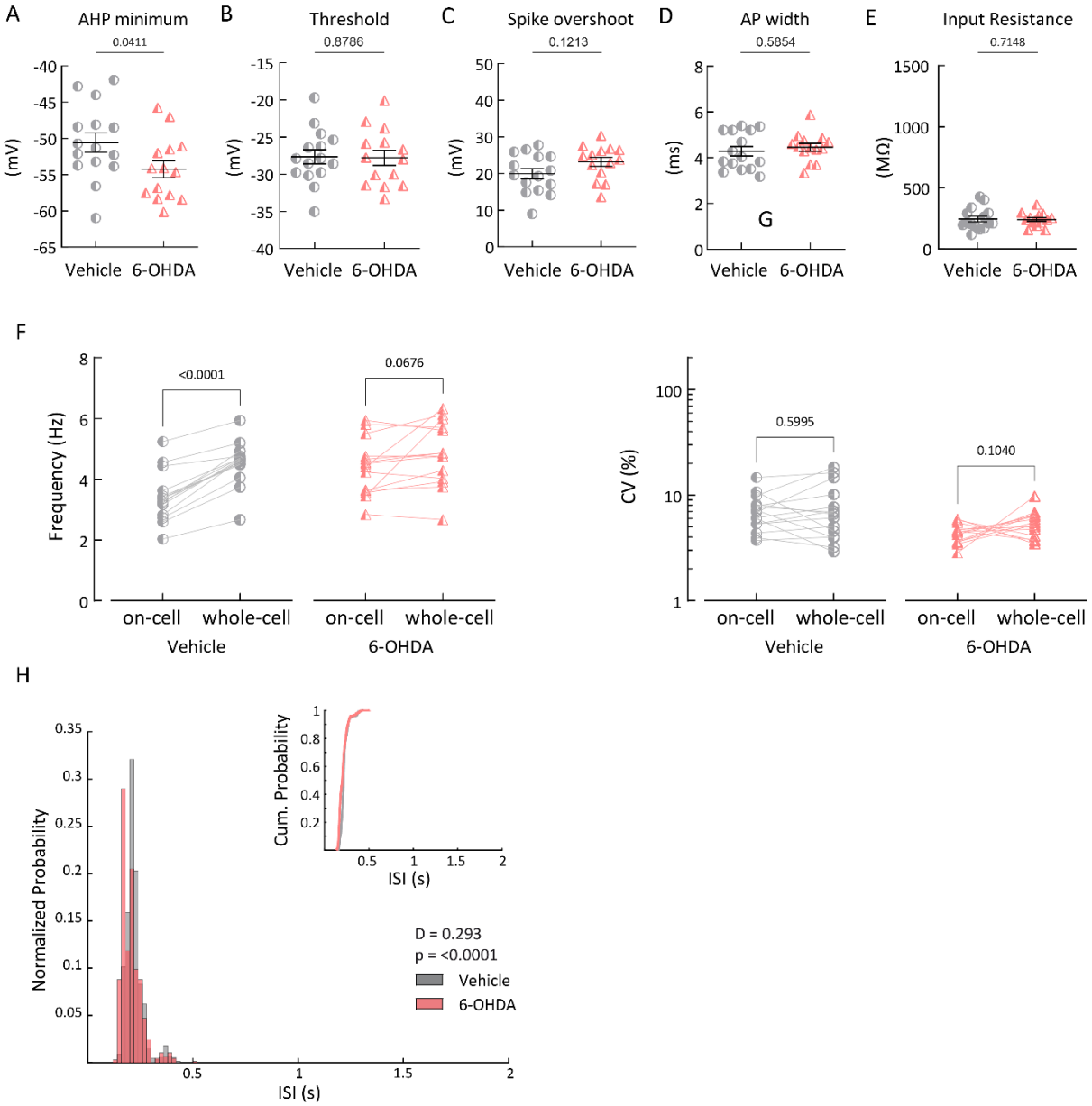

Scatter dot-plots, showing minor significant difference of in vitro afterhyperpolarization (AHP) minimum (A), and no difference in threshold (B), spike amplitude (C), action potential (AP) width (D) and input resistance (E) between the vehicle and 6-OHDA-infused mice in the late phase under 1µM AmmTx3. (F), (G) Paired scatter dot-plots of firing frequency (F) and coefficient of variance (G) during on-cell recording and whole-cell recording in the late phase under 1µM AmmTx3. (H) ISI distributions from all in vitro whole-cell recorded and labeled mSN DA neurons from vehicle- and 6-OHDA-treated mice in the late phase under 1µM AmmTx3. Inset, cumulative representation of the same distributions.

Supplementary Figure 10.

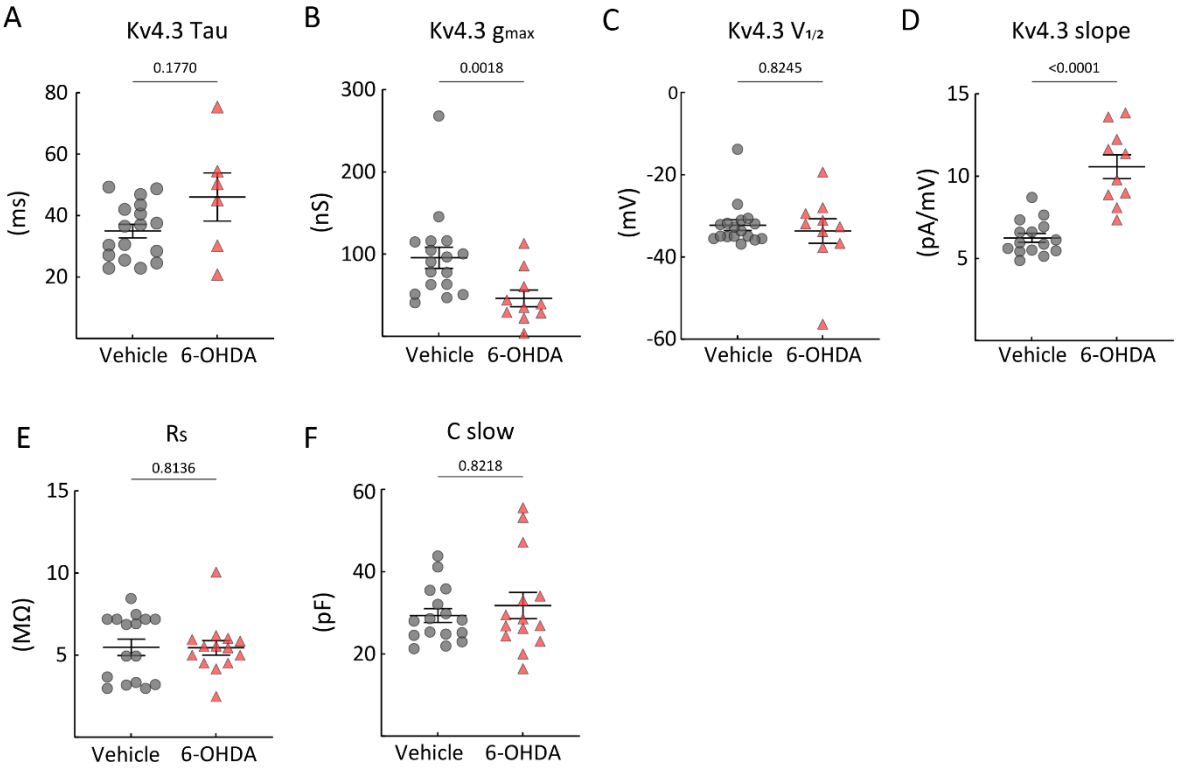

(A)-(D) Measurements of transient outward (A-type) potassium biophysical parameters in whole-cell voltage-clamp recordings of Kv4.3 channel activation and inactivation in vehicle relative to 6-OHDA infused mice. (E), (F) No difference in series resistance (Rs) or in slow capacitance between groups.

Supplementary Figure 11.

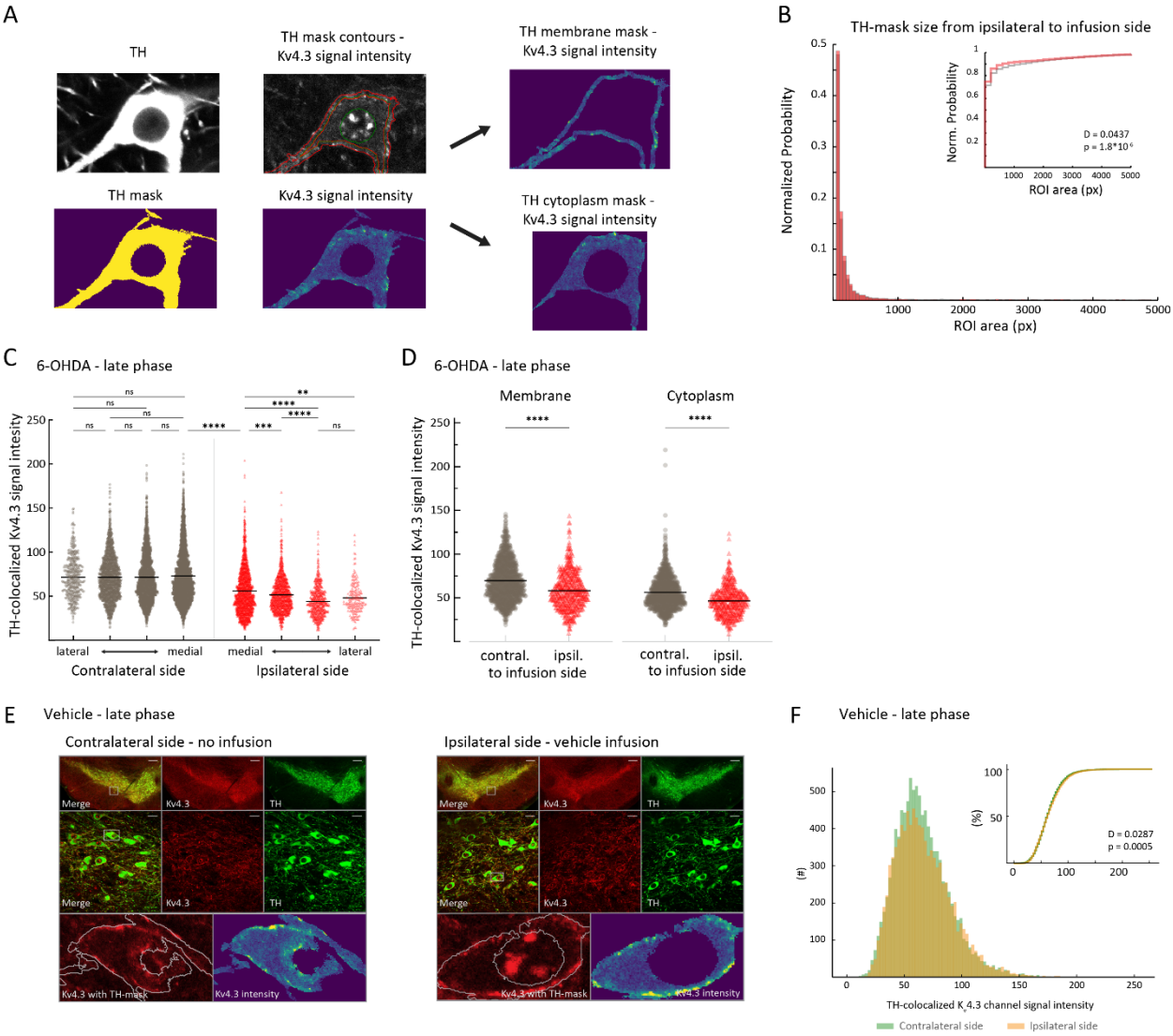

(A) Example illustration of an image from neuronal TH-immunosignal, transformed as a TH mask and overlayed on top of Kv4.3 immunosignal. Further segregation of the membrane and cytoplasm compartment with the corresponding Kv4.3 immunosignal intensity. (B) Distributions of all ROIs area sizes based on TH-masks from vehicle- (gray) and 6-OHDA-treated mice (red) in the late phase. Inset, cumulative representation of the same distributions. (C) Scatter dot-plots, illustrating the medio-lateral gradient of Kv4.3 immunosignal on the contralateral and ipsilateral side from 6-OHDA-treated mice in the late phase. (D) Scatter dot-plots, showing significant decrease in Kv4.3 immunosignal in both membrane and cytoplasm compartments in the ipsilateral (6-OHDA-infused) side compared to the contralateral (control) side. Membrane: $p = 0.0003$, contralateral side 67.2 ± 0.9, ipsilateral side 56.7 ± 1.1 (about 16% reduction); Cytoplasm: $p < 0.0001$, contralateral side 55.8 ± 0.9, ipsilateral side 45.9 ± 1.1 (about 18% reduction) (E) Top: 4x magnification of midbrain of a vehicle-infused mouse, >64 days post-lesion – contralateral side (left panel), and corresponding ipsilateral side (right panel). Middle: 60x magnification in the highlighted area from 4x image (green, TH; red, Kv4.3). Bottom, left: zoom-in on an example ROI (highlighted in 60x image). Bottom, right: color-coded Kv4.3-channel immunohistochemical signal intensity in the example ROI. (F) Histogram showing intensity of Kv4.3 immunosignals for all TH-positive ROIs, from ipsilateral, vehicle-infused, side (in orange) and from contralateral side (in green). Inset, same data shown as a cumulative distribution.